AlGaAs OPTOELECTRONIC DEVICES

FOR OPTICAL COMMUNICATIONS

Thesis by

Joseph Katz

In Partial Fulfillment of the Requirements

for the Degree of

Doctor of Philosophy

California Institute of Technology

Pasadena, California

1981

(Submitted May 6, 1981)

To My Wife,

Our Parents

and Our Children

– Acknowledgment –

–ABSTRACT –

This thesis describes several semiconductor injection laser diodes and related optoelectronic devices that can be used as light sources for optical communication systems, and develops the intrinsic electrical model of the laser diode. All the devices were grown from the GaAs–GaAlAs ternary system using the liquid phase epitaxy technique. The AlGaAs materials are very useful for the fabrication of both optical devices (sources and detectors) and conventional electronic components, due to their optical and electrical properties.

The first device is the Translaser, a monolithically integrated heterostructure bipolar transistor with an injection laser. The next two types of devices possess bistable electrical characteristics. One is a laser–SCR switch, and the second type consists of multi–PN heterostructure devices. Each of the devices described above performs an electronic function of modulating the light output of the laser associated with it.

Finally, two types of low–threshold single–mode laser diodes are presented. Their properties make them attractive candidates for sources in optical fiber communication systems. The first one is the Embedded Stripe Laser, and the second one is a new version of the Buried–Heterostructure laser, fabricated on semi–insulating substrates.

An equivalent circuit of the laser diode is presented in the last chapter. This model provides a better understanding of the operation of the laser diode, which is particularly important in applications which

involve its high frequency operation with other electronic components and when a modification of its frequency response is needed.

Table of Contents

1. INTRODUCTION

1.1 Optical Communication

The challenges involved in the storage, processing and distribution of ever increasing amounts of information at high rates are among the more important technological aspects of our era, and their importance is expected to increase even further in the future. Owing to their shorter wavelengths, electromagnetic waves in the spectral range of the optical and the near infra–red region have inherent advantages over microwaves which make them attractive to be used as carriers of information in communication systems.

The main media used today for transmitting optical waves are the various types of optical fibers. State of the art silica fibers are superior to metal cables and transmission lines used in the radio frequency and the microwave bands. They are smaller in size (several micrometers of diameter for single–mode fibers), light–weight, cheap, rugged and durable, immune to electromagnetic interference, difficult to tap, and they provide electrical isolation (since they carry fields, not charges). In the $0.85\mu m$ region, where $AlGaAs$ lasers and LEDs operate, optical fibers have low losses (attenuation coefficients of less than 3 db/km can be obtained) and large bandwidth–range product ($\approx 5GHz\text{-}km$). This makes it possible to have communication links with large spacings between repeaters. It should be noted that attenuation and bandwidth/dispersion parameters are even better in the $1.3\mu m$ and $1.55\mu m$ regions.

It is clear that other devices are needed if one is to realize efficient optical communication systems. These devices include light sources and detectors, repeaters, and all the electronic circuitry needed for the conversion of electronic signals into optical waves (at the source terminal) and vice versa (at the detector terminal). Semiconductor injection laser diodes are very attractive light sources because of their small size, ruggedness and reliability, efficiency, and the ability to modulate them directly (by modulating the current that flows through them) at high rates, up to the gigahertz region.

From the point of view of the overall relibility, cost and speed of the of the system, it is desirable that as many functions as possible, both optical and electronic, are combined monolithically on a common substrate. *GaAs* has been proposed by A. Yariv as a base for optoelectronic devices and circuits, since it can be employed in fabricating both electronic devices and optical devices [1]. It is a direct bandgap semiconductor, and thus efficient light sources (injection lasers and LEDs) can be fabricated from it, as well as efficient light detectors. Usually the lattice matched ternary $GaAs - Ga_{1-x}Al_xAs$ system is used for the device fabrication, as will be discussed in the next section. Furthermore, compared to silicon, which is the backbone of the electronic industry today, *GaAs* has higher electron mobility, and is thus suitable for the fabrication of high frequency electronic devices. Finally, the existence of semi-insulating *GaAs* crystals makes the monolithic integration of optical and electronic devices possible. It should be noted that other materials, and in particular the quarternary $InP - InGaAsP$ system, can also be used for

the same applications at longer wavelengths. A recent comprehensive review on the subject of devices for optical fiber communication is reference [2].

Before closing this section, it is worth mentioning that using optical waves has advantages also in free-space communication systems. Since the diffraction beam spread is $\approx \frac{\lambda}{D}$ (where λ is the radiation wavelength and D is the diameter of the transmitting antenna), very narrow beam patterns can be obtained, thus resulting in larger communication ranges. Furthermore, unlike in the microwave regime, it is conceivable to have systems operating in a regime where the dominant noise mechanism is not the thermal (KT) noise, but the quantum noise of the radiation (i.e., photon "shot noise"). In this case, communication systems have higher capacities and are thus more efficient [3].

1.2 AlGaAs Heterostructure Injection Lasers

Since the first demonstration of their operation [4], [5], the performance of semiconductor injection lasers has been greatly improved. The basic principle of the operation of these devices is by stimulated emission through recombination of injected carriers, which takes place in a region near the PN junction ("active region"). Part of the resulting radiation is coupled out of the laser via the two cleaved mirrors (Figure 1.2−1). The use of heterostructures, first suggested by Kroemer [6], and demonstrated by Alferov *et al.* [7], Panish *et al.* [8] and Kressel *et al.* [9], greatly improves the laser performance. In these structures the recombination active region is bounded by wider bandgap materials with lower index of refraction (Figure 1.2−1). These regions provide both carrier confinement and optical waveguiding, thus reducing the current density needed to obtain lasing (*threshold current density*) by more than one order of magnitude, as compared with homojunction $GaAs$ lasers (1−$3kAcm^{-2}$ *vs.* $\approx 50kAcm^{-2}$). The laser is said to be a Single or Double Heterostructure device *if the active region is bounded by one or two of its sides, respectively, by the wider bandgap regions.*

Semiconductor injection laser diodes were fabricated from several atomic systems. Among these, the $GaAs-Ga_{1-x}Al_xAs$ system is the most widely used and the most technologically developed. As x is increased from zero, the bandgap increases ($\Delta E_g \approx 1.25x$ eV) and *the index of refraction decreases* ($\Delta n \approx -0.62x$). The system is virtually lattice matched for all values of x, which is very important for minimizing interface defects which cause undesirable non−radiative recombination.
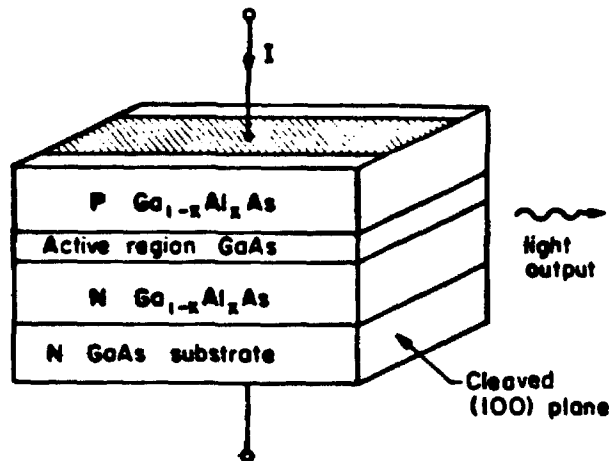
Figure 1.2- 1. Schematic drawing of an AlGaAs Double- Heterostructure injection laser.

The principle of operation of Double−Heterostructure injection lasers is depicted in Figure 1.2-2. Figure 1.2−2a shows the schematic band structure of the laser diode under forward bias conditions. Elec−trons injected from the N−*AlGaAs* layer into the active region are confined by the P−*AlGaAs* otential barrier, and holes injected from the P−*AlGaAs* are confined by the N−*AlGaAs* barrier. As a result, the carriers are trapped in a region which is much narrower than the carrier diffusion length, where the stimulated recombination takes place. Thus the threshold current, being proportional to the volume of the active region is reduced. A further reduction results from the better coupling

between the optical mode and the active region, which is due to the waveguiding mechanism of the low refractive index *AlGaAs* layers (Figure 1.2-2b,c).

N P

$Ga_{1-x}Al_xAs$ GaAs $Ga_{1-x}Al_xAs$

(a)

refractive index

(b)

optical mode intensity

(c)
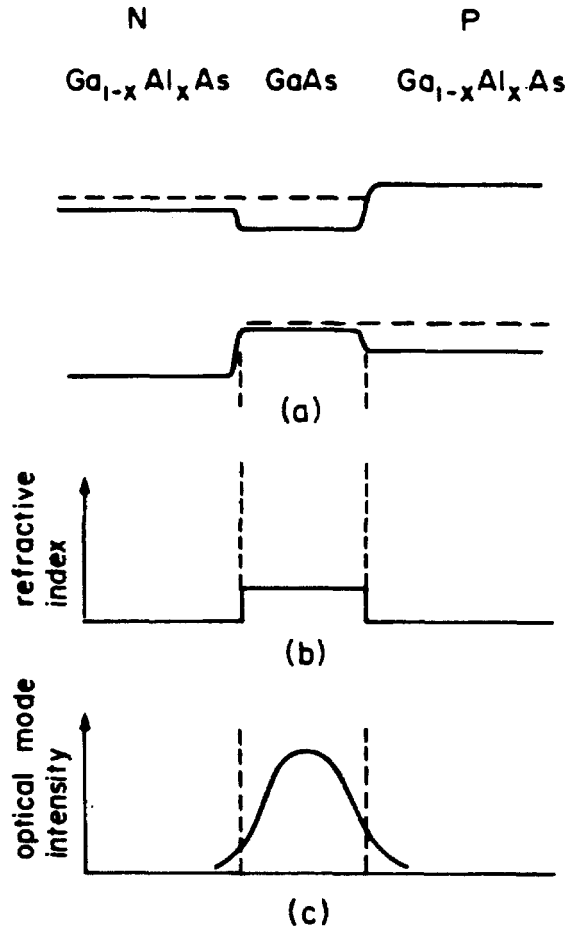
Figure 1.2- 2. Schematic drawing of: a) band diagram under forward bias conditions, b) index of refraction profile, and c) optical mode of a double- heterostructure injection laser diode

Comprehensive treatment of semiconductor injection laser diodes can be found in the books by Kressel and Butler [10], Casey and Panish [11], and Thompson [12].

1.3 Thesis Outline

The main subject of this thesis is the development and characterization of optoelectronic devices that can be applied as sources in optical communication systems. All the devices described here were fabricated of the *AlGaAs* ternary system, using conducting or semi–insulating *GaAs* crystals as substrates. This system is also suitable for fabrication of electronic devices, and thus makes it possible to fabricate integrated optoelectronic devices and circuits.

Chapter 2 describes two devices which, in addition to operating as injection lasers, also perform electronic functions which modulate their light output. The first one, named the Translaser, is a monolithically integrated device which consists of a heterostructure bipolar transistor and an injection laser [13]. The collector current of the transistor directly modulates the laser current, and thus its light output. The second device combines within itself the optical operation of a laser with the electrical operation of a semiconductor controlled rectifier, thus presenting an alternative mode of modulation of laser diodes [14].

In Chapter 3 an investigation of the properties of multi–PN junction heterostructure devices is carried out. This type of device presents an alternative approach for the realization of large optical cavity lasers. An interesting property is that they possess bistable electrical characteristics similar to those of "simple" Shockley–diodes [15].

Two novel structures of laser diodes that can be used as sources for single–mode optical fiber communication are described in Chapter 4.

The first device, the Embedded Stripe Laser [16], involves the application of selective growth techniques. Its structure incorporates two–dimensional waveguiding and carrier confinement in the active region, thus achieving low threshold currents and stable and well defined optical parameters. The second device is a new version of the Buried–Heterostructure laser – with properties similar to the Embedded Stripe Laser– so it can be grown on semi– insulating substrates, thus making it possible to incorporate it in optoelectronic integrated circuits [17].

In the last chapter (Chapter 5), the intrinsic electrical equivalent circuit of the laser diode is developed [18]. The model which is presented provides a better understanding of the operation of the laser diode, which is particularly important in applications which involve its high frequency operation with other electronic components and when a modification of its frequency response is desired.

References for Chapter 1

[1] A. Yariv, "Active Integrated Optics", Proc. Esfahan Symposium on Fundamental and Applied Laser Physics, M. S. Feld, A. Javan, and N. A. Kurnit, eds., Wiley–Interscience, New York (1973), pp 897–919

[2] D. Botez and G. J. Herskowitz, "Components for Optical Communications Systems: A Review", Proc IEEE, **68**, pp 689–731 (1980)

[3] J. R. Pierce, "Optical Channels: Practical Limits with Photon Counting", IEEE Trans. Commun., **COM-26**, pp 1819–1821 (1978)

[4] R. N. Hall, G. E. Fenner, J. D. Kingsley, T. J. Soltys, and R. O. Carlson, "Coherent Light Emission from $GaAs$ Junctions", Phys. Rev. Lett., **9**, pp 366–368 (1962)

[5] M. I. Nathan, W. P. Dumke, G. Burns, F. N. Dill, and G. J. Lasher, "Stimulated Emission of Radiation from $GaAs$ PN Junctions", Appl. Phys. Lett., **1**, pp 62–64 (1962)

[6] H. Kroemer, "A Proposed Class of Heterojunction Lasers", Proc. IEEE, **51**, pp 1782–1783 (1963)

[7] Zh. I. Alferov, V. M. Andreev, V. I. Korol'kov, E. L. Portnoi, and D. N. Tret'yakov, "Injection Properties of $n-Al_xGa_{1-x}As-$ $p-GaAs$ Heterojunctions", Sov. Phys. Semicond., **2**, pp 843–844 (1969)

[8] I. Hayashi, M. B. Panish, and P. W. Foy, "A Low Threshold Room–Temperature Injection Laser", IEEE J. Quant. Electron. **QE-5**, pp 211–212 (1969)

[9] H. Kressel and H. Nelson, "Close Confinement *GaAs* PN Junction Lasers with Reduced Optical Loss at Room Temperature", RCA rev., **30**, pp 106–113 (1969)

[10] H. Kressel and J. K. Butler, *Semiconductor Lasers and Heterojunction Leds*, Academic Press, New York, 1977

[11] H. C. Casey, Jr. and M. B. Panish, *Heterostructure Lasers*, Academic Press, New York, 1978

[12] G. H. B. Thompson, *Physics of Semiconductor Laser Devices*, John Wiley & Sons, Chichester, England, 1980

[13] J. Katz, N.Bar–Chaim, P. C. Chen, S. Margalit, I. Ury, D. Wilt, M. Yust, and A. Yariv "A Monolithic Integration of *GaAs/GaAlAs* Bipolar Transistor and Heterostructure Laser", Appl. Phys. Lett. **37**, pp 211–213 (1980)

[14] J. Katz, N. Bar–Chaim, S. Margalit, and A. Yariv, "*AlGaAs* Hetero-structure Injection Laser S.C.R" Electron. Lett. **16**, pp 840–842 (1980)

[15] J. Katz, N. Bar–Chaim, S. Margalit and A. Yariv, "Large Optical Cavity AlGaAs Lasers with Multiple Active Regions", J. Appl. Phys. **51**, pp 4038– 4041 (1980)

[16] J. Katz, S. Margalit, D. Wilt, and A. Yariv, "Single Growth Embedded Epitaxy *AlGaAs* Injection Lasers with Extremely Low Threshold Currents", Appl. Phys. Lett., **37**, pp 987–989 (1980)

[17] N. Bar–Chaim, J. Katz, I. Ury, and A. Yariv, "Buried–Heterostructure

AlGaAs Lasers on Semi–Insulating Substrates", Electron. Lett., **17**, pp 108–109 (1981)

[18] J. Katz, S. Margalit, C. Harder, D. Wilt, and A. Yariv, "The Intrinsic Electrical Equivalent Circuit of a Laser Diode", IEEE J. Quant. Electron., **QE-17**, pp 4–7 (1981)

2. INTEGRATION AND COMBINED OPERATION OF SEMICONDUCTOR LASERS AND BIPOLAR DEVICES

2.1 Introduction

In virtually all the applications envisaged for the semiconductor injection laser, its light output is to be modulated. One of the main advantages of the semiconductor injection laser is that its light output can be modulated – under certain limitations to be discussed in Chapter 5 – directly, by modulating the current passing through it. This current modulation is usually accomplished by connecting the laser to some electronic circuitry, to which the input modulation signal is applied. In many cases, the modulation source is a low power level one, and thus some amplification is needed so that the output signal will be compatible with the current levels required for a significant modulation of the light output of the laser.

In most of the systems in use today, the laser and its driving circuitry are fabricated on different substrates, or "chips". There are potential advantages in combining all these functions monolithically on a common substrate. All other things being equal, the monolithically integrated device will be more simple to fabricate, will have higher reliability, higher speed, and ultimately lower cost compared to the same circuit made of discrete devices.

Fortunately, the $AlGaAs$ ternary system has properties which makes it a suitable candidate for fabricating both electronic and optical devices. Compared to silicon, the backbone of the electronic industry today,

GaAs is a direct bandgap material (silicon is an indirect bandgap material) so efficient light generating processes are possible in it, and the charge carriers have higher mobilities and shorter lifetimes

Pioneering work in the area of integration of lasers with Metal−Semiconductor−Field−Effect−Transistors (MESFETs) was performed by Yariv and co−workers [1]−[2]. Unlike the various types of FETs, which are majority−type carrier devices, bipolar device operation is usually dominated by diffusion−driven transport mechanism of minority−type charge carriers. FETs are thus potentially faster devices, but it is also possible to fabricate bipolar transistors which have cutoff frequency well within the GHz regime [3]. In addition, the ultimate limit on the frequency response of the combined circuit is likely to be imposed by the laser diode itself (due to an intrinsic resonance in the 1−3 GHz region), and not necessarily by the driving circuitry. Another practical argument in favor of using bipolar transistors is that they are more compatible with conventional digital electronic circuitry (e.g. TTL logic gates), and thus a need for additional electronic circuitry (e.g., level shifters) is eliminated. Integration of semiconductor lasers with bipolar devices is described in this chapter.

Integration of a semiconductor laser and a bipolar transistor is described in Section 2.2. The combined device is named the Translaser [4]. In Section 2.3 another integrated device is described: Injection Laser with a Semiconductor−Controlled−Rectifier [5]. The Translaser belongs to the class of integrated devices, since it involves the combined opera−tion of two distinct devices. The Injection−Laser−SCR, however, is

basically one bipolar device, which combines the electrical operation of an SCR switch with the optical operation of the injection laser. In both cases we have – on a common substrate – a device which performs some electrical function in addition to its optical function.

2.2 The Translaser: A Monolithic Integration of AlGaAs Bipolar Transistor and a Heterostructure Laser

2.2.1 Introduction

One of the common circuits used for driving laser diodes is shown in Figure 2.2-1. The transistor base current generated by the modulation voltage source V_s is amplified by a factor β (β is the common-emitter current gain of the transistor) and the changes in the collector current – which is also the laser current, since they are connected in series – are translated into changes in the light output of the laser. This generic type of a circuit can be used to apply either small-signal or large-signal, digital and analog modulation. The Translaser combines, on a common substrate, both the transistor and the laser – the components that appear inside the dashed box in Figure 2.2-1. The substrate used for this particular device is a Te-doped, n^+- $GaAs$ (100) oriented substrate, although with a minor modification the Translaser can be fabricated also on Cr-doped, Semi- Insulating $GaAs$ substrate. The laser structure employed is a stripe geometry laser formed by a Be-implantation process, as described in detail in the work of Bar-Chaim et al [6].

One of the advantages of the Translaser is that the process used to form the lasers is compatible with the fabrication of heterostructure transistors. This is important for two reasons. First, compatibility usually implies simpler fabricating processes and thus higher devices yields. Secondly, heterostructure transistors having a wide bandgap emitter
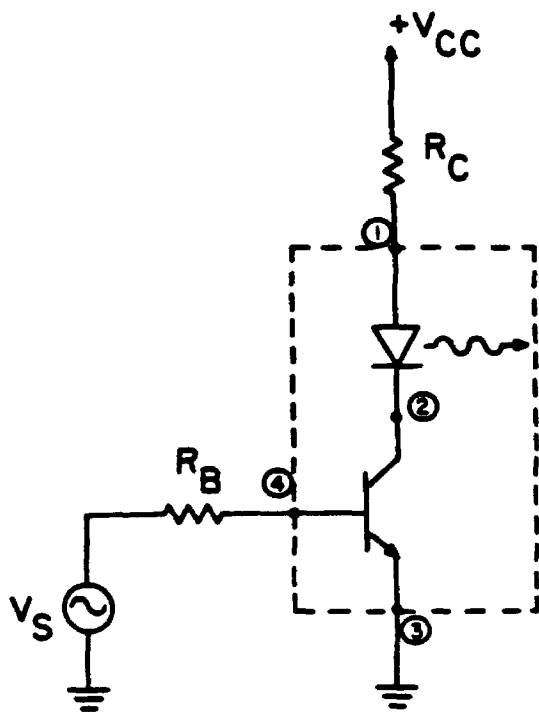
Figure 2.2-1. Laser diode and its driving circuit. The dashed box contains the components integrated in the Translaser

and a narrower bandgap base materials are known to have large common-emitter current gains [7]. The last point will be further elaborated in the next subsection.

2.2.2 Advantages of Heterostructure Transistors

Since the introduction of the idea of the heterostructure transistor [8], and in particular one in which the emitter material has a wider bandgap than the base material, its importance has been recognized,

and operation of devices made of various materials have been demonstrated [7],[9]–[14]. Because of the close lattice match between *GaAs* and *AlGaAs*, heterostructure transistors based on the ternary *AlGaAs* system are particularly attractive because the metallurgical interface at the emitter–base junction does not contain a large density of surface states, and thus does not cause a considerable degradation of the transistor operation. At 300°C, the lattice mismatch between *GaAs* and *AlAs* is only 0.2%.

A typical band structure diagram of a heterostructure laser at thermal electronic equilibrium is shown in Figure 2.2–2a. It is assumed that the spike in the conduction band that should exist at the junction according to the Anderson theory on heterojunctions [15], is actually not there, probably because the junction is not abrupt, as explained by Cheung et al [16]. The advantage of using this type of transistors – compared to homostructure transistors – can be understood from Figure 2.2–2b. This figure depicts the minority carrier concentration distribution across the emitter and base regions of a heterostructure transistor in the active mode of operation under the condition of low–level injection.

The common–emitter current gain (β) is related to the common–base current gain (α) by $\beta=\alpha/(1-\alpha)$. α itself is usually expressed as a product of the emitter injection efficiency and the base transport factor [17]. The last factor is basically the same in both heterostructure and homostructure transistors. The first factor, the emitter injection efficiency (γ) is defined as
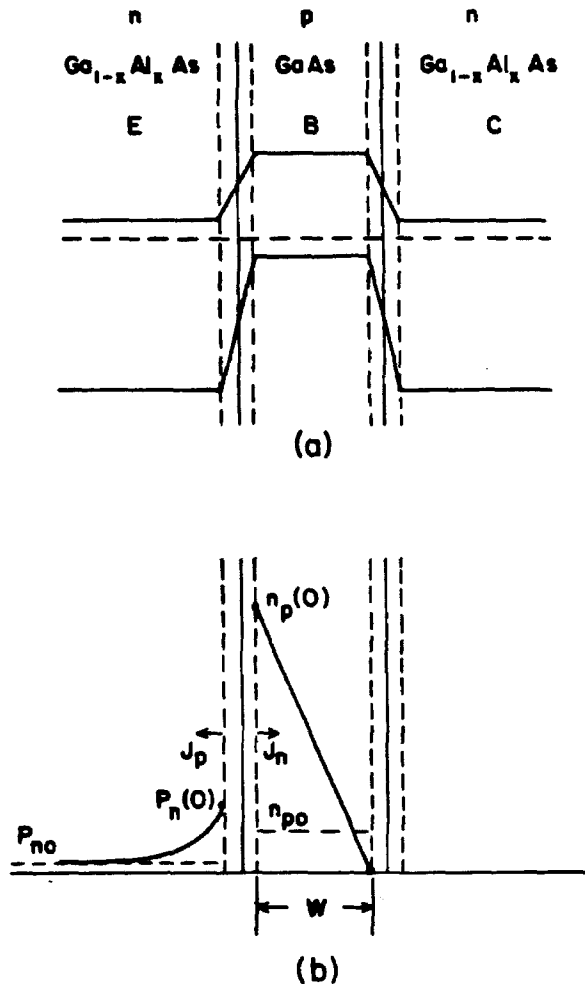
Figure 2.2-2. Heterostructure transistor. a) band structure diagram. b) minority carrier distribution in the emitter and base regions for a transistor operating in the active mode.

$$\gamma \triangleq \frac{minority\ current\ injected\ into\ the\ base}{total\ current\ at\ the\ emitter-base\ junction} = \frac{J_n}{J_n + J_p}$$

$$(2.2-1)$$

where J_n is the electron current density injected from the emitter into the base, and J_p is the hole current density injected from the base into the emitter. Using the notations of Figure 2.2-2b, and assuming that the transistors have narrow bases (i.e., $W << L_B$), J_p and J_n are approximately given by

$$J_n = qD_B \frac{n_p(0)}{W} \qquad\qquad (2.2-2a)$$

$$J_p = qD_E \frac{p_n(0)}{L_E} \qquad\qquad (2.2-2b)$$

where q is the electronic charge, D_B and D_E are the diffusion coefficients of the minority carriers in the base and emitter regions, respectively, $n_p(0)$ and $p_n(0)$ are the excess minority carriers concentration at the edges of the depletion regions of the base and emitter regions, respectively, W is the base width and L_E is the diffusion length of minority carriers in the emitter. For low level injection conditions (which prevail in our case), the expressions for $n_p(0)$ and $p_n(0)$ are:

$$n_p(0) = \frac{n_{iB}^2}{N_A} e^{\Lambda V_{BE}}$$

(2.2−3a)

$$p_n(0) = \frac{n_{iE}^2}{N_D} e^{\Lambda V_{BE}}$$

(2.2−3b)

where $\Lambda \triangleq \frac{q}{KT}$ (K is Boltzmann's constant and T is the absolute temperature), V_{BE} is the voltage applied to the emitter−base junction, n_{iB} and n_{iE} are the intrinsic carrier concentration of the materials of the base and emitter regions, respectively, and N_A and N_D are the doping concentrations in the base and the emitter regions, respectively. From basic semiconductor theory we know that in a given material,

$$n_i^2 = N_C N_V e^{-\frac{E_g}{KT}}$$

(2.2−4)

where N_C and N_V are the effective densities of states in the conduction and valence bands, respectively, and E_g is the energy bandgap in the material. From Equations (2.2−1) to (2.2−4) we obtain the following expression for the emitter injection efficiency:

$$\gamma = \left[1 + \frac{D_E}{D_B} \frac{N_A}{N_D} \frac{W}{L_E} \frac{N_{CE}}{N_{CB}} \frac{N_{VE}}{N_{VB}} e^{-\frac{\Delta E_g}{KT}} \right]^{-1}$$

(2.2−5)

where ΔE_g is the bandgap difference between the materials of the emitter and the base regions. In homostructure transistors $\Delta E_g = 0$, and thus, given W and L_E, one would want to increase N_D and decrease N_A

as much as possible in order to maximize the emitter injection efficiency. However, doing that increases the resistivity of the base region, a fact that can have adverse effects on the transistor operation in terms of increased base resistance and emitter crowding, reduced frequency response and even enhancing the possibility of punch–through phenomenon [18]. However, in heterostructure transistors we have an additional degree of freedom at our disposal, i.e., the bandgap difference ΔE_g between the materials of the emitter and the base. In an $Al_x Ga_{1-x} As/GaAs$ junction at room temperature we have $\Delta E_g/KT \approx 50x$. In regular devices $x \approx 0.3 - 0.4$, so the base doping can be increased, thus improving the overall transistor performance without decreasing the emitter injection efficiency which virtually stays close to its ideal value of unity.

It should be noted that the preceding discussion is inaccurate at low current levels, where the depletion region recombination current must be taken into account. This effect is usually larger in heterostructure transistors than in homostructure transistors because of the larger concentration of recombination centers at the heterointerface. More details will be given in the subsection on the experimental results.

2.2.3 Description of the Translaser

The cross–section of the Translaser is shown schematically in Figure 2.2–3. The basic building block of the device is a $250-\mu m$–wide (and about $300-\mu m$–long) region defined in a liquid–phase–epitaxy (LPE)–grown $n - AlGaAs/p - GaAs/n - AlGaAs$ double–heterostructure.
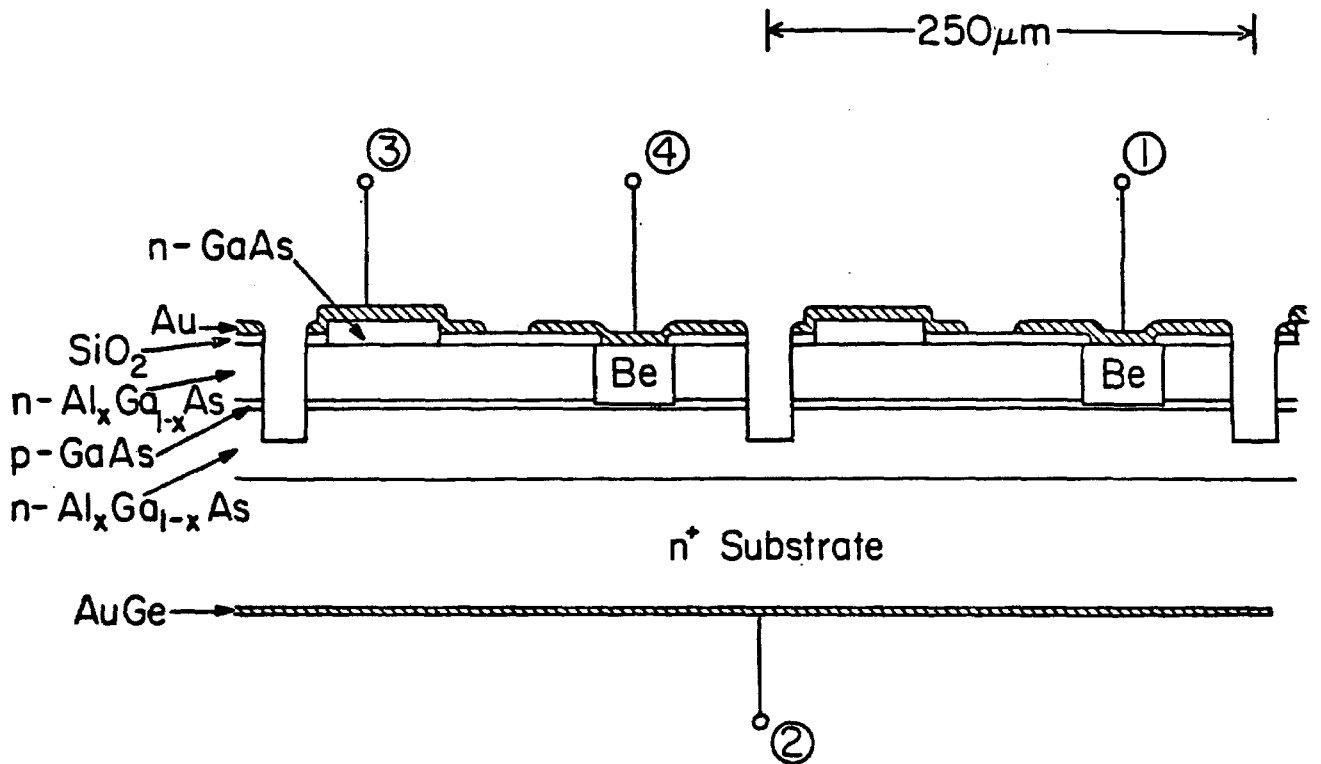
Figure 2.2- 3. Schematic cross- section of the Translaser.

The compatibility between the laser and the transistor manifests itself by the fact that each unit can operate independently as either an injection laser or as a bipolar transistor. In the first case, terminal 1 is the anode terminal of a Be-implanted laser and terminal 2 (the common substrate) is the laser cathode (terminal numbers refer to Figure 2.2-1). In the second case, terminal 3 is the emitter of the transistor, terminal 2 is the collector of the transistor and the base contact (terminal 4) is formed via the Be-implanted region. It is important to note that the

laser is structurally a bipolar transistor operated with the base as the positive terminal, while the emitter terminal is left floating. The usual assignment of the terminals is shown in Figure 2.2−1. Another point worth noting is that in some of the previous works [14], [19], the base of the transistor was contacted directly after etching the top $AlGaAs$ layer. Because of the small thickness of the base region ($\approx 0.25 \; \mu m$), the subsequent alloying of the collector contact can damage the collector−base junction and increase the leakage current. In the translaser this problem is solved by implementing the contact to the base by means of a Be-implantation, the same implantation that defines the stripe in a Trans−laser unit that is to be operated as a laser. In a later work by Ankri et al [20] the base contact was achieved by a diffusion process.

2.2.4 Fabrication Procedure

The fabrication of the device starts with the growth of four layers on an $n^{+}-GaAs$ substrate by liquid−phase−epitaxy (LPE), using the conventional single−slider graphite−boat apparatus [21]. The growth is done in H_2 atmosphere, with oxygen concentration of less than 0.5 ppm. The initial growth temperature is $800°C$ and the cooling rate is usually $0.4°C/\min$. The typical layers thicknesses, aluminum contents (x) and doping are shown in Table 2.2−1.

Following the growth, the upper $GaAs$ contact layer is removed by etching with 1:8:8 (H_2SO_4:H_2O_2:H_2O) solution in the region to be implanted, in order to assure diffusion of the Be−implanted stripe down to the active region. After deposition of 2500 Å of SiO_2 film on the

TABLE 2.2- 1. Growth parameters of the layers of the Translaser

Function of the Layer		Type	Thickness	Al Contents	Doping	
Laser	Transistor		$[\mu m]$	(x)	Dopant	Conc.$[cm^{-3}]$
Lower cladding	Collector	n	3.0	0.4	Sn	1×10^{17}
Active region	Base	p	0.25	0.0	Ge	1×10^{18}
Upper cladding	Emitter	n	1.0	0.4	Sn	1×10^{18}
	Emitter contact	n	0.7	0.0	Sn	$\gtrsim 1 \times 10^{18}$

wafer (the deposition temperature is 370°C), it is coated with a layer of photoresist (Shipley AZ−1350Z), in which stripes of width 6 μm are opened photolithographically. After etching the SiO_2 in these openings ($\approx$ 25 seconds in Buffer−HF solution, made by Transene Co., Inc.), a 100 KeV Be−implantation is performed at room temperature with a dose of $3 \times 10^{15} cm^{-2}$. After removal of the photoresist mask, the wafer is annealed for 40 minutes at 800°C. This results in diffusion of the $Be-$ implanted stripe down to, but not beyond the $GaAs$ active region (or base region). This is in accord with the results of Bar−Chaim et al [6] that the beryllium diffusion depth is strongly dependent on the aluminum content of the material, so that the diffusion process is virtually self− terminating at the $GaAs$ layer. Because of the use of the pho−

toresist as an implanting mask above the SiO_2 layer, the Be−implanted region has a minimal lateral diffusion, which is a desirable feature for obtaining lasers with low threshold currents. (For a laser structure with a given threshold current density, the threshold current is proportional − with some limitations − to the stripe width of the laser).

As the next step, a shallow Zn diffusion from a $ZnAs_2$ source (20 minutes at 640°C in a sealed ampule evacuated to 10^{-6} $torr$) is performed in the Be−implanted region which makes for a good ohmic contact to the base and active regions. After this diffusion, the ohmic contact to these regions is achieved by evaporation of Cr and Au. This is followed by opening of 100 μm−width windows down to the top $GaAs$ layer (by etching $\approx$ 5 seconds in Cr−etchant [40 ml HCl +2 gr $Hydrazine$ $Dihydrochloride$ $(H_2NNH_2 2HCl)$] followed by $\approx$ 10 seconds in Au−etchant [113 gr KI + 65 gr I_2 + 100 ml H_2O]). An evaporation of $AuGe$ and Au is then performed to form the emitter contact of the transistor. The emitter contact is separated from the base contact by etching the metals between them in a stripe of 10−μm−width (using Au−etchant and Cr−etchant as described before). The individual Translaser units are then isolated from each other by etching another 10−μm−wide stripe in the wafer down to the lower $AlGaAs$ layer. Thus each laser is isolated from the base and emitter of the neighboring transistors. The etchant used was 1:8:8 $(H_2SO_4:H_2O_2:H_2O)$. The substrate is then lapped (down to thickness of 70 to 100 μm) and deposited with $AuGe$ alloy (88% Au, 12% Ge) and Au, followed by alloying at 380°C. Finally the wafer is cleaved into individual columns, each containing several Translaser units with

length of about $(250 \pm 50)\mu m.$

2.2.5 Experimental Results

2.2.5.1 The Transistor

A typical collector current versus collector-emitter voltage curve is shown in Figure 2.2-4.
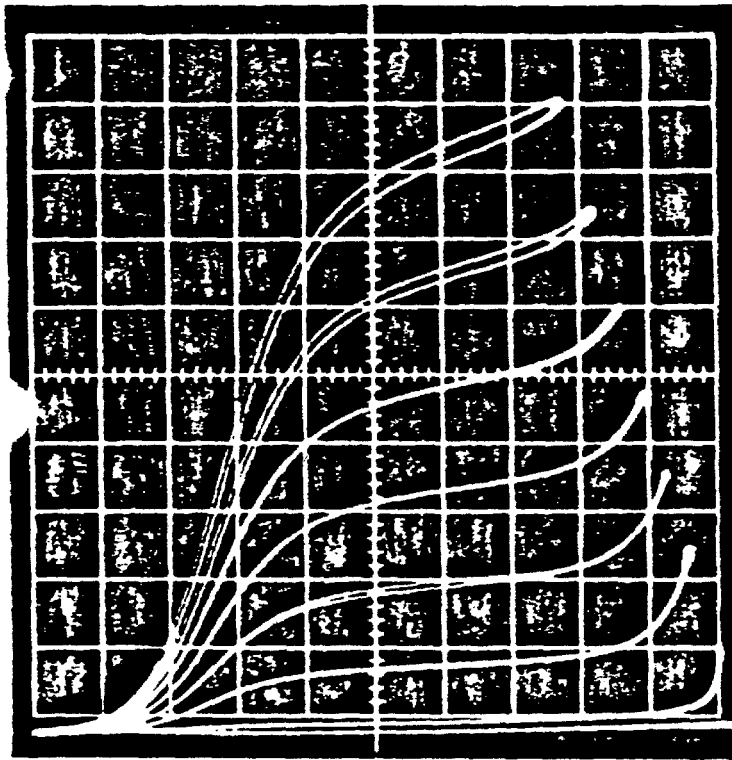
Figure 2.2-4. Typical collector current versus collector-emitter voltage curve of a heterostructure bipolar transistor.(horizontal scale: 0.5 V/div; vertical scale: 10 mA/div; base current: 20μA/step, with the lower curve corresponding to $I_B = 0\mu A$)

The transistor was tested at current levels up to 200 mA. Figure 2.2-5

shows the typical dependence of the DC current gain β_{DC} on the collector current I_C.

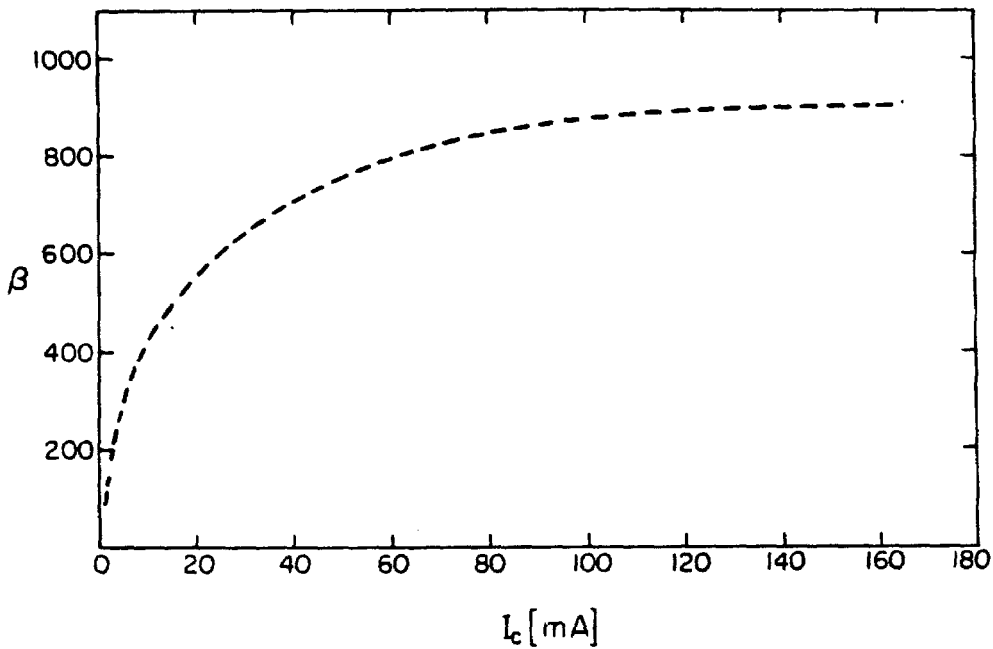**Figure 2.2-5.** Typical common-emitter current gain versus collector current bias point curve.

At low current levels ($\lesssim$ 100 Acm^{-2}) the value of β_{DC} increases with current. As mentioned before, the reason that β_{DC} is not constant is the existence of recombination current at the emitter–base junction deple–

tion region. In order to analyze this effect, we first define I_D as the usual expression of the diode current, given by

$$I_D = I_S(e^{\Lambda V_{BE}} - 1) \approx I_S e^{\Lambda V_{BE}} \qquad (2.2-6)$$

and I_R as the depletion region recombination current, given by

$$I_R = I_{RO} e^{\dfrac{\Lambda V_{BE}}{N_E}} \qquad (2.2-7)$$

where V_{BE} is the base–emitter voltage, N_E is a constant, (usually $1 \leqslant N_E \leqslant 3$). I_{RO} is a phenomenological recombination current constant, and I_S is the diffusion saturation current, given by

$$I_S = \frac{q n_i^2 D_B A_E}{N_A W} \qquad (2.2-8)$$

where n_i is the intrinsic carrier concentration in $GaAs$ and A_E is the emitter area. In our case $n_i = 1.1 \times 10^7 cm^{-3}$, $D_B = 100 cm^2 sec^{-1}$, $A_E = 3 \times 10^{-4} cm^2$, $N_A = 1 \times 10^{18} cm^{-3}$ and $W = 0.25 \mu m$, which gives $I_S = 2 \times 10^{-20} A$, or equivalently, $J_S \triangleq \dfrac{I_S}{A_E} = 8 \times 10^{-17} A - cm^{-2}$.

If we now define I_{CL} as the value of the collector current at which the value of β_{DC} drops to one half of its high–current value (β_0), we can solve for I_{RO} [22]. A good approximation for high values of β_{DC} is

$$\beta_{DC} = \frac{I_C}{I_B} = \frac{I_S e^{\Lambda V_{BE}}}{\dfrac{I_S e^{\Lambda V_{BE}}}{\beta_0} + I_{RO} e^{\frac{\Lambda V_{BE}}{N_E}}} \qquad (2.2\text{−}9)$$

$$= \frac{\beta_0}{1 + \beta_0 \dfrac{I_{RO}}{I_S} e^{\Lambda V_{BEL}(\frac{1}{N_E} - 1)}} \qquad (2.2\text{−}10)$$

At $I_C = I_{CL}$ we have

$$I_{CL} \approx I_S e^{\Lambda V_{BEL}} \qquad (2.2\text{−}11)$$

and

$$\beta_0 \frac{I_{RO}}{I_S} e^{\Lambda V_{BEL}(\frac{1}{N_E} - 1)} = 1 \qquad (2.2\text{−}12)$$

Combining Equations (2.2−11) and (2.2−12), we obtain

$$I_{RO} = \frac{1}{\beta_0} I_{CL}^{1 - \frac{1}{N_E}} I_S^{\frac{1}{N_E}} \qquad (2.2\text{−}13)$$

The value of N_E can be found from the slope of the $\log\beta$ vs. $\log I_C$ curve at low current levels. From Equation (2.2−9) we see that in this current regime $\beta_{DC} \propto I_C^{1 - \frac{1}{N_E}}$, provided that $\beta_{DC} \gg 1$. From the experimental results we obtain $N_E \approx 2.2$, which is a reasonable value. Values ranging from 1.1 to 2.5 are reported by Konagi et al [7], [14]. For

$N_E = 2.2$, $I_{CL} = 12mA$ and $\beta_0 = 910$, we obtain $I_{RO} = 1.2 \times 10^{-13}A$, or

equivalently, $J_{RO} \triangleq \dfrac{I_{RO}}{A_E} = 4 \times 10^{-10}Acm^{-2}$. It is interesting to note that

I_{RO} is about 7 orders of magnitude larger than I_S. For example, in Si

homostructure transistors, I_{RO} is typically only 3 orders of magnitude

larger than I_S.

From simplified calculations it is found that the recombination

current density constant J_{RO} is given by [23].

$$J_{RO} = \frac{qW_d n_i}{2\tau_{REC}} \qquad\qquad (2.2\text{--}14)$$

where W_d is the width of the depletion region at the emitter–base junc–

tion and τ_{REC} is the lifetime of the carriers. At $I_C = I_{CL}$ $W_d \approx 600\text{Å}$,

which yields $\tau_{REC} \approx 13\ ns$. This is a reasonably accurate result, taking

into account the fact that first, it is only a simplified model, and second,

that the value of J_{RO} is very sensitive to changes in N_E. For example, a

change of less than 5 percents in N_E (from 2.2 to 2.3) results in more

than 50 percent change in τ_{REC} (from 13 ns to 6 ns). For currents above

60 mA, the values of β_{DC} remains approximately constant. The value of

β_{DC} at the high collector current regime (β_0) is about 900, which is in a

good agreement with the theoretical value as limited by the base tran–

sport factor, i.e.

$$\beta_0 = (\frac{2L_B}{W})^2 \qquad\qquad (2.2\text{--}15)$$

with L_B, the diffusion length of the minority carriers in the base, equals about 4 μm [24].

2.2.5.2 The Laser

The laser section of the Translaser is a stripe geometry laser. The particular structure employed is a modified version of the first Be-implanted laser [6]. In that laser, all the layers that were grown in the LPE process were of n-type, while in the Translaser, the center $GaAs$ layer is of p-type, since it has to serve also as a base of an NPN transistor. In order to optimize the operation of the transistor, the base doping was increased to 1×10^{18} cm^{-3}. However,even this high doping level is not high enough to cause a substantial increase in the free-carrier optical absorption at the active region of the laser [25]. This is due to the fact that under lasing conditions, the carrier concentration in the active region exceeds 1×10^{18}, and furthermore, more absorption is caused by electrons which have smaller effective mass as compared to holes.

Threshold currents of the lasers were as low as 55 mA, with 60 mA being a typical value for a 250-μm cavity length devices. This value is comparable to the results obtained by Bar–Chaim et al [6], so it can be concluded that replacing the n-type active region by a p-type one does not cause any significant degradation in the performance of the laser, although the increased base doping can slightly increase the carrier loss outside of the stripe region. As will be discussed in Chapter 5, carrier loss mechanisms can improve the laser frequency response function.

The near-field and the far-field radiation patterns in the direction parallel to the junction plane are shown in Figures 2.2-6 and 2.2-7, respectively.
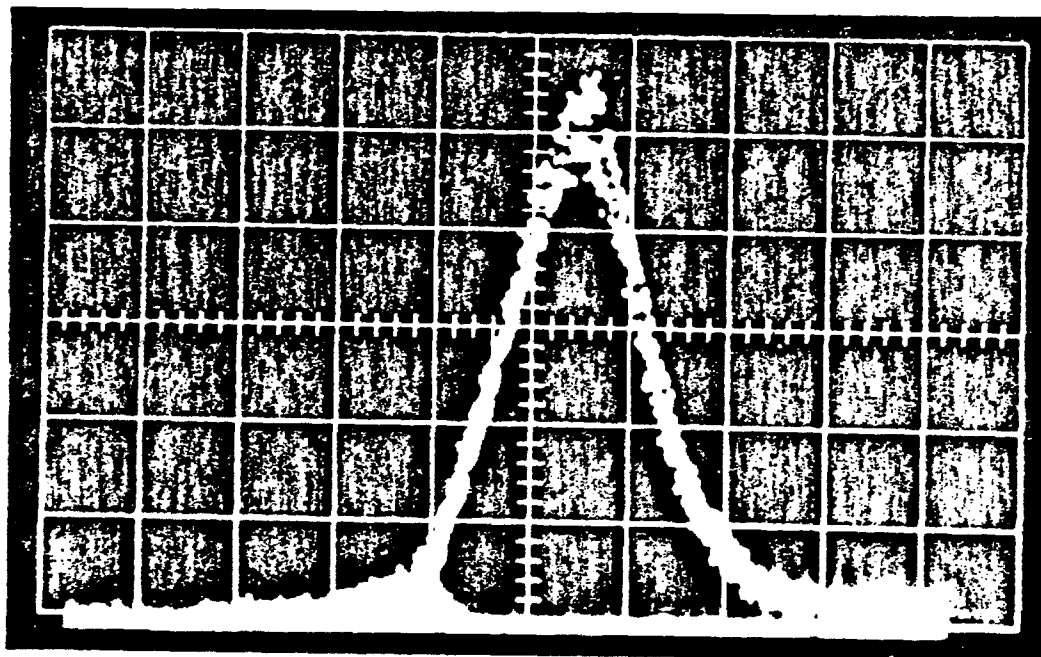
Figure 2.2- 6. Near field radiation pattern of the laser. (horizontal scale is 2.7 μm/div)

Both exhibit single spatial mode behavior. The half width of the near field intensity pattern is about 5 μm, and the half width angle of the far-field pattern is about 6°. On the basis of these results it can be concluded that the laser is mainly gain-guided. Lasers with the same physical dimensions but with real index guiding, usually have a wider far field pattern, and they often oscillate in a higher order spatial mode. Furthermore, only lasers with gain guiding have astigmatism in their radiation
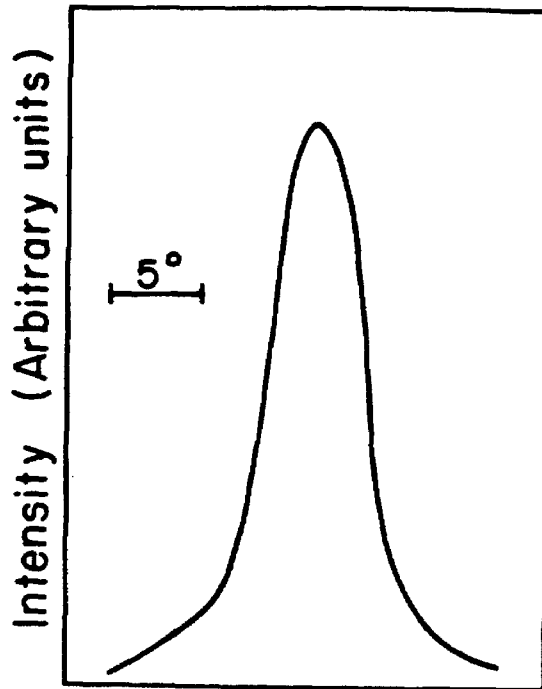
Figure 2.2- 7. Far field radiation pattern of the laser.

beam. Using the formulae given by Casey and Panish [26] we obtain that the magnitude of the real index difference is smaller than 5×10^{-4}, and probably less. The lasers operate in a small number of longitudinal modes. Single longitudinal mode operation of this type of lasers was achieved for devices with narrower ($\lesssim 4 \mu m$) stripes.

The light versus current characteristics of the laser is linear up to 10 mW output power, and no self-pulsations were observed after a few hundred hours of operation. The external differential quantum efficiency (η_D) is defined for current levels above threshold as

$$\eta_D = \frac{\Delta(carriers\ injected\ into\ the\ laser)}{\Delta(photons\ emitted\ out\ of\ the\ laser)} = \frac{2q\lambda}{hc}\frac{\Delta P_L}{\Delta I_L} \qquad (2.2-16)$$

was measured to be above 40%. In Equation (2.2−16) λ is the emission wavelength, h is Planck's constant, c is the vacuum light velocity, P_L is the optical power emitted from one facet of the laser, and I_L is the current flowing through the device.

2.2.5.3 Combined Operation of the Translaser

The Translaser was operated as one unit both in pulsed and CW modes of operation. In the later case, it was mounted with Indium on a Copper block heat−sink with the substrate side down. CW threshold currents were found to be about 20% higher than the pulsed threshold currents, in agreement with [27].

The temporal response of the Translaser was tested using an RCA C30902E Avalanche−Photodiode (APD) and a pulse generator with a 1 ns rise−time. Taking into account the risetimes of the pulse generator and the APD, the intrinsic rise−time of the Translaser under these conditions is 1.1 ns, corresponding to modulation rates of about 300 MHz. (Opera−tion of faster $AlGaAs$ heterostructure transistors have been demon−strated [19], [20]). This value is limited by the parameters of the device, as discussed in the following paragraph. The cutoff frequency (f_T) of a transistor, which is defined as the frequency at which the short−circuit current gain β in the common emitter configuration is unity, is given by [19]

$$\frac{1}{2\pi f_T} = \frac{C_{TE} + C_{TC}}{\Lambda I_C} + R_S C_{TC} + \tau_B + \tau_C \qquad (2.2-17)$$

where C_{TE} and C_{TC} are the transition capacitances of the collector-base and the emitter-base junctions, respectively, R_S is the sum of the collector series resistance and the collector and emitter contact resistances, τ_B is the base transit time, and τ_C is the collector depletion region transit time. Equation (2.2-17) is derived from the hybrid-π transistor model, which is reasonably accurate for frequencies up to about $f_T/3$. In our case $C_{TE} \approx 36 pF$, $C_{TC} \approx 16 pF$, $R_S \approx 10\Omega$, $I_C \approx 70 mA$, $\tau_B \approx 10 pS$, and $\tau_C \approx 5 pS$, which yields $f_T \approx 820$ MHz.

Since in our case the limiting factor for f_T is the $R_S C_{TC}$ term in Equation (2.2-17), the time response can be improved by fabricating transistors with smaller areas (and thus reducing the capacitance), and by using improved contacting techniques, which can reduce the contact resistances from $\approx 1 \times 10^{-4}\Omega - cm^2$ by more than one order of magnitude (and thus reducing the total series resistance). At that point, the other terms in Equation (2.2-17) begin to limit f_T. However, this limit occurs at frequencies of several gigahertz. For example, reduction of the area by a factor of 4 and the series resistance by a factor of 10 results in increasing f_T to about 8.4 GHz.

Another important figure of merit of a transistor is the maximum frequency of oscillations, f_{max}, at which the power gain of the transistor is unity. f_{max} is given by [3]

$$f_{max} = \left[\frac{f_T}{8\pi r_B C_{TC}} \right]^{\frac{1}{2}} \qquad (2.2-18)$$

r_B is the base spread resistance, given by

$$r_B = \frac{\rho_{SB}}{12} \frac{H}{L} \qquad (2.2-19)$$

where ρ_{SB} is the base region sheet resistance, H is the emitter width and L is the emitter length. In our case $r_B \approx 35\Omega$, which yields $f_{max} \approx$ 240 MHz. f_{max} can be improved by using a base electrode structure more suitable for high frequency applications, in which the H/L ratio is much smaller. For example, a transistor with an interdigital electrode structure with a 5 times smaller H/L ratio (in addition to all the other improved parameters as described above) will have f_{max} of about 3 GHz.

2.2.6 *Further Applications of the Translaser*

Because of the inherent versatility of the Translaser, various devices can be made by using more than several Translaser units on the same column. Some of the possible applications are shown in Figure 2.2-8. By connecting two transistors in a Darlington-pair configuration, much higher current gains are achieved, and the laser can be driven even from a low-level modulation sources (Figure 2.2-9a). Of course, there is the usual trade-off between gain and speed of response.

If an additional fabrication step is employed, so that the base contact of the first transistor in the darlington pair is removed, the result-

(a)   (b)   (c)
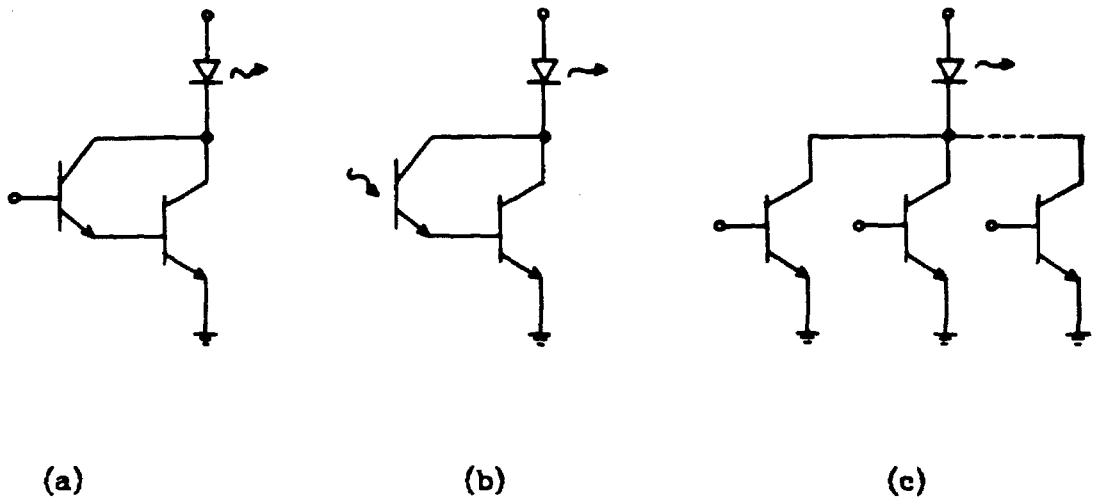
Figure 2.2- 8. Possible applications of the Translaser. a) Darlington-pair Trans-
laser. b) High-gain optical repeater. c) Opto-electronic 'OR' gate.

ing device will operate as a monolithically integrated optical repeater
(figure 2.2–9b). Monolithically integrated optical repeater, based on
MESFET detector and amplifier, has recently been reported by Yust et al
[28].

Another configuration is shown in Figure 2.2–9c. This device
operates as an opto–electronic "OR" gate. The laser emits light when an
electrical input signal is applied to at least one of the base terminals. In
this case no additional internal connections are needed, since the

collectors of all the transistors are part of the common substrate.

As a final remark, it should be noted that with a minor modification the Translaser can be fabricated also on Semi–Insulating (SI) substrates. Since the collector terminal is usually not needed for external contacting, this requires only the growth of an additional n^+–$GaAs$ layer on the SI substrate. More details on devices grown on SI substrates are given in Section 4.3.

2.3 AlGaAs Injection Laser - Semiconductor - Controlled - Rectifier Switch

2.3.1 Introduction

An alternative method for driving injection lasers, which is particularly suitable for medium speed pulsed applications, is by using an SCR as a switch, as depicted in Figure 2.3-1. The SCR is basically a $p - n - p - n$-structure device. Several *GaAs* and *AlGaAs* $p - n - p - n$ light-emitting devices have been reported recently [29]-[35]. However, all these are electrically two-terminal devices: they are either optically activated, or they switch when the voltage imposed upon them exceeds their breakover voltage value. The device described in this section combines the operation of an *AlGaAs* heterostructure injection laser with the electrical operation of an SCR, i.e., this is a three terminal device, where the switching is accomplished by applying a control signal to the gate electrode, in the usual mode of operation of conventional SCR devices. We can look on the combined device as a laser switch.

2.3.2 Principles of SCR Operation

A basic SCR structure and its basic current-voltage characteristics are shown in Figure 2.3-2. Under forward bias condition the device has two stable states, and thus it can operate as a switch. Referring to Figure 2.3-2, in region "A" the SCR is in the forward-blocking, or "OFF" state. The middle (NP) junction (J2) is reverse-biased, and virtually all the applied voltage develops across it. In region "C" the device is in the second stable state-the forward conducting, or "ON" state. All the junctions are forward-biased, so the voltage drop across the device is only
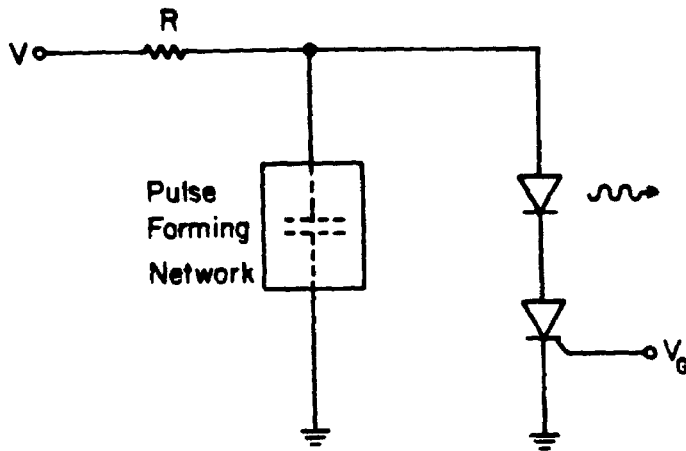
Figure 2.3- 1. Laser driving circuit using semiconductor-controlled rectifier.

slightly larger than a voltage drop across a forward−biased *pn* junction. Region "B" is an unstable state of the SCR, in which it switches between the two stable states, and thus possesses negative differential resistance. The switching point between the two stable states depends on the magnitude of the gate current I_C. The switching voltage with $I_C = 0$ is defined as the *brekover voltage* (V_{BO}) of the SCR. The minimum current required to maintain the SCR in the "ON" state is defined as the *holding current* (I_H) of the SCR. In the reverse−biased direction, regions "D" and "E" are the reverse− blocking and the reverse breakdown regions, respectively, and they usually bear little importance to the normal mode of operation of the SCR.

The fact that the SCR posseses two stable states can be shown by using the two−transistor model representation for the device [36]. From
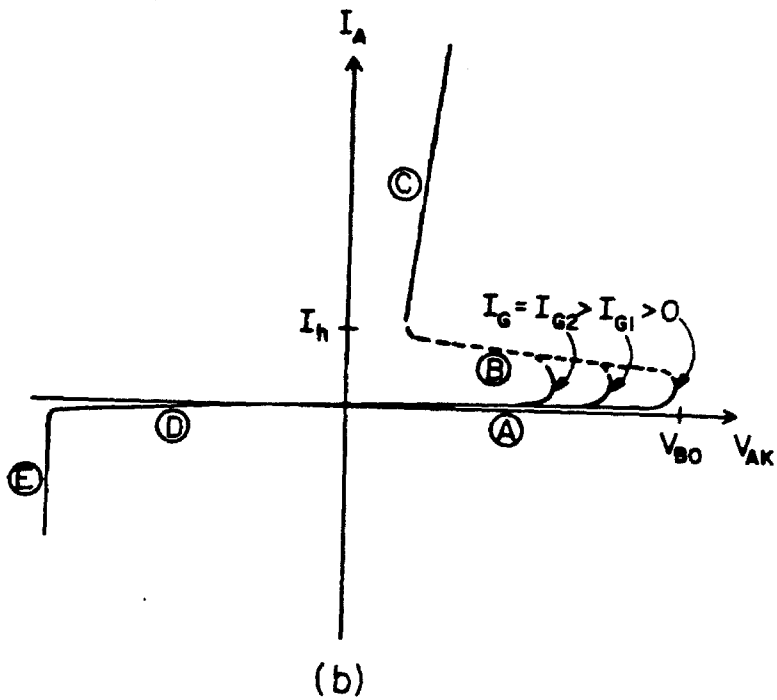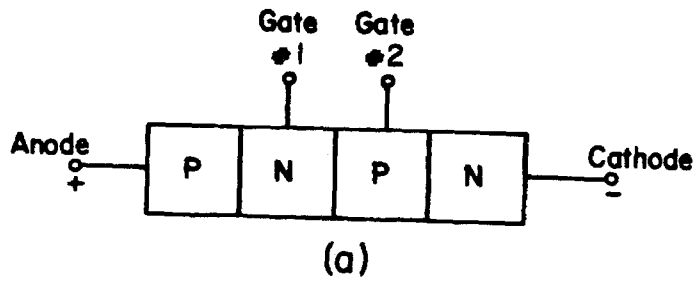
Figure 2.3- 2. a) Schematic structure of an SCR. b) Current–Voltage curve of an SCR.

Figure 2.3–3 we can clearly see how this model is derived.

Following the signs convention and the current definitions in Figure 2.3–3c, the circuit equations for the model are
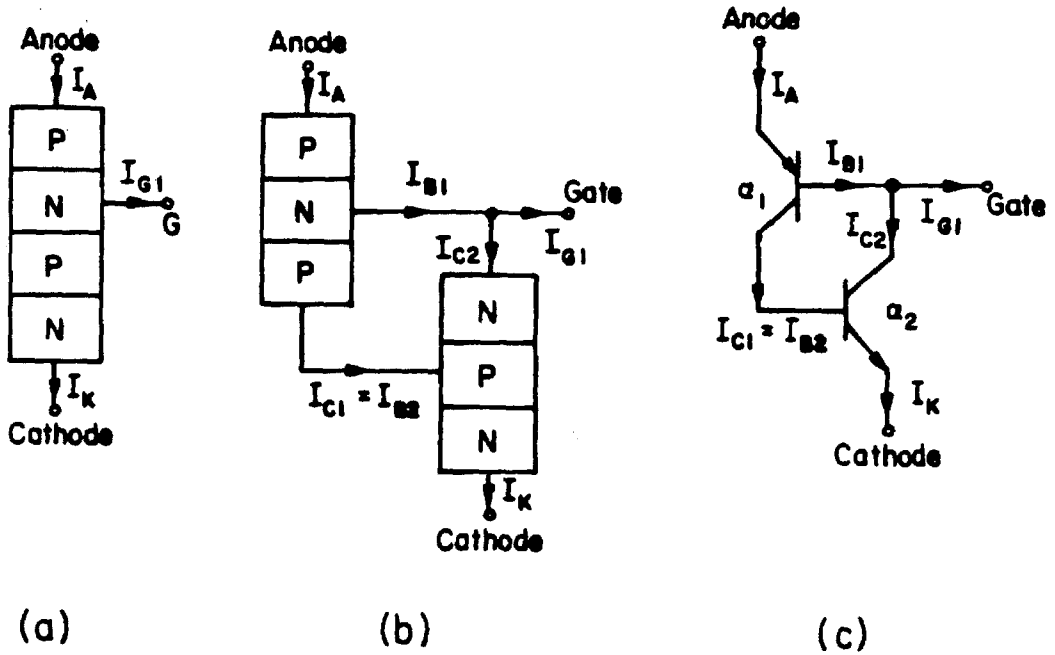
Figure 2.3- 3. Derivation of the two- transistor model for the SCR. a) SCR structure. b) conceptual decomposition of the SCR. c) two—transistor model.

$$I_{Ci} = \alpha_i I_{Ei} + I_{COi} \qquad i = 1, 2$$

$$(2.3-1)$$

$$I_{B1} + I_{C1} = I_{C2} \qquad I_{C1} = I_{B2} \qquad I_A = I_{E1}, \qquad I_K = I_{E2} \qquad (2.3-2)$$

where α_i is the common base current gain of the i-th transistor, and I_{COi} is the collector to base reverse saturation current of the i-th transistor. Combining Equations (2.3-1) and (2.3-2) the following

expression for the anode current I_A is obtained:

$$I_A = \frac{I_{CO1} + I_{CO2} + (1-\alpha_2)I_{C1}}{1- \alpha_1 - \alpha_2} \qquad (2.3-3)$$

It is clearly seen that when $\alpha_1 + \alpha_2 = 1$, I_A approaches infinity, which indicates the bistability of the device.

An actual solution of the SCR characteristics must take into account the physical phenomena which are essential to the SCR operation: the dependence of α on the current, and the avalanche multiplication in the depletion region of the center junction. A more accurate description employs the graphical analysis method by Gibbons [37]. Referring to the notations in Figure 2.3-4, the current I through the device is

$$I = M[I_p(x_1) + I_n(x_2)] \qquad (2.3-4)$$

where M is the avalanche multiplication factor (assumed to be the same for electrons and holes, as is the case in GaAs) and the subscripts p and n refer to the hole and electron currents, respectively.

Using the transistors equations [Equation (2.3-1)],

$$I_p(x_1) = \alpha_1(I_A)I_A + I_{CO1} \qquad (2.3-5a)$$

$$I_n(x_2) = \alpha_2(I_K)I_K + I_{CO2} \qquad (2.3-5b)$$
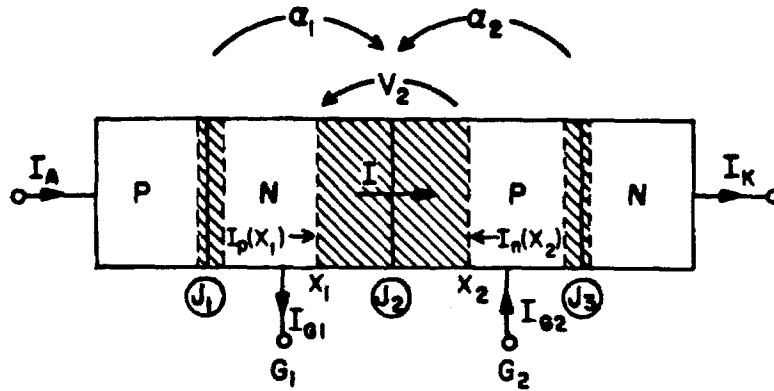
Figure 2.3- 4. Schematic structure of a generalized SCR device.

and the relations $I = I_K$ and $I_A = I + I_{G1}$ (In our case $I_{C2}=0$, as can be seen from Figure 2.3-3 and 2.3-5), Equations (2.3-4) and (2.3-5) can be combined to yield

$$\frac{1}{M(V_2)} = \alpha_1(I + I_{G1}) + \alpha_2(I) + \frac{I_{CO1}+I_{CO2}-\alpha_1(I+I_{G1})I_{G1}}{I} \qquad (2.3-6)$$

$$\triangleq f(I,I_{G1})$$

where M is usually given by the empirical expression

$$M(V_2) = \left[1 - \left(\frac{V_2}{V_{BD}} \right)^c \right]^{-1} \qquad\qquad (2.3\text{-}7)$$

(V_{BD} is the breakdown voltage of the junction and c is an empirical parameter, usually also a function of V_2 [38]). Equations (2.3-6) and (2.3-7) can be solved graphically, and the result is the $I - V$ curve of the device [37].

2.3.3 Description and Operation Principles of the Injection-Laser-SCR

A schematic cross-section of the structure of the combined device is shown in Figure 2.3-5a, and the schematic symbol of the device is shown in Figure 2.3-5b. The functions of the various layers in the operation of the laser and the SCR are described in Table 2.3-1. The upper emitter-base junction of the device is a homojunction, formed by Zinc diffusion in the upper AlGaAs cladding layer. The lower emitter-base junction is a heterojunction at the interface of the active region and the lower cladding layer.

In the forward-blocking ("OFF") state, the current flowing in the device is the reverse bias leakage current of the heterojunction between the active region and the upper cladding layer. Due to the low intrinsic carrier concentration in GaAs and AlGaAs, and the depletion region recombination current, the current dependence on the voltage follows approximately an $\exp(\frac{qV}{2KT})$ law up to quite high injection levels. This lowers the overall sensitivity of the device, since it takes more current to obtain the "ON" voltage on the junction than the current it would have
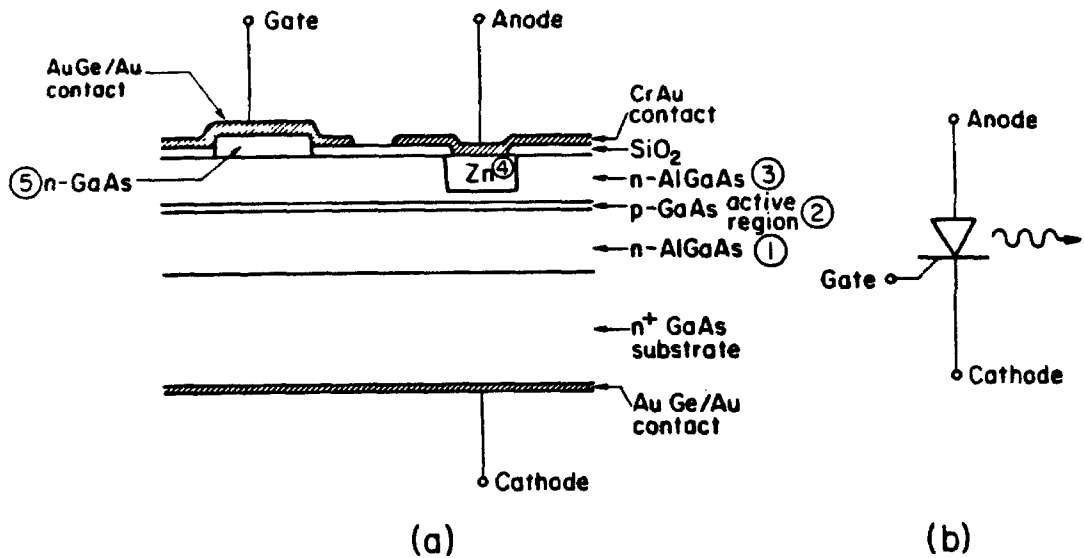
Figure 2.3-5. a) Schematic cross-section of the Injection Laser- SCR. b) The symbol of the combined device.

taken if the junction followed the conventional $\exp(\frac{qV}{KT})$ law. On the other hand, SCR devices fabricated from *GaAs* are less sensitive to high temperatures because of their large bandgap, and they are inherently faster than *Si* SCRs because the carrier lifetime is shorter.

In the forward-conducting ("ON") state, all the junctions of the device are forward-biased. Electrons are injected into the active region

TABLE 2.3- 1. Functional table of the regions of the injection- laser- SCR. The indexing of the various regions refers to Figure 2.3- 5a.

Region	Function of the Region	
	Laser	SCR
1. lower $n - AlGaAs$	lower cladding	lower emitter
2. $p - Ge$	active region	lower base
3. upper $n - AlGaAs$	upper cladding	upper base
4. Zn- diffusion		upper emitter
5. upper $n - GaAs$		contact layer

across the heterojunction at the lower emitter, and holes are injected from the upper emitter and flow through the upper cladding layer to the active region. This is basically a remote–junction structure, similar to a structure which was discussed recently by Kobayashi et al [39]. Loss of carriers in the upper cladding layer is negligible because the minority carrier concentration in that layer is lower than in $GaAs$ by a factor of $e^{-\frac{\Delta E_g}{KT}}$, where ΔE_g is the difference in energy bandgaps of the materials of the upper cladding layer and the active region. This results in an insignificant increase in the threshold current of the laser. The laser structure itself is basically that of the common oxide–stripe laser with

zinc diffusion.

2.3.4 Fabrication Procedure

Some of the processing steps are common to the fabrication of the Laser–SCR and the Translaser. Missing details can be found in the sub-section describing the fabrication procedure of the Translaser.

The fabrication of the Laser–SCR starts with the growth of four layers on an n^+– $GaAs$ substrate by liquid–phase–epitaxy. Typical layer thicknesses, aluminum contents and doping are given in Table 2.3–2.

TABLE 2.3- 2. Growth parameters of the layers of the injection laser SCR

Layer number (Fig. 2.3- 5a)	Type	Thickness [μm]	Al contents (x)	Doping Dopant	Conc. [cm^{-3}]
1	n	3.0	0.4	Sn	5×10^{16}
2	p	0.25	0.0	Ge	1×10^{18}
3	n	2.0	0.4	Sn	5×10^{16}
4	n	0.7	0.0	Sn	$\gtrsim 1\times10^{18}$

The contact layer is removed in the region where the Zn is to be diffused. This makes it possible to achieve a larger degree of control of the subsequent diffusion process. After deposition of 2500 Å of SiO_2 on the wafer, it is coated with photoresist in which stripes of width of 7 μm are opened. After the etching of the SiO_2 in these openings and removing

the photoresist, Zn is diffused in vacuum at 640°C for 20 minutes, followed by an annealing of the wafer at 800°C for 30 minutes. This results in diffusion of the Zn down to a distance of about $0.5\mu m$ above the active region, in agreement with the results of Lee et al [40]. The distance between the diffusion front and the active region is chosen to be as small as possible in order to minimize carriers loss in the upper base region, while still maintaining the fabrication process under control. If the diffusion front reaches the active region, the device will still operate as a laser [41],[42], but the electrical mode of operation is then that of a diode and not an SCR. During the Zn−diffusion the stripes widen up to about $10\mu m$ because of lateral diffusion and undercut below the SiO_2 film.

An evaporation of $Cr − Au$, etching the SiO_2 above the $GaAs$ contact layer, and an evaporation of $AuGe/Au$, form the anode and gate contacts, respectively, of the SCR. The gate contact is separated from the anode contact by etching the metal contact between them in a $10\mu m$ stripe. The substrate is consequently lapped, and the substrate side of the wafer is deposited with $AuGe$ and Au, followed by alloying at 380°C. Finally $300\mu m$−long individual devices are cleaved from the wafer.

2.3.5 *Experimental Results*

First we calculate the common−base current gain α of the two transistors which model the SCR, in order to see if it can possess two stable states. α is given by $\alpha = \gamma t_B$, where t_B is the base transport factor, is given by [17]

$$t_B \triangleq \frac{\text{minority current reaching the collector}}{\text{minority current injected into the base}}$$

$$= [\cosh(\frac{W}{L_B})]^{-1} \qquad\qquad (2.3\text{-}8)$$

where L_B is the diffusion length of the minority carriers in the base region. The expression for γ is given by Equation (2.2-5). (For transistors without very narrow bases, the factor W in that equation should be replaced by $L_B\tanh(\frac{W}{L_B})$). From Equations (2.3-8) and (2.2-5) we obtain $\alpha = 0.998$ for the lower transistor and $\alpha = 0.98$ for the upper transistor. So we see that at moderately high current levels $\alpha_1 + \alpha_2 > 1$. At low current levels the opposite condition (i.e., $\alpha_1 + \alpha_2 < 1$) holds, of course, because of the depletion region recombination current, so we can conclude that the device will demonstrate a bistable behavior. This behavior can be clearly seen in Figure 2.3-6a, which depicts the anode current versus anode–cathode voltage (I_A vs. V_{AK}) curve, with the gate current I_G as a parameter. The breakover voltage (V_{BO}) of the device is about 8V and the holding current (I_H) is about 1 mA. V_{BO} can change from one device to another because the differences in the amount of leakage currents. As the magnitude of the gate current pulse is increased, the device switches at lower voltages. This can be understood with the aid of Equation (2.3-3): as I_G is increased, I_A is increased. Since both α_1 and α_2 are themselves monotonically increasing functions of I_A at this region, for example due to avalanche multiplication in the depletion region of the middle junction, it takes less voltage to satisfy

(a)

(b)
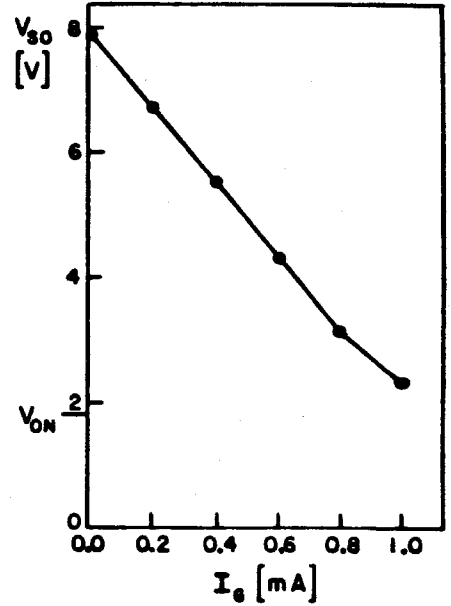
Figure 2.3- 6. a) Typical I_A vs. V_{AK} curve of an injection laser- SCR switch. (horizontal scale: 1V/div; vertical scale: 1 mA/div; gate-current scale: 200μA/step).b) Switching voltage vs. I_C.

the switching condition as I_C is increased. A typical switching voltage versus gate current is shown in Figure 2.3–6b.

The laser has similar properties to other oxide stripe lasers. Threshold currents are typically about 100 mA, and their optical properties, including near-field and far-field patterns, are similar to those of the

Be-implanted lasers, leading to the conclusion that they are gain—guided. Operation in a single transverse mode was obtained up to about $1.5 \times I_{th}$.

References for Chapter 2

[1] I. Ury, S. Margalit, M Yust, and A. Yariv, "Monolithic Integration of an Injection Laser and a Metal Semiconductor Field Effect Transistor", Appl. Phys. Lett., **34**, pp 430−432 (1979)

[2] D. Wilt, N. Bar−Chaim, S. Margalit, I. Ury, M. Yust, and A. Yariv, "Low Threshold *Be* Implanted *(GaAl)As* Laser on Semi- Insulating Substrate", IEEE J. Quant. Electron., **QE-16**, pp 390−391 (1980)

[3] G. O. Ladd and D. L. Feucht, "Performance Potential of High−Frequency Heterojunction Transistors", IEEE Trans. Electron. Devices, **ED-17**, pp 413−420 (1970)

[4] J. Katz, N.Bar−Chaim, P. C. Chen, S. Margalit, I. Ury, D. Wilt, M. Yust, and A. Yariv "A Monolithic Integration of *GaAs/GaAlAs* Bipolar Transistor and Heterostructure Laser", Appl. Phys. Lett., **37**, pp 211−213 (1980)

[5] J. Katz, N. Bar−Chaim, S. Margalit, and A. Yariv, "*AlGaAs* Heterostructure Injection Laser S.C.R" Electron. Lett., **16**, pp 840−842 (1980)

[6] N. Bar−Chaim, M. Lanir, S. Margalit, I. Ury, D. Wilt, M. Yust, and A. Yariv, "*Be*−Implanted *(GaAl)As* Stripe Geometry Lasers", Appl. Phys. Lett., **36**, pp 233−235 (1980)

[7] M. Konagi, K. Katsukawa, and K. Takahashi, "*(GaAl)As/GaAs* Heterojunction Phototransistors with High Current Gain", J. Appl. Phys., **48**, pp 4389−4394 (1977)

[8] W. Shockley, U.S. Patent No. 2569347, 1951

[9] D. K. Jadus and D. L. Feucht, "The Realization of a *GaAs−Ge* Wide Band Gap Emitter Transistor", IEEE Trans. Electron. Dev., **ED-16**, pp 102−107 (1969)

[10] H. J. Hovel and A. G. Milnes, *"ZnSe−Ge* Heterojunction Transistors", IEEE Trans. Electron. Dev., **ED-16**, pp 766−774 (1969)

[11] W. P. Dumke, J. M. Woodall, and V. L. Rideout, *"GaAs−GaAlAs* Heterojunction Transistor for High Frequency Operation", Solid−State Electron., **15**, pp 1339−1343 (1972)

[12] Zn. I. Alferov, F.A. Akhmedov, V. I. Korol'ov, and V.G. Nikitin, "Photo-transistor Utilizing *GaAs−AlAs* Heterojunction", Sov. Phys.−Semicond., **7**, pp 780−782 (1973)

[13] M. T. Brian, *"CdS−Si* Wide−Band−Gap Emitter Transistors", J. Phys. D, **8**, pp 543−550 (1975)

[14] M. Konagi and K. Takahashi, *"(GaAl)As−GaAs* Heterojunction Transistors with High Injection Efficiency", J. Appl. Phys., **46**, pp 2120−2124 (1975)

[15] R. L. Anderson, "Experiments on *Ge−GaAs* Heterojunctions", Solid State Electron., **5**, pp 341−351 (1962)

[16] D. T. Cheung, S. Y. Chiang, and G. L. Pearson, "A Simplified Model for Graded−Gap Heterojunctions", Solid State Electron., **18**, pp 263−268 (1975)

[17] S. M. Sze, *Physics of Semiconductor Devices*, Wiley, New York, 1969, pp 270–272

[18] A. G. Milnes and D. L. Feucht, *Heterojunctions and Metal Semiconductor Junctions*, Academic Press, New–York 1972, ch 3

[19] J. P. Bailbe, A. Marty, P. H. Hiep, and G. E. Rey, 'Design and Fabrication of High–Speed *GaAlAs/GaAs* Heterojunction Transistors", IEEE Trans. Electron. Dev., **ED-27**, pp 1160–1164 (1980)

[20] D. Ankri and A. Scavennec, 'Design and Evaluation of a Planar *GaAlAs–GaAs* Bipolar Transistor", Electron. Lett., **16**, pp 41–42 (1980)

[21] H. C. Casey, Jr. and M. B. Panish, *Heterostructure Lasers*, Academic Press, New York, 1978, Part B, pp 119–124

[22] J. Choma Jr. and J. L. Burns, 'Spice Macromodel for the Integrated Bipolar Junction Transistor", to be published in IEEE Trans. Electron. Dev.

[23] Ref. [17], pp 102–104

[24] H. C. Casey, Jr., B. I. Miller, and E. Pinkas, 'Variation of Minority –Carrier Diffusion Length with Carrier Concentration in *GaAs* Liquid Phase Epitaxial Layers", J. Appl. Phys., **44**, pp 1281–1287 (1973)

[25] Ref. [21], Part A, pp 174–176

[26] Ref. [21], Part B, pp 240–252

[27] H. Yonezu, T. Yuasa, T. Shinohara, T. Kamejima, and I. Sakuma, "CW Optical Power from (AlGa)As Double Heterostructure Lasers", Japan. J. Appl. Phys., **15**, pp 2393−2402 (1976)

[28] M. Yust, N. Bar−Chaim, S. H. Izadpanah, S. Margalit, I. Ury, D. Wilt, A. Yariv, "A Monolithically Integrated Optical Repeater", Appl. Phys. Lett., **35**, pp 795−797 (1979)

[29] D. Meyerhoffer, A. S. Keiser, and H. Nelson, "A Light−Activated Semiconductor Switch", J. Appl. Phys., **38**, pp 111−123 (1967)

[30] W. F. Kosonocky, R. H. Cormeli, and I. J. Heghi, "Multilayer GaAs Injection Laser", IEEE J. Quant. Electron., **QE-4**, pp 176−179 (1968)

[31] Y. Arai, M. Sakuta, and K. Sakai, "GaAs Light Emitting Device with Light Activated Negative Resistance", Japan. J. Appl. Phys., **9**, pp 853−854 (1970)

[32] H. F. Lockwood, K. −F. Etzold, T. E. Stockton and D. P. Marinelli, "The GaAs P−N−P−N Laser Diode", IEEE J. Quant. Electron., **QE-10**, pp 567−569 (1975)

[33] Z. I. Alferov, F. A. Akhmedov, V. I. Korol'kor, and A. A. Yakovenko, "Electroluminescent Photothyristors Based on GaAs Heterostructure Laser", Sov. Phys. Semicond., **7**, pp 1127−1130 (1975)

[34] C. P. Lee, A. Gover, S. Margalit, I. Samid, and A. Yariv, "Barrier− Controlled Low−Threshold P−N−P−N GaAs Heterostructure Laser" Appl. Phys. Lett., **30**, pp 535−538 (1977)

[35] J. A. Copeland, A. G. Dentai, and T. P. Lee, "P−N−P−N Optical Detec−

tors and Light Emitting Diodes", IEEE J. Quant. Electron., **QE**-14, pp 810–813 (1978)

[36] J. J. Ebers, "Four–Terminal P–N–P–N Transistors", Proc. IRE, **40**, pp 1361–1364 (1952)

[37] J. F. Gibbons, "Graphical Analysis of $I-V$ Characteristics of Generalized P–N–P–N Devices", Proc. IEEE, **55**, pp 1366–1374 (1967)

[38] R. Leguerre and J. Urgell, "Approximate Values of the Multiplication Coefficient in One–Sided Abrupt Junctions", Solid State Electron., **19**, pp 875–881 (1976)

[39] T. Kobayashi and Y. Furukawa, "Recombination Enhanced Annealing Effect in $AlGaAs/GaAs$ Remote Junction Heterostructure Lasers", IEEE J. Quant. Electron., **QE**-15, pp 674–684 (1979)

[40] C. P. Lee, S. Margalit, and A. Yariv, "Dependence of Zn Diffusion on the Al Concentration in $Ga_{1-x}Al_xAs$", Solid State Electron., **21**, pp 905–907 (1978)

[41] H. Yonezu, Y. Matsumoto, T. Shinohara, I. Sakuma, T. Suzuki, K. Kobayashi, R. Lang, Y. Nannichi, and I. Hayashi, "New Stripe Geometry Laser with High Quality Lasing Characteristics by Horizontal Transverse Mode Stabilization–a Refracting Index Guiding with Zn Doping", Japan. J. Appl. Phys., **16**, pp 209–210 (1977)

[42] G. H. B. Thompson, D. F. Lovelace, and S. E. H. Turley, "Deep Zn Diffused $(GaAl)As$ Heterostructure Stripe Laser with Twin Transverse Junctions for Low Threshold Current and Kink–Free

Light Characteristics", IEEE J. Quant. Electron., **QE-15**, pp 772–775 (1978)

3. MULTI- PN JUNCTION HETEROSTRUCTURE DEVICES

3.1 Introduction

Since their introduction, the Shockley–diode [1] and other related devices have found many applications in switching and regulating circuits [2]. Recently the operation of Shockley–diodes which function also as *AlGaAs* injection lasers has been demonstrated [3], [4]. The basic description of the operation of PNPN devices can also be found in Section 2.3, where a combination of an injection laser with a semiconductor controlled rectifier is described. Operation of a homostructure multi– *PN GaAs* device as an injection laser has also been reported [5], but no analysis of the electrical or optical properties of the device was given.

This chapter analyzes the electrical and optical properties of semiconductor devices consisting of many layers of alternating P and N type. It is found that such devices provide an alternative for realizing bistable switching devices. Since the electrical "gain" is distributed among all the regions of the structure, different switching conditions are obtained. Mainly we find that it takes more "gain" to perform the switching, which results in an increase in the breakover voltages and in the holding currents. The electrical gain referred to in the last sentence is the common–base current gain of the transistors that represent these devices, as will be explained later in this chapter. This type of device can also find application in making *AlGaAs* injection lasers with more than one active region [6].

The outline of the chapter is as follows. In Sections 3.2 and 3.3, the

electrical and optical properties, respectively, of the multi–PN devices are analyzed. Finally, Section 3.4 describes the fabrication procedure and the experimental results of several types of such devices, and com– pares the experimental results with the theoretical calculations. Appen– dix A reviews the solution of the diffusion equation in a uniform region with general boundry conditions, and Appendix B presents a numerical method, based on the finite–element–method, for solving general two dimensional waveguide problems.

3.2 Electrical Properties of Multi- PN Structures

3.2.1 Modified Transistor Model for Multi–PN Structures

Consider a structure consisting of $2m$ layers of alternating P and N type. This structure, as shown schematically in Figure 3.2–1, is denoted by $(PN)_m$.
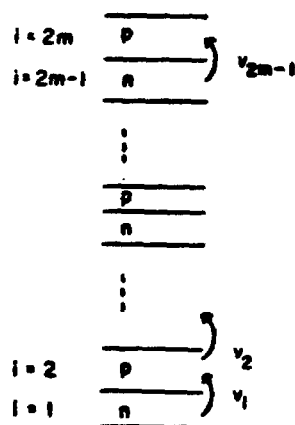

Figure 3.2- 1. Schematic drawing and notations for a $(PN)_m$ structure.

By a direct extension of the two–transistor model for the SCR, one can analyze the structure using a more complicated transistor network. An example of a $(PN)_3$ structure is shown in Figure 3.2–2. Generally, it takes a $2\times(m-1)$ transistor network to describe a $(PN)_m$ structure. Using the sign convention and notation of Figure 3.2–3, the $3\times2\times(m-1)$ equations needed to describe the network (three equations for each
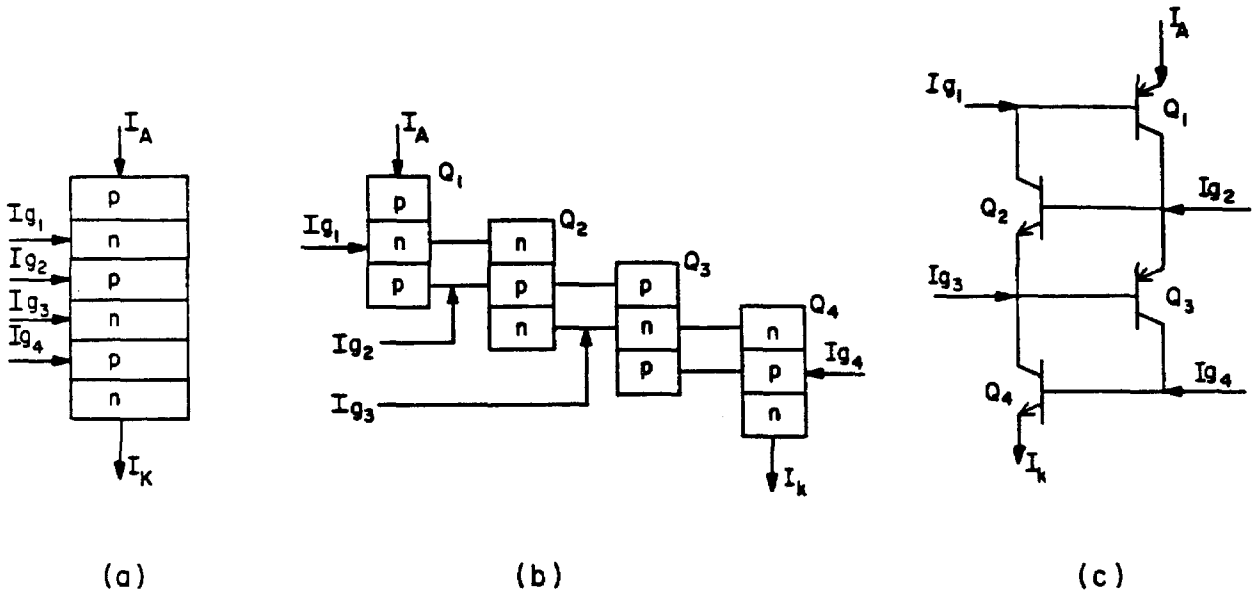
Figure 3.2- 2. Transistor model of a $(PN)_3$ device. a) Schematic structure of the device. b) Decomposition of the device into individual transistors. c) Equivalent circuit of the device.

transistor) are:

$$I_{Bi} + I_{Ci} = I_{Ei}, \qquad i = 1, 2, \ldots, 2(m-1) \tag{3.2-1a}$$

$$I_{Ci} = \alpha_i I_{Ei} + I_{COi}, \qquad i = 1, 2, \ldots, 2(m-1) \tag{3.2-1b}$$

$$I_{Ci} = I_{B,i-1} + I_{E,i-2} + I_{C,i-1}, \qquad i = 2, 4, 6, \ldots, 2(m-1) \tag{3.2-1c}$$

$$I_{Ei} = -I_{B,i-1} + I_{C,i-2} + I_{C,i-1}, \qquad i = 3, 5, 7, \ldots, 2m-3$$
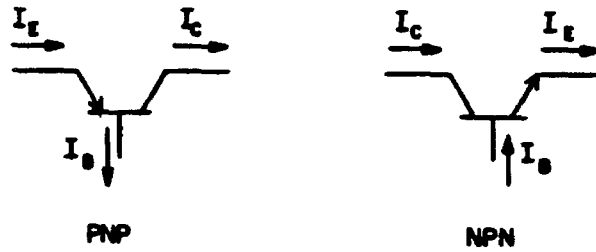
Figure 3.2- 3. Sign convention for the currents in the transistors [used in Equation (3.2- 1)].

$$(3.2-1d)$$

$$I_{E1} = I_{E, 2m-2} - \sum_{i=1}^{i=2m-2} I_{Gi} \qquad (3.2-1e)$$

where the transistors are assumed to be initially in the cutoff or active region (i.e., the device is in the forward blocking state). I_{COi} is the collector to base reverse saturation current of the i-th transistor, α_i is the common-base current gain of the i-th transistor, and I_{Gi} is the current generated at the i-th gate of the device. The set of equations (Equation 3.2-1) can be cast in a matrix form

$$\mathbf{A}\,\overline{I} = \overline{I}_{\text{drive}} \qquad (3.2-2)$$

For example, the $(PN)_3$ structure is described by the following matrix equation. A is given by

$$
\begin{vmatrix}
1 & 0 & 0 & 0 & 0 & 0 & 0 & 0 & 0 & -1 & 0 & 0 \\
1 & -1 & -1 & 0 & 0 & 0 & 0 & 0 & 0 & 0 & 0 & 0 \\
-\alpha_1 & 0 & 1 & 0 & 0 & 1 & 0 & 0 & 0 & 0 & 0 & 0 \\
0 & -1 & 0 & 0 & 0 & 1 & 0 & 0 & 0 & 0 & 0 & 0 \\
0 & 0 & 0 & 1 & -1 & -1 & 0 & 0 & 0 & 0 & 0 & 0 \\
0 & 0 & 0 & -\alpha_2 & 0 & 1 & 0 & 0 & 0 & 0 & 0 & 0 \\
0 & 0 & -1 & 0 & 1 & 0 & 1 & 0 & 1 & 0 & 0 & 0 \\
0 & 0 & 0 & 0 & 0 & 0 & 1 & -1 & -1 & 0 & 0 & 0 \\
0 & 0 & 0 & 0 & 0 & 0 & -\alpha_3 & 0 & 1 & 0 & 0 & 0 \\
0 & 0 & 0 & -1 & 0 & 0 & 0 & -1 & 0 & 0 & 0 & 1 \\
0 & 0 & 0 & 0 & 0 & 0 & 0 & 0 & 0 & 1 & -1 & -1 \\
0 & 0 & 0 & 0 & 0 & 0 & 0 & 0 & 0 & -\alpha_4 & 0 & 1
\end{vmatrix}
\qquad (3.2-3)
$$

and $\overline{I}$ and $\overline{I}_{drive}$ are given by

$$
\overline{I} =
\begin{vmatrix}
I_{E1} \\
I_{B1} \\
I_{C1} \\
I_{E2} \\
I_{B2} \\
I_{C2} \\
I_{E3} \\
I_{B3} \\
I_{C3} \\
I_{E4} \\
I_{B4} \\
I_{C4}
\end{vmatrix}
\qquad
\overline{I}_{drive} =
\begin{vmatrix}
-\sum I_{Ci} \\
0 \\
I_{CO1} \\
I_{G1} \\
0 \\
I_{CO2} \\
I_{G2} \\
0 \\
I_{CO3} \\
I_{G3} \\
0 \\
I_{CO4}
\end{vmatrix}
$$

Equation (3.2-2) can be solved for $I_A = I_{E1}$ with $\{\alpha_i\}$ as a set of parameters. The particular case where I_A approaches infinity (i.e., the determinant of A equals zero) indicates the switching condition. Inspection of the matrix A in Equation (3.2-2) shows the following:

$(PN)_m$ structures, with $m \geq 2$, can not possess more than two stable states. This is deduced from the fact that for a given structure,

only one set of $\{\alpha_i\}$, at most, yields $I_A \to \infty$.

The condition for switching changes, depending on the structure parameters. Some of the results are shown in Figure (3.2-4). It is clearly seen that as m increases, the device must have more gain in order to possess two stable states. Structures without enough gain remain in the forward blocking state, and when the applied voltage is increased they eventually undergo either avalanche or zener breakdown. One simple explicit expression is obtained for the case where all the transistors have the same gain, i.e., $\alpha_1 = \alpha_2 =, \ldots, \triangleq \alpha$. In this case switching occurs in a $(PN)_m$ structure when

$$\alpha = 1 - \frac{1}{m} \qquad\qquad (3.2-4)$$

For $m = 2$ we get the well known result for the SCR ($\alpha_1 = \alpha_2 = 0.5$).

As a final remark, it is interesting to note that the above analysis can be also carried out for multi-PN structures in which the first layer and the last layer are of the same type (e.g., a $PNPNP$ structure). In this case it is found that the device behvior does not show bistability, and thus it is similar to a transistor. It seems that all generic types of one-port low-freqency low-field semiconductor devices are described by one of the following structures: P (or N), PN, PNP (or NPN) and $PNPN$.

Figure 3.2-5 helps to explain this fact. In particular, it describes why both $(PN)_3$ and $(PN)_{2)}$ devices have the same basic characteristics. Figure 3.2-5a depicts the device in the forward blocking ("OFF") state. The cross-hatched areas represent the depletion regions of the reverse biased junctions (J_2 and J_4). The junction J_3 is, in principle, forward
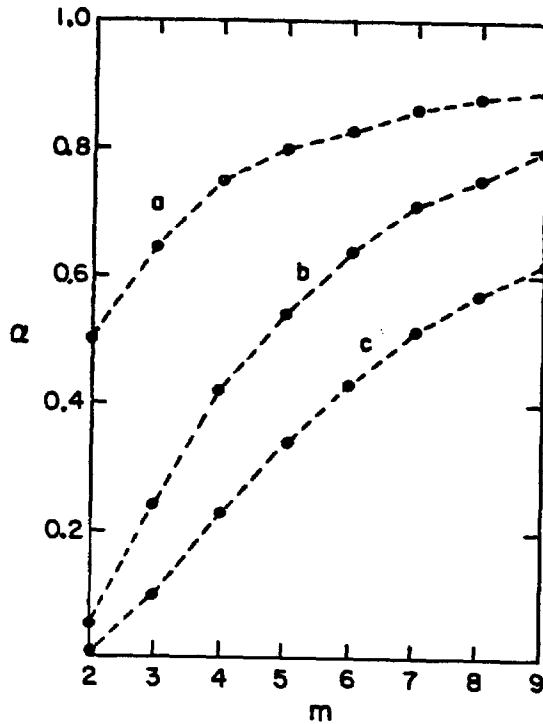
Figure 3.2- 4. Common base current gain (α) for switching of a $(PN)_m$ device versus m. a) All the transistors are identical $(\alpha_i=\alpha)$. b) All the odd (or all the even) numbered transistors in the model have $\alpha=0.95$. Shown is α needed from the other transistors for switching. c) Same as in b), but with a given α of 0.99.

biased. However, since the current that flows through the device is very small, there is also a very small voltage drop in the region between J_2 and J_4. Since a region with virtually no current and voltage has a little effect on the device, to the external world the device appears basically as
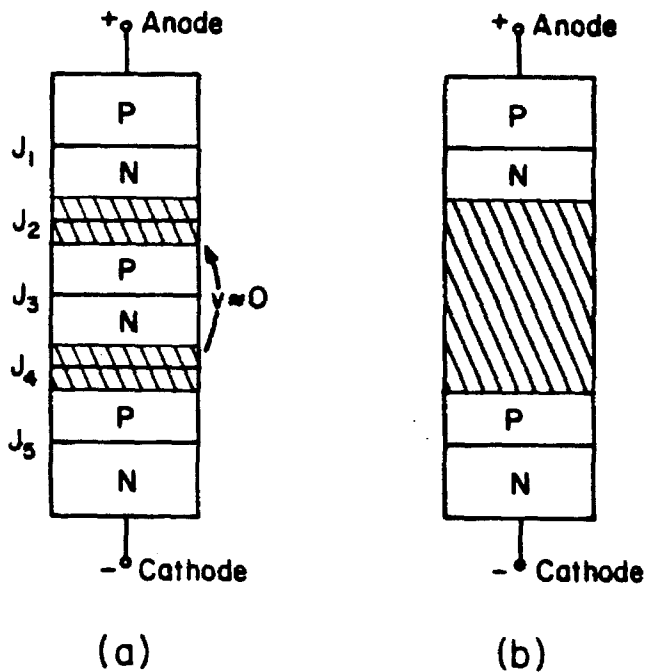
Figure 3.2 5. Comparison between the generic characteristics of $(PN)_3$ and $(PN)_2$ devices. a) $(PN)_3$ device. b) corresponding $(PN)_2$ device. (regular Shockley diode).

if it had the structure depicted in Figure 3.2-5b, which is a $(PN)_2$ device. In the forward conducting ("ON") state, all the internal regions in the $(PN)_3$ device are in saturation, which is the same situation as in the $(PN)_2$ device. Of course, the quantitative analysis is different for the two cases, as can be seen from the next two subsections.

3.2.2 Solution of Diffusion Equation in the Forward Blocking ('OFF')
State

In this section we will analyze the $(PN)_m$ structure in the forward

blocking state. In this section and in the next one, the indices on the

various parameters refer to either the junctions (e.g. voltages,depletion-

region recombination currents) or to the layers between the junctions

(e.g. diffusion lengths,widths of the layers). As can be seen from Figure

3.2-1, the i-th junction separates the i-th and the $(i+1)$-th layers. The

minority carriers distribution in the forward blocking ("OFF") state is

shown in Figure 3.2-6. All the even-numbered junctions are reverse-

biased so that the minority carriers concentration at them is effectively

zero. The equation for the current density through the reverse-biased

junctions is

$$J = J_{2i} = M_{2i}[J_{G,2i} + J_{p,2i+1}(W) + J_{n,2i}(0)], \quad i = 1, 2, \ldots, (m-1)$$

$$(3.2-5)$$

M_{2i} is the avalanche multiplication in the depletion region of the

$2i$-th junction, which, for $GaAs$, is the same for both electrons and holes

and can be approximated by the following empirical formula

$$M_{2i}(V_2) = \left[1 - \left(\frac{V_{2i}}{V_{BD,2i}} \right)^c \right]^{-1}$$

$$(3.2-6)$$

where $V_{BD,2i}$ is the breakdown voltage of the $2i$-th PN junction and c is

an empirical constant. $J_{G,2i}$ is the current density generated in the
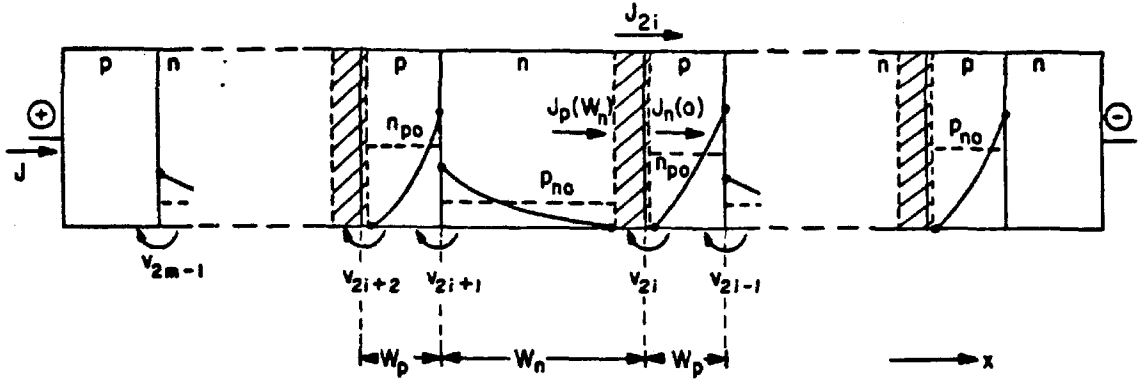
Figure 3.2- 6. Minority carrier distribution across a $(PN)_m$ device in the forward blocking ('OFF') state.

depletion region of the $2i$-th junction (e.g. thermal or light generation) which can – to the first order – be approximated as a constant. $J_{p,2i+1}(W)$ is the hole diffusion current density entering the junction from the left and is given by

$$J_{p,2i+1}(W) = J_{sp,2i+1}\left[(e^{\Lambda V_{2i+1}}- 1) + \cosh\left(\frac{W_{n,2i+1}}{L_{p,2i+1}}\right)\right] \qquad (3.2-7)$$

where $\Lambda = \dfrac{q}{KT}$ and V_i is the voltage across the i-th junction.

$$J_{sp, 2i+1} = \frac{q D_{p, 2i+1} \, p_{no, 2i+1}}{L_{p, 2i+1} \, \sinh\left(\dfrac{W_{n, 2i+1}}{L_{p, 2i+1}}\right)} \tag{3.2-8}$$

and $J_{n, 2i}(0)$, the electron diffusion current density entering the junction from the right, is given by

$$J_{n, 2i}(0) = J_{sn, 2i}\left[(e^{\Lambda V_{2i-1}} - 1) + \cosh\left(\frac{W_{p, 2i}}{L_{n, 2i}}\right) \right] \tag{3.2-9}$$

where

$$J_{sn, 2i} = \frac{q D_{n, 2i} \, n_{po, 2i}}{L_{n, 2i} \, \sinh\left(\dfrac{W_{p, 2i}}{L_{n, 2i}}\right)} \tag{3.2-10}$$

n_{po}, W_p, D_n, L_n and p_{no}, W_n, D_p, L_p are the equilibrium concentration of the minority carriers, the width, the diffusion coefficient and the diffusion length of the minority carriers in the appropriate P and N regions, respectively.

The odd numbered junctions are slightly forward biased, so we have to include the effect of the depletion region recombination currents. These currents can be approximated by the following formula

$$J_R = J_{RO} \, e^{\frac{\Lambda V}{N_E}} \tag{3.2-11}$$

where J_{RO} and N_E are empirical constants (see Section 2.2). In the following calculations we will assume that $N_E = 2$, which is a good

approximation for practical devices.

Since the current is the same throughout the device, we can equate the current densities through the even and odd numbered junctions, so the current density is given by

$$J = J_{2i+1} = J_{p, 2i+1}(0) + J_{n, 2i+2}(W) + J_{R, 2i+1}$$

$$= J_{sp, 2i+1}[(e^{\Lambda V_{2i+1}} - 1)\cosh(\frac{W_{n, 2i+1}}{L_{p, 2i+1}}) + 1] \qquad (3.2-12)$$

$$+ J_{sn, 2i+2}[(e^{\Lambda V_{2i+1}} - 1)\cosh(\frac{W_{p, 2i+2}}{L_{n, 2i+2}}) + 1]$$

$$+ J_{RO, 2i+1}e^{\frac{\Lambda V_{2i+1}}{2}}$$

or

$$J = J_{s, 2i+1}^{*}(e^{\Lambda V_{2i+1}} - 1) + J_{s, 2i+1} + J_{RO, 2i+1}e^{\frac{\Lambda V_{2i+1}}{2}}, \qquad i = 0, 1, 2, \ldots, (m-1)$$

$$(3.2-13)$$

where $J_{p, 2i+1}(0)$ is the hole diffusion current density entering the junction from the right, $J_{n, 2i+2}(W)$ is the electron diffusion current density entering the junction from the left, J_{sp} and J_{sn} are as defined before in Equations (3.2−8) and (3.2−10),

$$J_{s,2i+1} \triangleq J_{sp,2i+1} + J_{sn,2i+2} \qquad (3.2-14)$$

$$J_{s,2i+1}^* \triangleq J_{sp,2i+1} \cosh\left(\frac{W_{n,2i+1}}{L_{p,2i+1}}\right) + J_{sn,2i+2} \cosh\left(\frac{W_{p,2i+2}}{L_{n,2i+2}}\right) \qquad (3.2-15)$$

and $J_{RO,2i+1}$ is the recombination current constant of the $(2i+1)$-th junction.

Note that for $i=0$, $J_p(0) = 0$, and for $i=m-1$, $J_n(W_p) = 0$, since we can assume that the diffusion currents in the two extreme layers are negligble, e.g., these layers are $AlGaAs$ layers with high Al contents, and thus their values of n_{po} and p_{no} are much lower than those of $GaAs$, because of the differences in the bandgap energies.

Using Equations (3.2-5) to (3.2-13), we can obtain a closed form expression for the $J-V$ curve of the device in the following way. For a given value of J, Equation (3.2-13) is a quadratic in $e^{\frac{\Lambda V_i}{2}}$, $i = 1, 3, 5, \ldots, (m-1)$. Once a solution is obtained for all the odd numbered junctions, Equation (3.2-6) can be solved for V_i $i=2, 4, \ldots, (m-2)$, using Equations (3.2-5) and (3.2-7) to (3.2-10). The sum of all the junction voltages thus obtained is the total voltage V across the device, corresponding to the assumed value of J. The particular form of the resulting expressions is quite complicated, but the calculations are straightforward, as described above. The important parameter of the $J-V$ curve in the "OFF" state is the breakover voltage (V_{BO}), which is defined in the same way as for the Shockley diode. At this

point $\frac{dV}{dJ} = 0$. As the current is further increased, the voltage across the

device decreases. This is a negative resistance $[\frac{dV}{dJ} < 0]$ region and thus

unstable, leading to the "ON" state. In this new situation the assumption

about the junction voltages are no longer valid, and new calculations

have to be done.

The breakover voltage of the $(PN)_m$ device is the same as the vol-

tage across $(m-1)$ Shockley diodes operating in series. This is because

the structure consists of distinct sections, ·each isolated between two

reverse biased junctions at which the carriers concentration is virtually

zero. (See Figure 3.2-6). Thus we see that by increasing m we can

obtain devices with higher breakover voltages.

3.2.3 Solution of the Diffusion Equation in the Forward Conducting ('ON') State

In the forward conducting state all the junctions are forward

biased, $|V_i| >> \frac{KT}{q}$, $i=1, 2, \ldots, (2m-1)$, i.e., all the transistors that

model the device are in saturation. This is similar to the behavior of the

common Shockley diode in the 'ON" state. The distribution of the minor-

ity carriers concentration in this state is shown in Figure 3.2-7. (Note

the change of sign in the notation for the even-numbered junction vol-

tages; now all the junctions are forward biased). The resulting diffusion

equations of the entire structure can be written in the form:

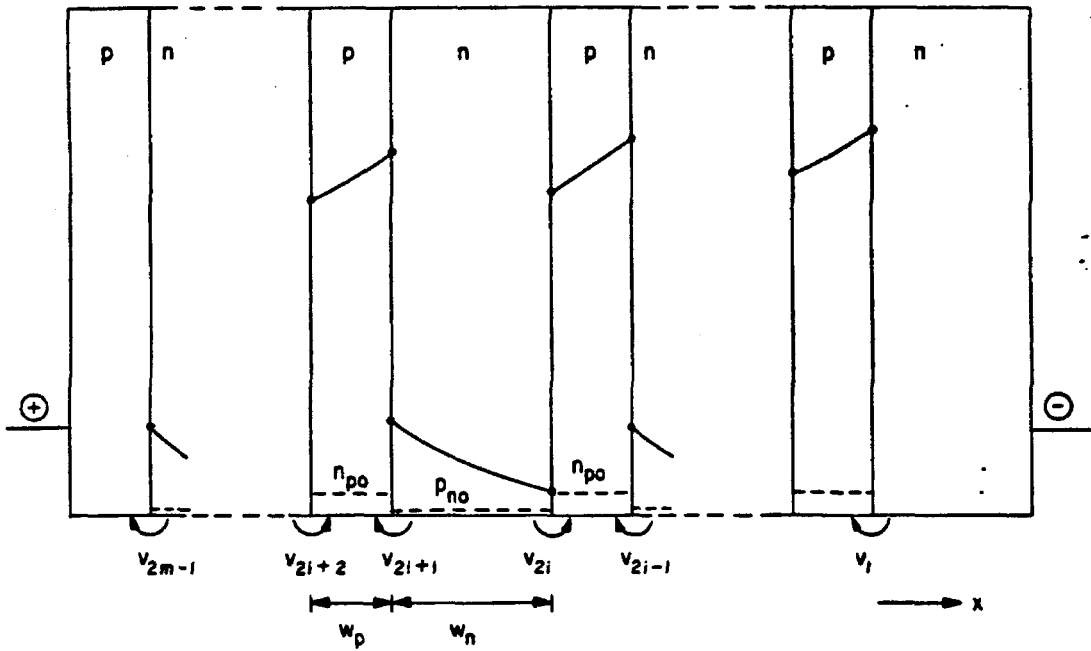$$B\overline{u} + C\overline{w} = \overline{J} \tag{3.2-16}$$

Figure 3.2 7. Minority carriers distribution across a $(PN)_m$ device in the forward conducting ('ON') state.

where

$$\overline{u} = \begin{vmatrix} e^{\Lambda V_1} - 1 \\ e^{\Lambda V_2} - 1 \\ \cdot \\ \cdot \\ e^{\Lambda V_{2m-1}} - 1 \end{vmatrix}$$

(3.2–17)

$$\overline{\mathbf{w}} = \begin{vmatrix} e^{\frac{\Lambda V_1}{2}} - 1 \\ e^{\frac{\Lambda V_2}{2}} - 1 \\ \cdot \\ \cdot \\ e^{\frac{\Lambda V_{2m-1}}{2}} - 1 \end{vmatrix} \qquad (3.2\text{--}18)$$

$$\overline{\mathbf{J}} = \begin{vmatrix} 1 \\ -1 \\ \cdot \\ \cdot \\ 1 \end{vmatrix} \qquad (3.2\text{--}19)$$

The matrix **B**, given by

$$(3.2\text{--}20)$$

$$\mathbf{B} = \begin{vmatrix} J_{sn1}^{\bullet} & -J_{sn2} & 0 & \cdot & & 0 \\ -J_{sn1} & J_{s2}^{\bullet} & -J_{sp3} & 0 & \cdot & \\ 0 & -J_{sp2} & J_{s3}^{\bullet} & -J_{sn4} & \cdot & \\ \cdot & & & \cdot & \cdot & \\ 0 & \cdot & & & -J_{sp,2m-2} & J_{sp,2m-1}^{\bullet} \end{vmatrix}$$

contains the diffusion contribution to the total current and

$$(3.2\text{--}21)$$

$$\mathbf{C} = \begin{vmatrix} J_{RO1} & 0 & \cdot & & 0 \\ 0 & J_{RO2} & 0 & \cdot & \\ \cdot & 0 & J_{RO3} & 0 & \cdot \\ & & & \cdot & \\ 0 & \cdot & & & J_{RO,2m-1} \end{vmatrix}$$

contains the depletion-region recombination contribution to the total current. $J_{sp,i}$, $J_{sn,i}$, $J_{s,i}^{\bullet}$ and J_{ROi} are given in Equations (3.2-8),(3.2-10),(3.2-15) and (3.2-11), respectively. Also $J_{sp,i}^{\bullet} = J_{sp,i}\cosh\left(\dfrac{W_{n,i}}{L_{p,i}}\right)$ and

$J_{sn,i}^{*} = J_{sn,i} \cosh\left(\dfrac{W_{p,i}}{L_{n,i}}\right)$. The derivation of Equations (3.2–16) to (3.2–21)

is outlined in Appendix A. Several calculated results for the devices

described Tables 3.2–1 and 3.2–2 are shown in Figure 3.2–8 and in Fig–

ure 3.2–9.

TABLE 3.2-1. Details of a $(PN)_7$ structure.

Layer Number	Type	Al Contents (x)	Doping Concentration $\times 10^{16}\ [cm^{-3}]$	Width $[\mu m]$
1	n	0.4	0.1	1.5
2	p	0.0	3	0.2
3	n	0.1	0.1	0.8
4	p	0.0	3	0.2
5	n	0.1	0.1	0.8
6	p	0.0	3	0.2
7	n	0.1	0.1	0.8
8	p	0.0	3	0.2
9	n	0.1	0.1	0.8
10	p	0.0	3	0.2
11	n	0.1	0.1	0.8
12	p	0.0	3	0.2
13	n	0.1	0.1	0.8
14	p	0.4	1	1.5
15	p^{+}	0.0	≈ 10	1.0

Part a of these figures shows the distribution of the excess minority car–

riers across the devices. The distribution across the $(PN)_5$ device is

much more balanced than in the $(PN)_7$ device. This fact is also clearly

demonstrated in part b of the figures, which shows the distribution of

TABLE 3.2- 2. Details of $(PN)_5$ structure.

Layer Number	Type	Al Contents (x)	Doping Concentration $\times 10^{18} \, [cm^{-3}]$	Width $[\mu m]$
1	n	0.4	0.1	1.5
2	p	0.0	3	0.25
3	n	0.1	0.1	0.5
4	p	0.1	0.1	0.5
5	n	0.0	3	0.25
6	p	0.1	0.1	1.0
7	n	0.0	3	0.25
8	p	0.1	0.1	1.0
9	n	0.0	3	0.25
10	p	0.4	1	1.5
11	p^+	0.0	≈ 10	1.0

the recombination current across the device. As will be discussed in Section 3.4, it is desirable to have as uniform distribution in the $GaAs$ regions as possible. When designing a structure for a particular carrier profile, the parameters at our disposal are the number of the layers,their types and widths and the doping concentration. All these parameters appear in the solution of the diffusion equation, and thus can affect the performance of the device.

The holding current of the device (i.e., the minimum forward current which is required to sustain the "ON" state) can be estimated in the following way. We know that if the current is reduced below the holding value, the device exhibits negative resistance and is unstable. This
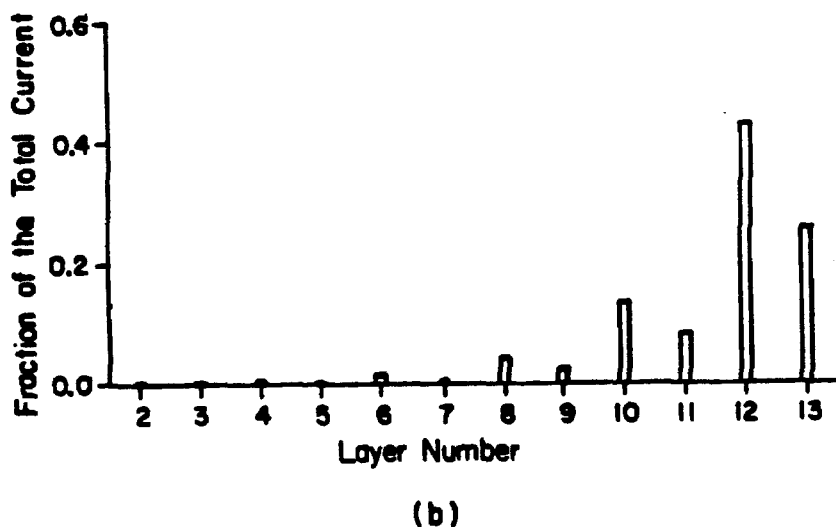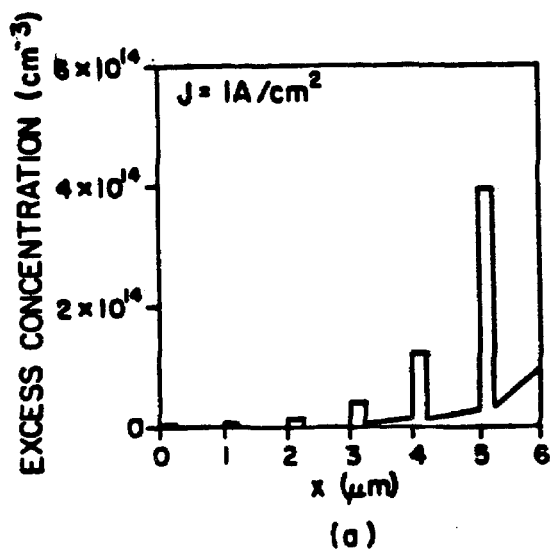
(a)

(b)

Figure 3.2- 8. 'ON' state characteristics of the $(PN)_7$ device described in Table 3.2- 1. a) Excess minority carriers. b) Recombination current distribution in the various regions.

leads to the "OFF" state described in the preceding section, so the value of J for which $\frac{dV}{dJ} = 0$ is the holding current density (J_H). This parameter can be found by solving Equation (3.2–16) numerically. Calculated dependence of J_H on several parameters is shown in Figure 3.2–10. The device consists of $(m-1)$ PN sections of $GaAs$ sandwiched
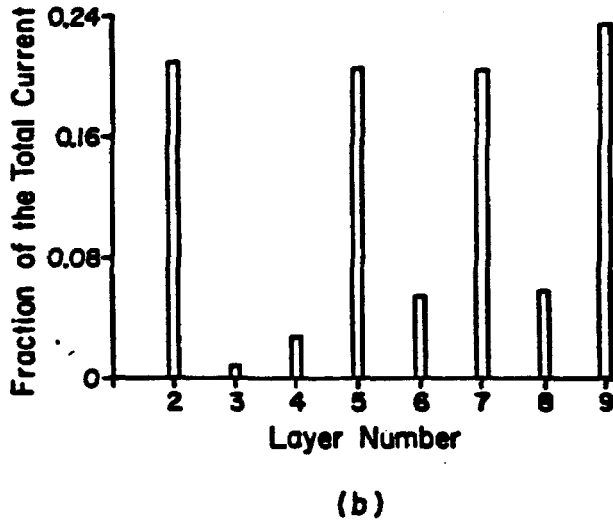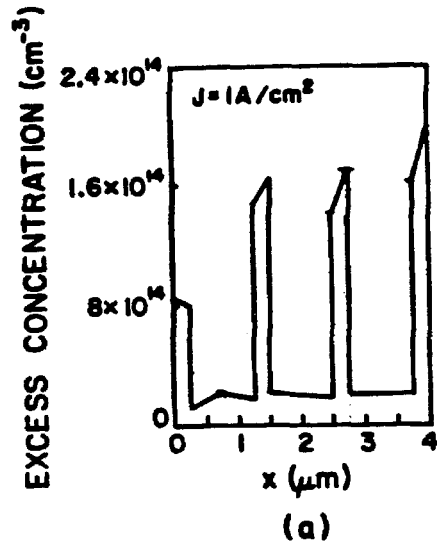
Figure 3.2- 9. 'ON' state characteristics of the $(PN)_5$ device described in Table 3.2- 2. a) Excess minority carriers. b) Recombination current distribution in the various regions.

between two layers of high Al contents $AlGaAs$. As expected, the holding current density increases with increasing the number of the PN sections of the device, with increasing the widths of the layers and with increasing the doping levels. The basic cause for this increase is the need to replenish recombined carriers in more and more regions while still maintaining

all the layers in saturation. Because of the basic exponential dependence between the current and the voltage in *PN* devices, the increase in the holding current with increasing the number of sections in the device is larger than the corresponding increase in the breakover voltages.
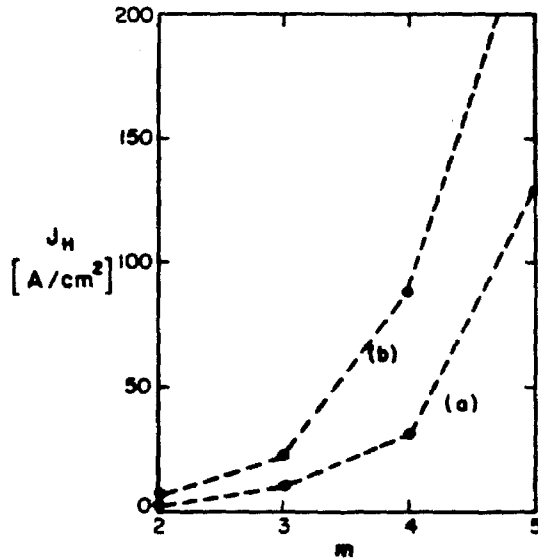

Figure 3.2-10. Calculated dependence of the holding current density (J_H) on the number of layers in the device. a) $W_n=W_p=0.5\mu m$. b) $W_n=W_p=1\mu m$.

It should be noted that the above analysis can be easily extended to any arbitrary structure, not necessarily one which consists of alternating *P* and *N* regions (e.g., *PPNN* $\cdots$).

3.3 Optical Properties of Multi- PN Heterostructure Devices

When multi-PN heterostructures are fabricated from the ternary *AlGaAs* system, it can result in a new type of large optical cavity (LOC) injection lasers. A conventional LOC structure [7] consists of one active region. A large optical cavity structure which is made in a multi-PN structure, contains more than one active region. An example is shown in Figure 3.3-1. In this mode of operation, layers of *GaAs*, which serve as the active regions of the coupled lasers, are surrounded by *AlGaAs* regions of lower refractive index, which together constitute the large optical cavity. Splitting the active region volume into several separated layers may give more degrees of freedom in designing the optical and electrical properties of the device.

The optical properties of such structures can be analyzed using the theory of periodic waveguides [8] or a similar theory of general multilayer waveguides. The whole device is basically one waveguide structure. In particular, it is found that if we have q active regions, every fundamental mode of the single waveguide structure splits into q submodes. Out of these, the submode that has the maximum overlap with the gain profile of the structure will lase.

Since the individual waveguides (i.e., the active regions) are close to each other, and the refractive index differences between them and the *AlGaAs* layers between them are not large, perturbation methods are inadequate for the solution of the problem. Solving for the waveguide modes by the method of Yeh et al [8] involves the solution of a compli-
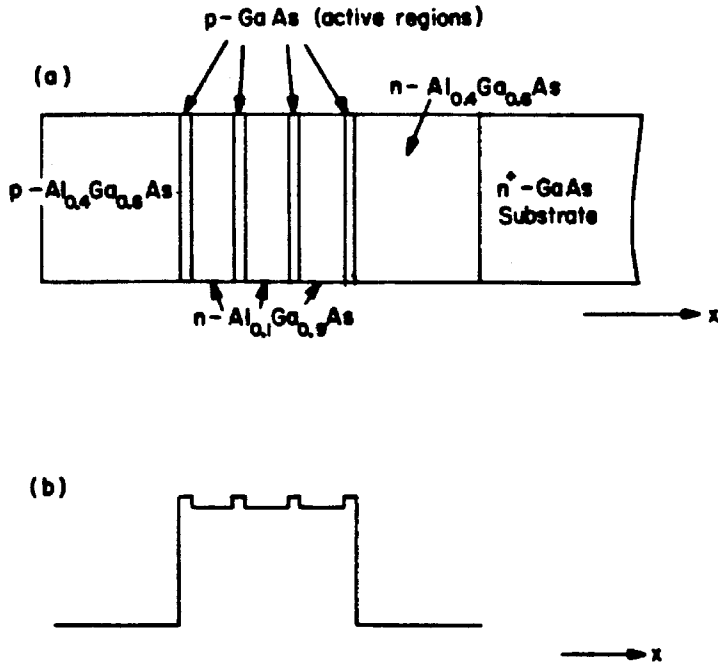
Figure 3.3- 1. Example of implementation of a large optical cavity device with a $(PN)_m$ structure. a) Device structure. b) Refraction index distribution across the device.

cated nonlinear characteristic eigenvalue equation. There are problems (in terms of the computational effort required) in solving this equation, particularly when the eigenvalues are complex. This is the case, for example, when the gain in the active regions is taken into account. An alternative method of numerical solution, based on the Finite Element Method [9], is used in this work. The general computing method, described in Appendix B of this chapter, is capable of solving also two dimensional waveguides. It was used here for solving one dimensional structures.

In designing multi-PN structures for use as LOC injection lasers, one must take into account the need to establish nearly equal gain in all the active regions. As a first approximation this is obtained by making the recombination currents in all the active regions as equal to each other as possible. Another consideration is to minimize the recombination currents in the *AlGaAs* layers, since they do not contribute to the optical gain of the laser. An example of such a design is shown in Figure 3.2–9b.

Figure 3.3–2 shows the calculated optical mode of the $(PN)_5$ device whose parameters are described in Table 3.2–2. The index of refraction (N) is the sum of its real part (N_r), shown in Figure 3.3–2a and its imaginary part (N_i), shown in Figure 3.3–2b. (i.e., $N = N_r + iN_i$). N_i is related to the optical gain (g) by $N_i = \dfrac{\lambda}{4\pi} g$. In this particular structure N_i corresponds to a gain of about $40 cm^{-1}$, but the mode is determined virtually only by the variations of N_r across the device. In Figure 3.3–2c and 3.3–2d the near–field and far–field intensity patterns, respectively, are shown.
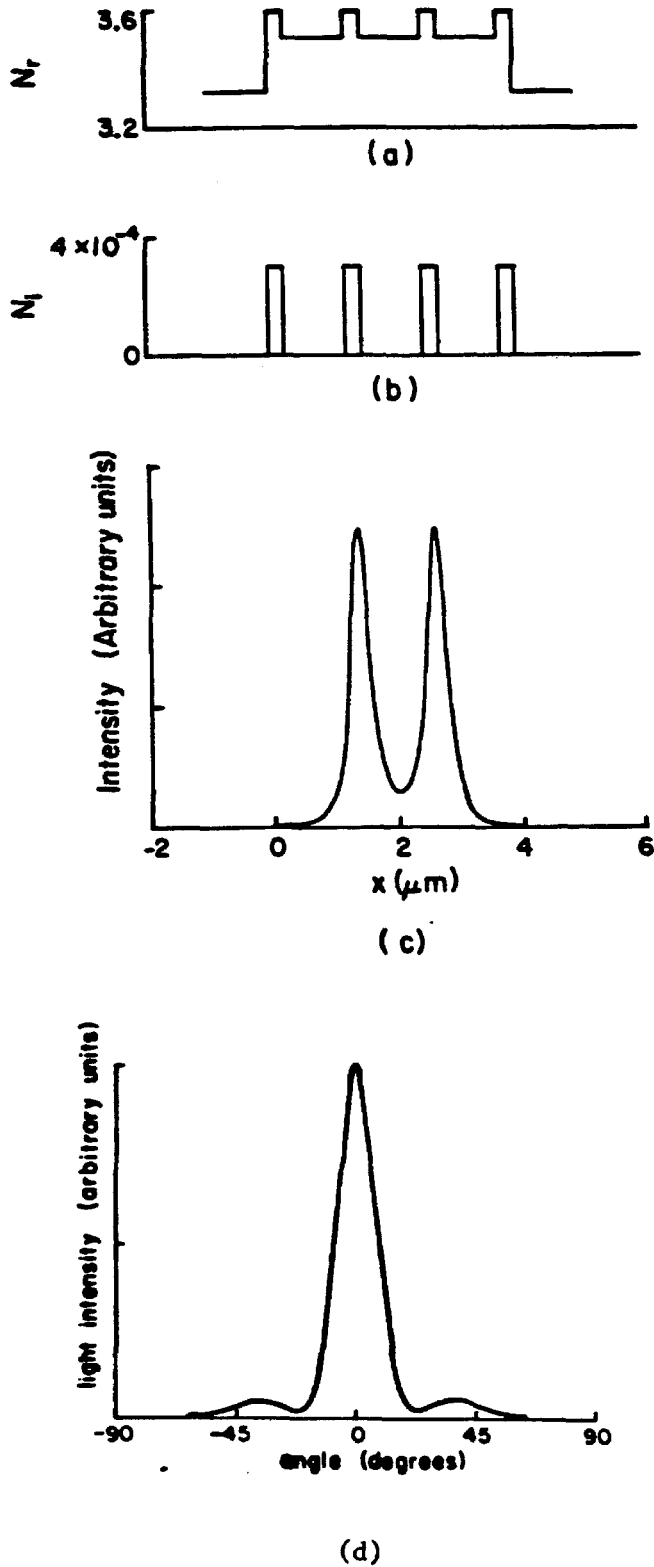
Figure 3.3-2. Calculated optical properties of the $(PN)_5$ laser. a)real part of the index of refraction. b)imaginary part of the index of refraction. c)near field pattern. d)far field pattern.

3.4 Experimental Results

3.4.1 Fabrication Procedure

Some of the processing steps are common to the fabrication of the multi-PN heterostructures and the Translaser. Missing details on these steps can be found in the subsection describing the fabrication procedure of the Translaser. (Section 2.2-4).

The layered structure is grown by liquid phase epitaxy at $800°C$. Parameters of two typical device structures (e.g., layers types, widths, doping) are described in Tables 3.2-1 and 3.2-2. Since the number of the solution chambers in the graphite boat is smaller than the required number of layers in the structure, the periodic parts of the structure are grown by moving the slide-bar of the boat in both directions between the solutions. In that case, two "dummy" wafers are used, one on each side of the actual growth wafer. The function of these "dummy" wafers is to reduce the supersaturation of each solution before it comes in contact with the actual wafer [10]. The dopants used are Ge (p-type), Sn (n-type, for regions with $N_D \lesssim 1 \times 10^{18} cm^{-3}$) and Te (n-type, for regions with $N_D \gtrsim 1 \times 10^{18} cm^{-3}$).

Devices that are tested only for electrical parameters are etched down to a $100 \times 100 \mu m^2$ mesas, while devices which operate also as injection lasers are etched down to a $100 \mu m$ mesa in one direction and cleaved to $\approx 300 \mu m$ length in the perpendicular direction.

3.4.2 Electrical Properties

The multi–*PN* structure is an alternative way of manufacturing switching devices. The inherently greater gains involved in such a device should yield in principle higher breakover voltages and higher holding currents. This is due to the modification in the switching condition as compared to a simple SCR. Several types of devices have been fabricated in order to find the electrical characteristics of multi–*PN* structures.

A device of the first type is shown in Figure 3.4–1 This is a $(PN)_7$ device. The dependence of the $I-V$ curve of the structure on the *Al* contents (x) in the layers between the *GaAs* regions was investigated. Curves of devices with $x=0.1$, 0.2, and 0.4 are shown in Figure 3.4–2. When the *Al* contents is too high, the current gain of the *PNP* transistors in the device model (these are the transistors which have the n –*AlGaAs* layers as their base regions) becomes too small to maintain the device in the "ON" state. For $x=0.4$ even reduction in the number of layers, e.g., $(PN)_4$ is not enough. In this case the obtained $I-V$ curve is that of a transistor in avalanche. The calculated carriers distribution in the device is shown in Figure 3.2–8a for $x=0.1$. As we see, the carrier concentration is the highest in the upper *GaAs* region, with fewer and fewer carriers in the subsequent regions. This result was verified in the following way. Instead of etching the devices into the $100 \times 100 \mu m^2$ mesas, they were etched only in one direction and cleaved in the other dimension (with lengths about $300 \mu m$), thus forming injection lasers. Observing the near field radiation pattern of the laser, it was found that at, or slightly above the threshold $(J_{th} \approx 5.5 kA -cm^{-2})$ only the upper
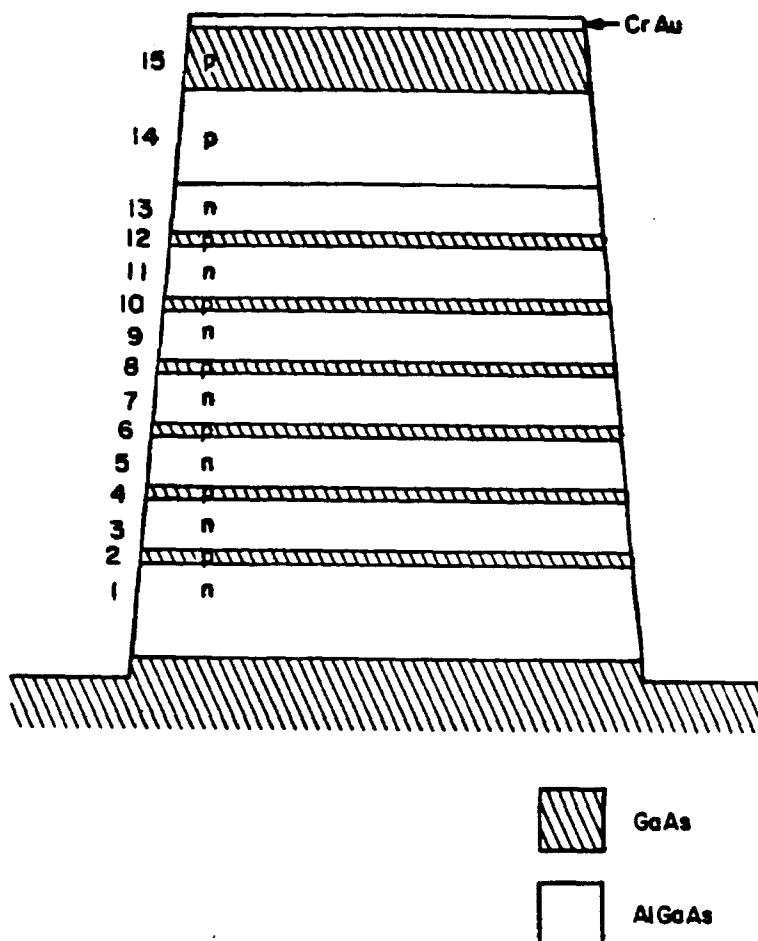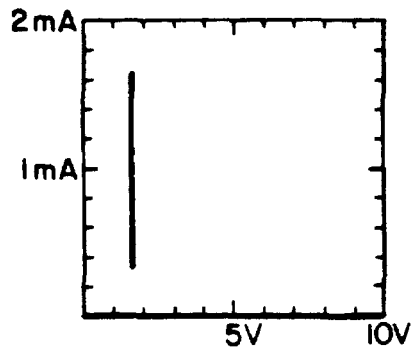
Figure 3.4- 1. Example of a fabricated $(PN)_7$ device. Typical parameters are shown in Table 3.2 -1.

active region is lasing, while all the other active regions emitted only spontaneous emission. Only when the current was raised to about $1.4 \times I_{th}$ did the next active region lase.

Devices of a second type were grown with the goal of equalizing the
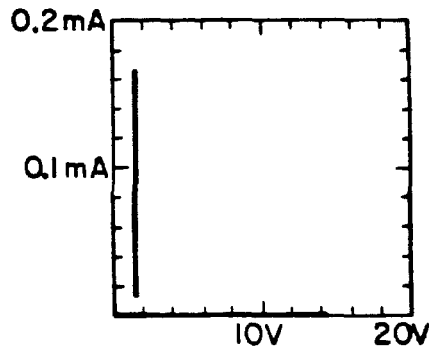
Figure 3.4- 2. Dependence of the $I-V$ curve of $(PN)_7$ devices on the Al contents (x) in the waveguide layers. a) $x = 0.1$. b) $x = 0.2$. c) $x = 0.4$ (No bistability).

carrier distribution in all the *GaAs* layers of the device. The $(PN)_5$ structure is shown in Figure 3.4-3, and the $I-V$ curve is shown in Figure 3.4-4.
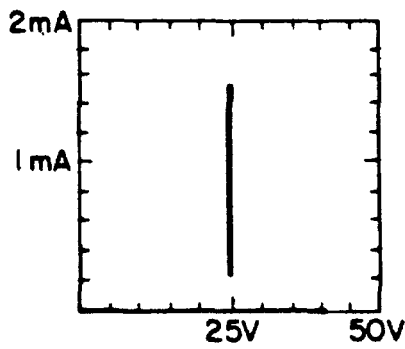

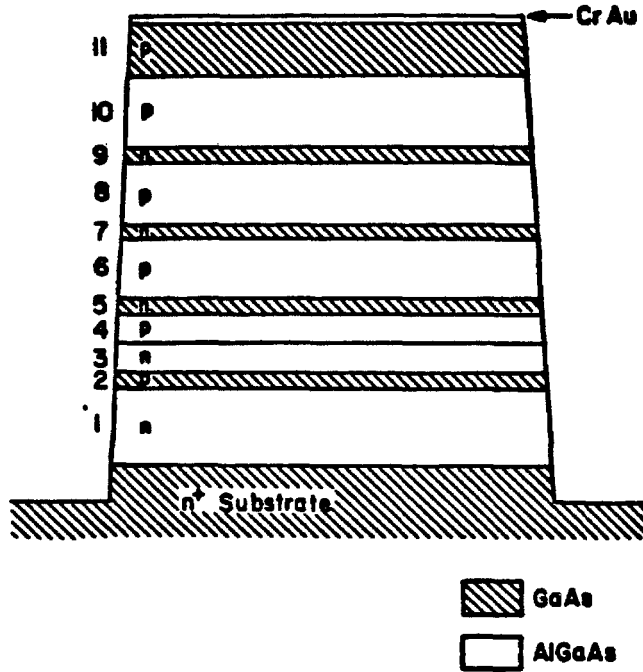**Figure 3.4- 3.** Example of a fabricated $(PN)_5$ device. Typical parameters are shown in Table 3.2- 2.

From Figure 3.2-8b it is seen that most of the carriers ($\approx 82\%$) recombine in the active regions, and the the level of recombination currents in the different active regions is uniform to within 10%. The breakover voltage (V_{BO}) of the device is $\approx 9V$. Devices with breakover voltages of more
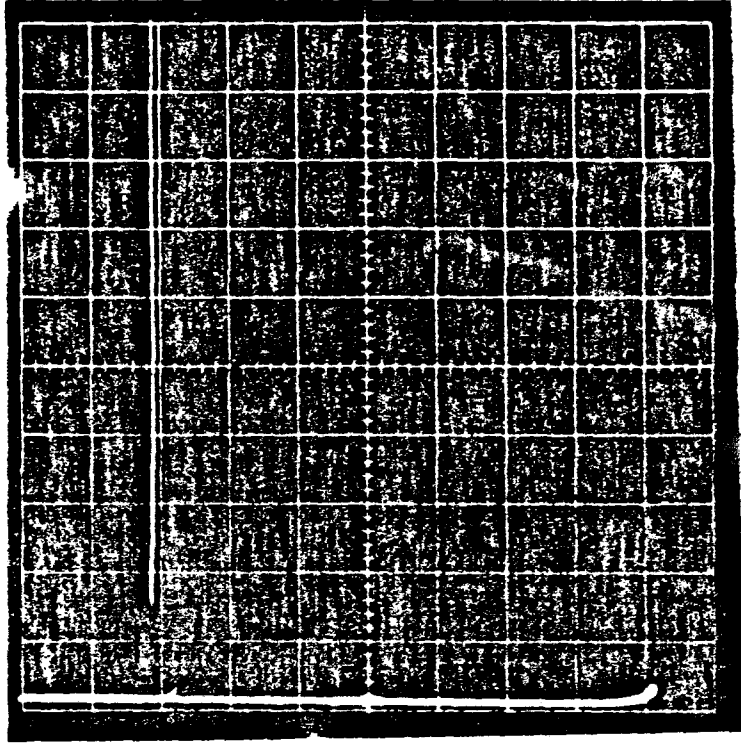
Figure 3.4- 4. $I-V$ curve of a $(PN)_5$ device. (horizontal scale: 1 V/div; vertical scale: 0.1 mA/div).

than $35V$ were also observed. The value of V_{BO} in each particular device also depends on the amount of leaking due to imperfections. The hold– ing current density (J_H) is about $1.5 A cm^{-2}$.

3.4.3 Optical Properties

Lasers were made also from the $(PN)_5$ devices described in Figure 3.4-3. The threshold current density is about $13 kA cm^{-2}$, comparable to conventional large optical cavity lasers of the same dimensions. The

light versus current curve of a typical laser is shown in Figure 3.4−5.
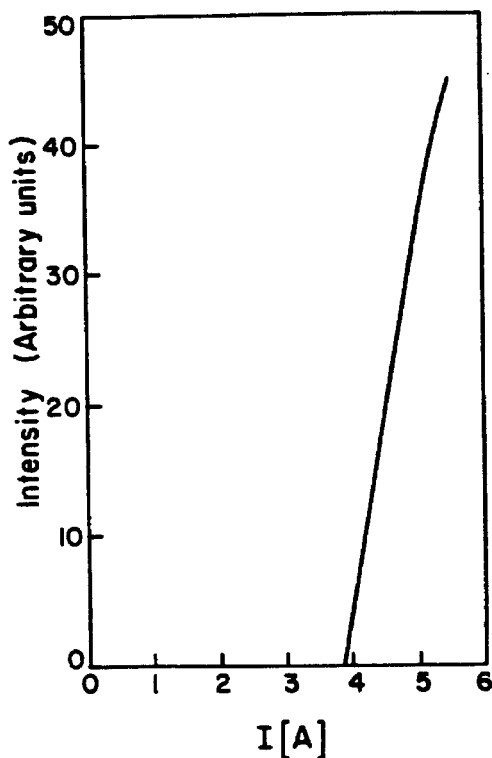
Figure 3.4- 5. Light versus current curve of a $(PN)_5$ laser. (the area of the device is $\approx 300 \times 100 \mu m^2$)

The differential quantum efficiency is about 40% for both facets. At threshold the near field showed the pattern expected from the calculation of the carrier concentration. Figure 3.4−6 shows a photomicrograph of the near field pattern of the laser. Figure 3.4−7 shows the
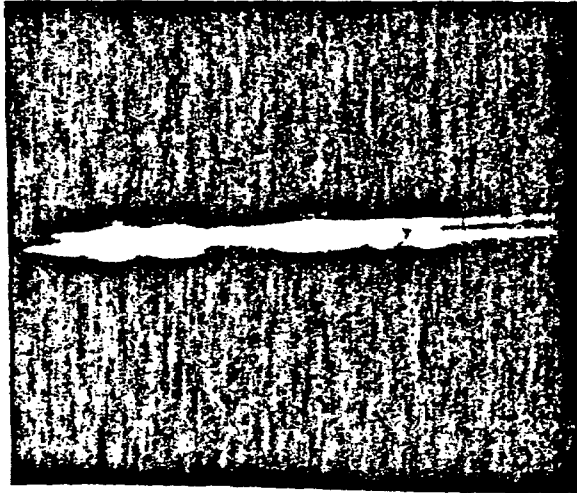
Figure 3.4- 6. Photomicrograph of a near field pattern of a $(PN)_5$ device.

measured near field intensity pattern of the laser in the direction per-
pendicular to the junction plane. The inability to fully resolve the two
extreme weak side lobes of the mode is due to the nonuniform and
filamentary lasing in the direction of the junction plane. It is expected
that reducing the transverse width of the active region from $100\mu m$ to
$10\mu m$ or less will enable the device to oscillate in a single transverse
mode, in the same way it is done in conventional stripe geometry injec-
tion lasers. In Figure 3.4−8 the far field pattern of the laser in a direc-
tion perpendicular to the junction plane is shown. The fact that the far

Figure 3.4- 7. Near field pattern of a $(PN)_5$ laser.

field pattern is broader than the calculated value is probably due to spontaneous emission. Generally there is a good agreement between calculated and measured results, as can be seen by comparing these results to these of the preceding section.
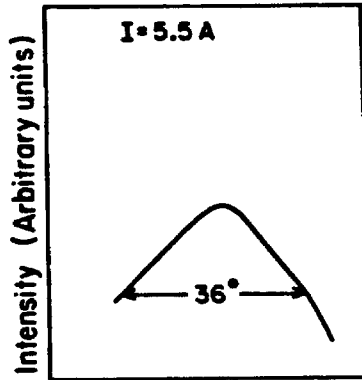
Figure 3.4- 8. Far field pattern of a $(PN)_5$ laser.

Appendix A: Derivation of the device equations in the 'ON' state

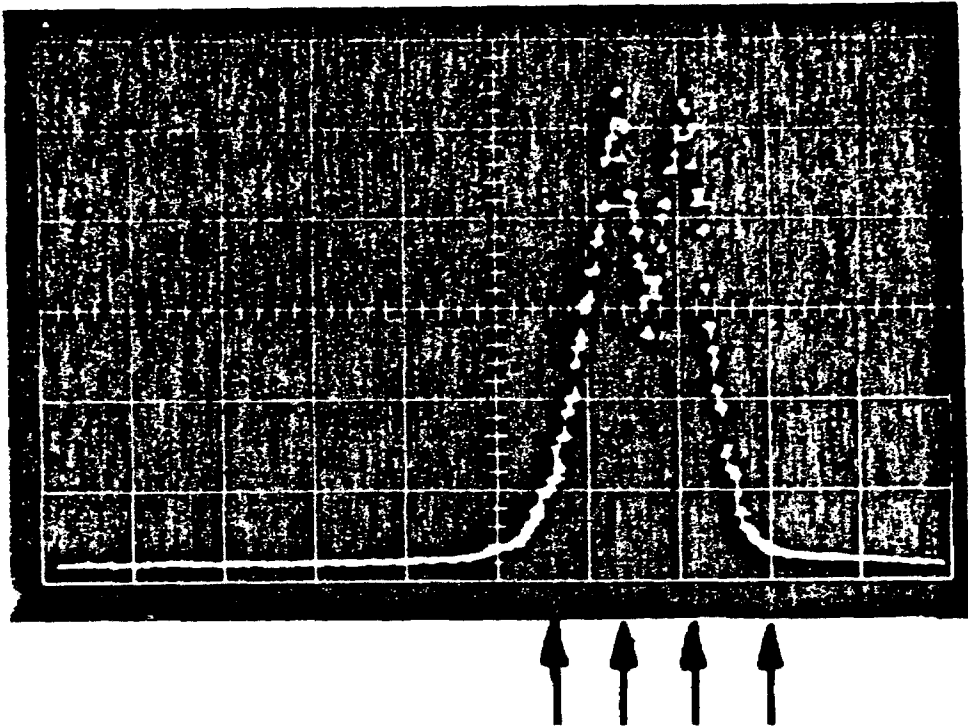In the "ON" state, all the junctions are forward biased. As a result of this condition, all the layers can be analyzed as bases of a transistor in saturation. We will analyze separately the n and p regions, solving the diffusion equation. The effect of the depletion region recombination currents can be accommodated by an added term as in Equation (3.2−11) at every junction.

1. n−type region: The minority carriers distribution is shown in Figure A.1a. The steady−state solution to the diffusion equation in this region subject to the boundry conditions

$$\widehat{p}(0) = p_{no}(e^{\frac{qV(0)}{KT}} - 1) \qquad (A-1)$$

$$\widehat{p}(W_n) = p_{no}(e^{\frac{qV(W_n)}{KT}} - 1) \qquad (A-2)$$

is

$$\widehat{p}(x) = \widehat{p}(0)\frac{\sinh(\frac{W_n-x}{L_p})}{\sinh(\frac{W_n}{L_p})} + \widehat{p}(W_n)\frac{\sinh(\frac{x}{L_p})}{\sinh(\frac{W_n}{L_p})} \qquad (A-3)$$

where $\widehat{p}$ denotes carrier concentration in excess of the equilibrium concentration, p_{no} is the equilibrium minority carrier concentration in this region, and $V(0)$ and $V(W_n)$ are the junction voltages at the two ends of this region. Note that both $\widehat{p}(0)$ and $\widehat{p}(W_n)$ are much

larger than p_{no}. The hole diffusion currents at the two ends of the n-type region are

$$J_p(0) = -qD_p \frac{d\hat{p}(x=0)}{dx} = J_{sp}\left[(e^{\frac{qV(0)}{KT}} - 1)\cosh(\frac{W_n}{L_p}) - (e^{\frac{qV(W_n)}{KT}} - 1)\right]$$

$$(A-4)$$

$$J_p(W_n) = -qD_p \frac{d\hat{p}(x=W_n)}{dx} = J_{sp}\left[(e^{\frac{qV(0)}{KT}} - 1) - (e^{\frac{qV(W_n)}{KT}} - 1)\cosh(\frac{W_n}{L_p})\right]$$

$$(A-5)$$

where J_{sp} is given by Equation (3.2−8).

2. p-type region:

The minority carriers distribution is shown in Figure 3.2−15b. Repeating the same analysis, but replacing the holes with electrons, we obtain

$$J_n(0) = J_{sn}\left[(e^{\frac{qV(W_p)}{KT}} - 1) - (e^{\frac{qV(0)}{KT}} - 1)\cosh(\frac{W_p}{L_n})\right] \qquad (A-6)$$

$$J_n(W_p) = J_{sn}\left[(e^{\frac{qV(W_p)}{KT}} - 1)\cosh(\frac{W_p}{L_n}) - (e^{\frac{qV(0)}{KT}} - 1)\right] \qquad (A-7)$$

where J_{sn} is given by Equation (3.2−10).
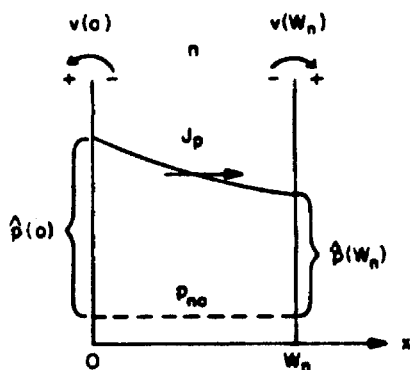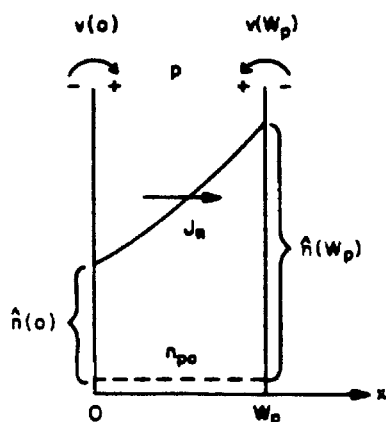
Figure A- 1. Parameters of a) n- type region, and region in saturation. b) p-type

At each junction the sum of the two diffusion currents entering the junction from both sides, plus the recombination current in the depletion region of the junction itself equal the total current density J through the device. Thus for a PN junction (i.e., the odd-numbered junctions) we can write

$$J = J_n(W_p) + J_p(0) + J_R \qquad (A-8)$$

and for an *NP* junction (i.e., the even–numbered junctions) we can write

$$J = J_p(W_n) + J_n(0) + J_R \tag{A-9}$$

where the current components in Equations (A–8) and (A–9) are given by Equations (A–4) to (A–7) and (3.2–11). Of course, the particular indexing of the voltages depends upon the location of the specific junctions in the device. Also note that at the two extreme junctions the only diffusion current is due to minority carriers in the inner layers, as explained in the text. When Equations (A–4) to (A–9) and (3.2–11) are grouped together with appropriate indexing, the result is given by Equations (3.2–16) to (3.2–21).

Appendix B: Numerical Solution of Two Dimensional Waveguides Using the Finite Element Method

In this Appendix a method for solving two dimensional waveguides is described. We start from the general wave equation for the electric field $\vec{E}$

$$\nabla^2 \vec{E} - \mu\varepsilon_0\varepsilon\frac{\partial^2 \vec{E}}{\partial t^2} = -\nabla(\vec{E}\cdot\nabla\ln\varepsilon) - (\nabla\ln\mu)\times(\vec{\nabla}\times\vec{E}) \qquad (B-1)$$

This equation is derived directly from Maxwell's equations without any simplifying assumptions. Under the assumptions of non−magnetic media (i.e., $\mu=\mu_0$), two dimensional structures [i.e., $\varepsilon=\varepsilon(x,y)$], and harmonic time dependence, the field solutions are of the form

$$\vec{E}(x,y,z,t) = \vec{E}(x,y)e^{i(\omega t - \beta z)} \qquad (B-2)$$

in which case Equation (B−1) is reduced to

$$\frac{\partial^2 \vec{E}}{\partial x^2} + \frac{\partial^2 \vec{E}}{\partial y^2} - (\beta^2 - \mu\varepsilon_0\varepsilon\omega^2)\vec{E} = -\nabla(\vec{E}\cdot\nabla\ln\varepsilon) \qquad (B-3)$$

Writing Equation (B−3) explicitly results in a set of three differential scalar wave equations for the x, y and z components:

$$\frac{\partial^2 E_z}{\partial x^2} + \frac{\partial^2 E_z}{\partial y^2} + (k^2\varepsilon - \beta^2)E_z + \frac{\partial}{\partial x}\Big[E_z\frac{\partial\ln\varepsilon}{\partial x} + E_y\frac{\partial\ln\varepsilon}{\partial y}\Big] = 0 \quad \text{(B-4a)}$$

$$\frac{\partial^2 E_y}{\partial x^2} + \frac{\partial^2 E_y}{\partial y^2} + (k^2\varepsilon - \beta^2)E_y + \frac{\partial}{\partial y}\Big[E_z\frac{\partial\ln\varepsilon}{\partial x} + E_y\frac{\partial\ln\varepsilon}{\partial y}\Big] = 0 \quad \text{(B-4b)}$$

$$\frac{\partial^2 E_z}{\partial x^2} + \frac{\partial^2 E_z}{\partial y^2} + (k^2\varepsilon - \beta^2)E_z - i\beta\Big[E_z\frac{\partial\ln\varepsilon}{\partial x} + E_y\frac{\partial\ln\varepsilon}{\partial y}\Big] = 0 \quad \text{(B-4c)}$$

where $k \triangleq \omega\sqrt{\mu\varepsilon_0} = \frac{\omega}{c}$.

In calculations done for injection lasers, we are interested in the tangential components of the field, since they eventually carry the radiated power. Thus we will solve Equations (B-4a) and (B-4b) for E_z and E_y. We start by multiplying Equation (B-4) by a function W and integrating it. Next we use Green's Theorem

$$\int_A f\Big(\frac{\partial^2 g}{\partial x^2} + \frac{\partial^2 g}{\partial y^2}\Big)dxdy = \int_C f\nabla g\cdot\hat{n}dl - \int_A \nabla g\cdot\nabla g\,dxdy \quad \text{(B-5)}$$

(C is the contour around the region A) and the rules of partial integration. Since in our case the integration is carried over the whole (xy) plane, and all the functions under consideration are zero at infinity, the line integral in Equation (B-5) drops, leading to the following equation:

$$\int_A\Big(\frac{\partial W}{\partial x}\frac{\partial E_z}{\partial x} + \frac{\partial W}{\partial y}\frac{\partial E_z}{\partial y}\Big)dxdy - \int_A(k^2\varepsilon - \beta^2)WE_z\,dxdy \quad \text{(B-6)}$$

$$+ \int_A\Big[E_z\frac{\partial\ln\varepsilon}{\partial x} + E_y\frac{\partial\ln\varepsilon}{\partial y}\Big]\frac{\partial W}{\partial x}dxdy = 0$$

Similarly we obtain from Equation (B-4b)

$$\int_A \left(\frac{\partial W}{\partial x} \frac{\partial E_y}{\partial x} + \frac{\partial W}{\partial y} \frac{\partial E_y}{\partial y} \right) dx dy - \int_A (k^2 \varepsilon - \beta^2) W E_y dx dy \qquad (B-7)$$

$$+ \int_A \left[E_x \frac{\partial \ln \varepsilon}{\partial x} + E_y \frac{\partial \ln \varepsilon}{\partial y} \right] \frac{\partial W}{\partial y} dx dy = 0$$

In the Finite Element Method, the (xy) plane is divided into poligon-shaped elements, usually triangles or quadrilaterals. In each element the properties of the medium (in this problem– ε) are assumed to be constant. Next we make an approximate expansion of E_x and E_y in terms of a set of base functions $\{\varphi_i\}$:

$$E_x \approx \sum_j C_{2j-1} \varphi_j \qquad (B-8a)$$

$$E_y \approx \sum_j C_{2j} \varphi_j \qquad (B-8b)$$

The functions $\{\varphi_i\}$ are localized: each φ_i has a value of unity at the i-th node, and it is non–zero only over the elements which border this node.

Putting $W = E_x, E_y$ in Equations (B-6) and (B-7), using Equation (B-8), yields the following matrix equation:

$$\begin{vmatrix} A_{ij}^x & D_{ij}^y \\ D_{ij}^x & A_{ij}^y \end{vmatrix} \begin{vmatrix} \hat{E}_x \\ \hat{E}_y \end{vmatrix} + \beta^2 \begin{vmatrix} B_{ij} & 0 \\ 0 & B_{ij} \end{vmatrix} \begin{vmatrix} \hat{E}_x \\ \hat{E}_y \end{vmatrix} = \vec{0} \qquad (B-9)$$

where

$$A_{ij}^x \triangleq \int_A \left(\frac{\partial \varphi_i}{\partial x} \frac{\partial \varphi_j}{\partial x} + \frac{\partial \varphi_i}{\partial y} \frac{\partial \varphi_j}{\partial y} \right) dx dy - \qquad \text{(B-10a)}$$

$$k^2 \int_A \varepsilon \varphi_i \varphi_j dx dy + \int_A \frac{\partial \varphi_i}{\partial x} \varphi_j \frac{\partial \ln \varepsilon}{\partial x} dx dy$$

$$A_{ij}^y \triangleq \int_A \left(\frac{\partial \varphi_i}{\partial x} \frac{\partial \varphi_j}{\partial x} + \frac{\partial \varphi_i}{\partial y} \frac{\partial \varphi_j}{\partial y} \right) dx dy - \qquad \text{(B-10b)}$$

$$k^2 \int_A \varepsilon \varphi_i \varphi_j dx dy + \int_A \frac{\partial \varphi_i}{\partial y} \varphi_j \frac{\partial \ln \varepsilon}{\partial y} dx dy$$

$$D_{ij}^x \triangleq \int_A \frac{\partial \varphi_i}{\partial y} \varphi_j \frac{\partial \ln \varepsilon}{\partial x} dx dy \qquad \text{(B-10c)}$$

$$D_{ij}^y \triangleq \int_A \frac{\partial \varphi_i}{\partial x} \varphi_j \frac{\partial \ln \varepsilon}{\partial y} dx dy \qquad \text{(B-10d)}$$

$$B_{ij} \triangleq \int_A \varphi_i \varphi_j dx dy \qquad \text{(B-10e)}$$

Equation (B-9) is a generalized eigenvalue problem. Since we are usually interested in the lowest order modes, only the highest values of β need to be solved for. The solution can be done efficiently by an iterative method [11]. It should also be noted that since $\{\varphi_i\}$ are localized, the matrices in Equations (B-9) can, after rearrangement, be bounded, a

fact that helps in terms of computer storage space and computing time needed for the solution.

The far–field pattern is found by taking the Fourier Transform of the mode pattern times an obliquity factor [12]. For angles less than 45° relative to the forward direction, the equation for the far–field diffraction from an opening in an infinite conducting screen [13], are accurate enough for our application.

References for Chapter 3

[1] J. L. Moll, M. Tanenbaum, J. M. Goldey, and N. Holonyak, Jr., "p−n−p−n Transistor Switches", Proc. IRE, 44, pp 1174−1182 (1956)

[2] F. E. Gentry, F. W. Gutzwieler, N. Holonyak, Jr., and E. E. Von Zastrow, *Semiconductor Controlled Rectifiers*, Prentice−Hall, Inc. Englewood Cliffs, New−Jersey, 1964

[3] H. F. Lockwood, K.−F. Etzold, T. E. Stockton and D. P. Marinelli, "The GaAs P−N−P−N Laser Diode", IEEE J. Quant. Electron., **QE- 10**, pp 567−569 (1974)

[4] C. P. Lee, A. Gover, S. Margalit, I. Samid and A. Yariv, "Barrier−controlled low−threshold pnpn GaAs heterostructure laser", Appl. Phys. Lett., **30**, pp 535−538 (1977)

[5] W. F. Kosonocky, R. H. Cornely and I. J. Hegyi, "Multilayer GaAs Injection Laser" IEEE J. Quant. Electron., **QE- 4**, pp 176−179 (1968)

[6] J. Katz, N. Bar−Chaim, S. Margalit and A. Yariv, "Large Optical Cavity AlGaAs Lasers with Multiple Active Regions", J. Appl. Phys., **51**, pp 4038−4041 (1980)

[7] H. C. Casey, Jr. and M. B. Panish, *Heterostructure Lasers*, Part B, Academic Press, New−York, 1978, pp 197−207

[8] P. Yeh, A.Yariv and C.−S. Hong, "Electromagnetic Propagation in Periodic Stratified Media. I. General Theory", J. Opt. Soc. Am., **67**, pp 423−438 (1977).

[9] O. C. Zienkiewicz, *The Finite Element Method*, Third Edition, McGraw-Hill, London, 1977

[10] Ref. [7], Part B, pp 123–124.

[11] S. B. Dong and J. A. Wolf, Jr, "On a Direct–Iterative Eigensolution Technique", Int. J. Num. Meth. Eng., 4, pp 155–161 (1972)

[12] H. Kressel and J. K. Butler, *Semiconductor Lasers and Heterojunction Leds*, Academic Press, New York, 1977, Ch. 6

[13] J. D. Jackson, *Classical Electrodynamics*, Second Edition, John Wiley & Sons, New-York, 1975, Ch. 9

4. NOVEL STRUCTURES OF LOW THRESHOLD SINGLE MODE INJECTION LASERS

4.1 Introduction

Of the many parameters characterizing the laser diode, the threshold current is probably the single most important one. This importance stems from two main reasons. First, all the power invested in the laser below its threshold is wasted. This is undesirable in multi-device networks and in other systems where low power consumption is of great importance. Second, all the power wasted below threshold is dissipated in the laser, thus raising its temperature. Since the lifetime of injection laser degrades drastically with increasing temperature [1], lasers with high threshold currents are inherently less reliable.

The second property often required from lasers used in optical communication systems is that they have a stable radiation pattern –i.e., single spatial mode lasers –preferably the fundamental mode.

Two types of lasers having these two desirable properties are described in this chapter. A laser structure fabricated by a novel technique of selective growth, the Embedded Stripe Laser (ESL) [2], is described in Section 4.2. In Section 4.3 we describe a modified version of the Buried Heterostructure (BH) laser [3], which in this case [4] is fabricated on a Semi Insulating (SI) $GaAs$ substrate, thus making it more suitable for integration with other electronic devices, using planar technology.

4.2 The Embedded Stripe Laser

4.2.1 Principles of Selective Growth

In the usual methods of devices fabrication, the epitaxial layers are grown uniformly over all the substrate area, and their different spatial features are subsequently defined by photolithographic steps. A basic alternative approach, used in fabricating the Embedded Stripe Laser, is to use selective growth. In this method we define spatial features on the substrate itself, so the epilayers do not grow uniformly over it. Several methods for fabricating different devices using this approach have been demonstrated [4]–[7]. In particular, Lee, Samid, Gover and Yariv [4]–[5] fabricated lasers by growing through stripe openings defined on the substrate by different techniques. The details of the crystallographic features of the selective growth are described in detail in [6]. The main results are summarized below.

Since the growth is restricted only to certain parts of the substrate, it has three dimensional features. In all the cases described, the growth is in the (100) plane of the substrate. When the stripes are parallel to the cleavage planes of the crystal (i.e., the (011) or the (01$\overline{1}$) planes), the basic form of the resulting growth is shown in Figure 4.2-1. The structure has a trapezoidal cross section. The side walls of the trapezoid structure are the (11$\overline{1}$) and the ($\overline{1}$11) planes, which grow at an angle of 55°44′ with respect to the (100) substrate surface. The selective growth starts on the (100) surfaces, and proceeds to the (111) surfaces, where it continues at a much smaller rate. The case described above is the most

useful one, since the crystal cleavage planes serve as the laser mirrors.
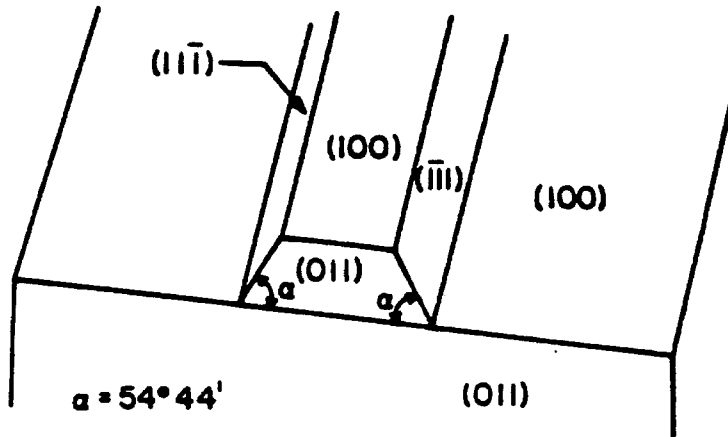
Figure 4.2- 1. Schematic structure of embedded growth

If the stripes are oriented in 45° with respect to the cleavage planes, the side walls of the grown structure are perpendicular to the substrate. This result was used by Bellavance and Campbell [7] to fabricate lasers with grown mirrors.

4.2.2 Description of the Embedded Stripe Laser

It is widely appreciated that a prerequisite for a double hetero – structure(DH) laser with low threshold current and a well behaved optical mode, is the existence of a built-in optical waveguide and carrier confinement in the plane of the active layer as well as at right angles to it, as explained by Saito and Ito [8]. The buried heterostructure (BH)

laser [3] is probably the best known example of such a laser structure. Unlike the BH laser, the Embedded Stripe Laser, described in this chapter, is fabricated by a one step liquid phase epitaxial growth [2]. This growth is performed on a $GaAs$ substrate through openings in Si_3N_4 masks. The main disadvantage of earlier works in selective growth (which were described in the previous section), is that in these cases the substrate area was covered completely by a mask (oxide or nitride), except for the relatively narrow stripes where the laser mesa was grown. Since the area available, in this case, to the excess solute is limited, large and poorly controlled growth rates result, even at slow cooling rates. This leads to devices with large dimensions (stripe widths $\approx 25\ \mu m$) and hence high threshold currents ($> 200\ mA$).

In the growth method employed in the Embedded Stripe Laser, which is illustrated in Figure 4.2-2, the Si_3N_4 mask, which delineates the area of the selective growth, is deposited as two narrow stripes —one on each side of what is later on to become the laser mesa. Large "dummy" areas of the substrate adjacent to the stripe are thus available to receive most of the solute and thus moderate the growth rate. This results in embedded lasers with active regions whose width as well as height can be controlled within the submicron range. The fact that the $GaAs$ active region is completely embedded in $AlGaAs$, provides the necessary optical guiding and electrical confinement, as discussed above.

An example of the small structure dimensions that can be obtained reproducibly under normal growth conditions is shown in Figure 4.2-3. It should be noted that the total height of the mesa is $2\ \mu m$, the width of
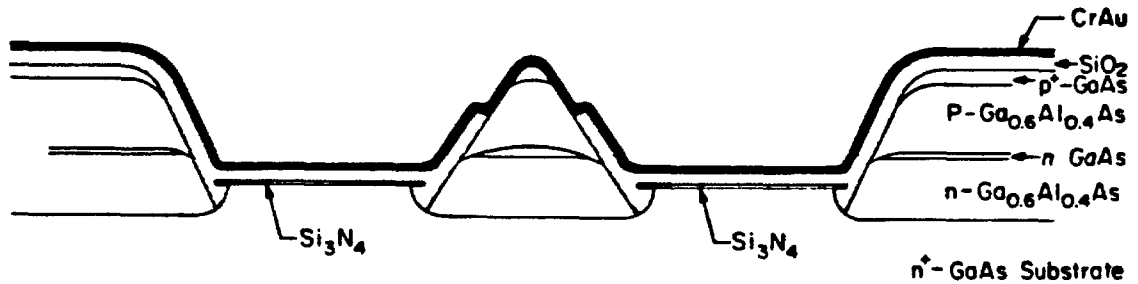
Figure 4.2- 2. Schematic cross section of the Embedded Stripe Laser

the center layer is 1.4 μm, and its thickness in the center is about 0.3 μm.

4.2.3 Fabrication Procedure

Some of the processing steps are common to the fabrication of the Embedded Stripe Laser and the Translaser. Missing details on these steps can be found in the subsection describing the fabrication procedure of the Translaser (Section 2.2–3). Fabrication of the device starts with the deposition of Si_3N_4 film on a (100) oriented, Te-doped n^+-$GaAs$ substrate. The thickness of the film is a few hundred Å, and the deposition temperature is 690 °C. Most of the nitride area, except for two 5 μm
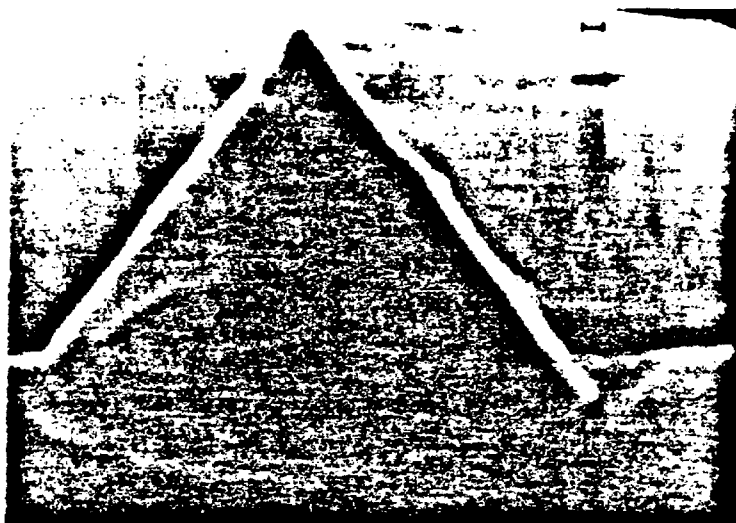
Figure 4.2- 3. Example of small structure dimensions obtainable with the new growth technique. (The length bar is 0.1 μm)

stripes with a 5 μm spacing between them is etched away, using Buffered–HF solution for ≈ 2 minutes. This pattern is repeated every 250 μm. Devices with different dimensions were also fabricated, and 5 μm is a typical value.

The typical parameters of the layers grown in the liquid phase epi-

taxy process are given in Table 4.2−1.

TABLE 4.2- 1. Growth Parameters of Embedded Stripe Lasers

Layer	Type	Thickness [μm]	Al contents (x)	Doping	
				Dopant	Conc. [cm^{-3}]
lower cladding	n	2.0	0.4	Sn	1×10^{17}
active region	n (undoped)	0.3	0.0		$\approx 5 \times 10^{16}$
upper cladding	p	2.0	0.4	Ge	1×10^{17}

The cooling rate employed during the growth process was the normal 0.4 $°C/\min$. There is no need for slower cooling rate for achieving controlled and reproducible results. The particular shape of the active region depends on the exact details of the growth process (e.g., the time that this layer was grown, the thickness of the lower cladding layer, the orientation of the substrate crystal). A typical active region is crescent shaped, with about 0.3 μm thickness in the center.

A SiO_2 film (Thickness ≈ 2500 Å) is deposited on the growth, and stripes are opened along the center of the laser mesas using regular photolithographic techniques. Because the thickness of the photoresist around the laser mesa is larger than in other places, the accuracy of the stripe registration in this photolithographic step is not critical. Cr-Au is

evaporated as the p-type contact. The wafer is then lapped, and $AuGe/Au$ is evaporated as the n-type contact, followed by alloying at 360 °C. The last step is cleaving the wafer to devices with lengths in the 125 to 325 μm range.

During the growth, the facets of the layers at the stripe edges (which are the (111) surfaces) grow at an angle of about 55° with respect to the (100) substrate surface, as described in Section 4.2–1. The laser mesa grows at the nominal rate until the triangle shape is completed. After that, the growth rate on the mesa is much smaller, while at the other parts of the wafer it is unchanged. This confirms the fact that the growth takes place first on the (100) surfaces, and only later, and at a much slower rates, on the (111) surfaces. If the growth is continued under these conditions, we get intolerably large differences in height between the mesa and its surroundings. This makes it difficult to apply the p-contact to the device. As mentioned before, the exact shape of the grown structure also depends on the orientation of the stripes. It was found, in agreement with the results of Lee [6], that if the stripes are perpendicular to the (011) cleavage plane, the growth rate is higher than in the case where the stripes are perpendicular to the (01$\overline{1}$) cleavage plane. This causes the lasers grown using the first orientation to have somewhat thicker active regions.

SEM photographs of cross sections of typical devices grown in both orientations are shown in Figure 4.2–4. It was recently found that lasers with curved active layers give better results in terms of spatial mode stability [9].
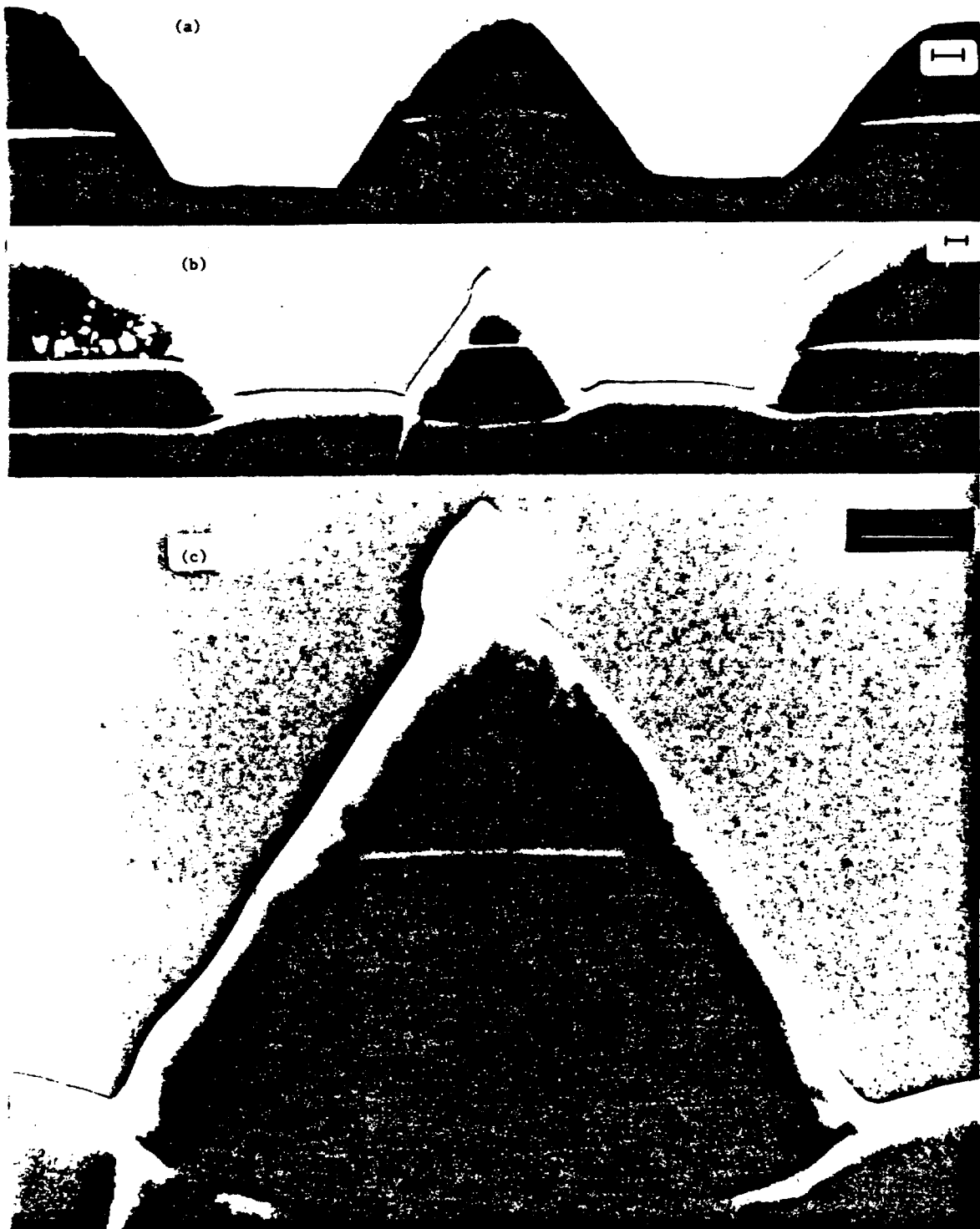
Figure 4.2-4. SEM photographs of a)device grown with mesa perpendicular to (01$\underline{1}$) orientation. b)device grown with mesa perpendicular to (011) orientation. c)enlarged photograph of b). (the length mark is 1μm)

4.2.4 Experimental Results

· As explained in the introduction to this chapter, the main motivation in developing this type of laser was to obtain a low-threshold single-mode source. Typical values of the room temperature pulsed threshold current of the laser (I_{th}) versus the laser length (L) are shown in Figure 4.2-5. Typical values of threshold currents are 15-20 mA for 200 μm lasers and 25-30 mA for 300 μm lasers. These are very low values, comparable to the threshold currents of the BH lasers. CW threshold currents are about 15% above the pulsed threshold values.

The threshold current of the laser is a monotonically increasing function of the temperature. The exact theoretical calculation of this dependence is complicated [10], and for all practical purposes the following empirical formula is used:

$$I_{th}(T_2) = I_{th}(T_1)e^{\frac{T_2-T_1}{T_0}}$$

where T_0 is usually called the characteristic temperature of the laser. This relation holds for a temperature region of a few tens of degrees about room temperature. Because of reliability considerations, high values of T_0 are desired. High values of T_0 were measured for the Embedded Stripe Laser. Typical results are $T_0 = 175°$ in the temperature range of $20°C < T < 90°C$ and $T_0 = 160°C$ in the $20°C < T < 135°C$. This means that when operating at 75°C, I_{th} is increased by only 33% compared to its room temperature value.

The linearity of the light versus current characteristic is another
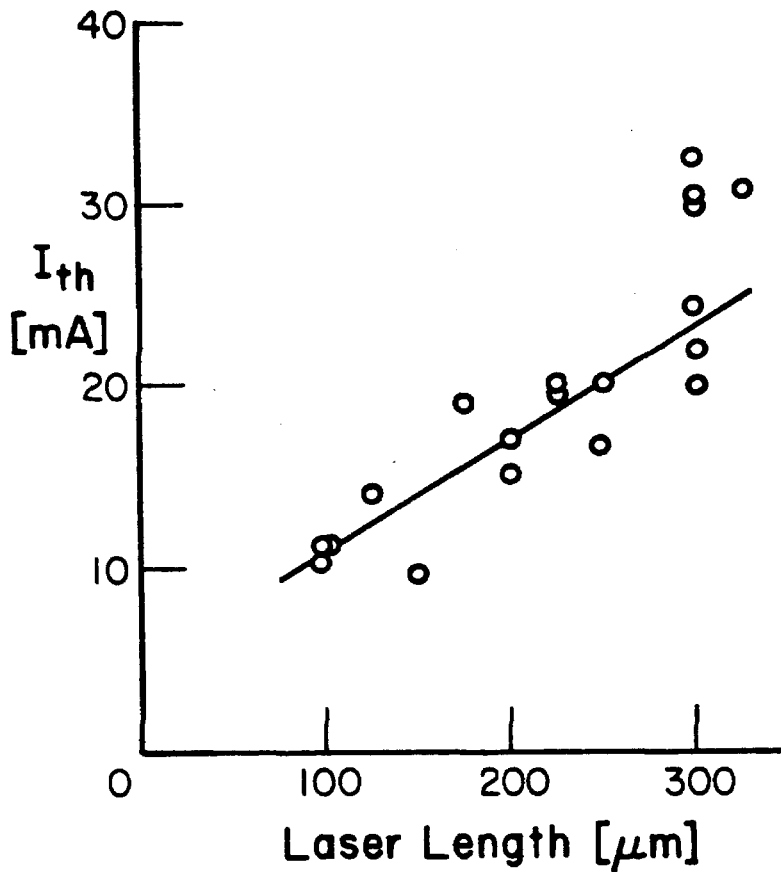
Figure 4.2- 5. Dependence of the lasers threshold current (I_{th}) on the laser length (L)

important parameter of a laser diode. Nonlinearities, or "kinks", are very

undesirable since they are usually accompanied by mode instabilities

and thus impose severe limitation on the operation of the device in many

applications [11]. The light versus current curve of a typical Embedded

Stripe Laser is linear and kink-free up to power levels of about 12

mW/facet. This is true even for devices that do not operate in the

fundamental spatial mode, but rather in some higher order mode. The external differential quantum efficiency (η_D) of the lasers are about or above 45%. Values of η_D quoted above are for 225 μm-long lasers. The dependence of η_D on the laser length is given in the following theoretical expression:

$$\eta_D = \eta_i \left[1 - \frac{\alpha_i L}{\ln R} \right]^{-1} \qquad (4.2\text{-}2)$$

where η_i is the internal quantum efficiency (basically a phenomenological-empirical factor representing all kinds of imperfections in the real lasers), α_i is the total internal optical losses in the laser (except mirror losses), L is the length of the laser and R is the mirrors reflectivity.

Measurements of the near field and the far field patterns show that lasers with narrow active regions ($\lesssim 0.3\mu m$) tend to operate in the fundamental spatial mode in current levels up to more than three times the threshold current. A typical far field pattern of such lasers in the direction parallel to the junction plane is shown in Figure 4.2-6. The half-beam width of the mode is about 30°. Devices with thicker active regions ($\gtrsim 0.4\mu m$) develop higher order modes at about 1.4×I_{th}. Lasers with wider active regions can operate stably in some higher order mode. An example of such modes is shown in Figure 4.2-7. The Embedded Stripe Lasers tend to operate in a low number ($\approx 1-5$) longitudinal modes. A considerable fraction of them operate in a single longitudinal mode, which is important for applications involving high data rate single mode optical fiber systems. A typical example of a spectrum of single
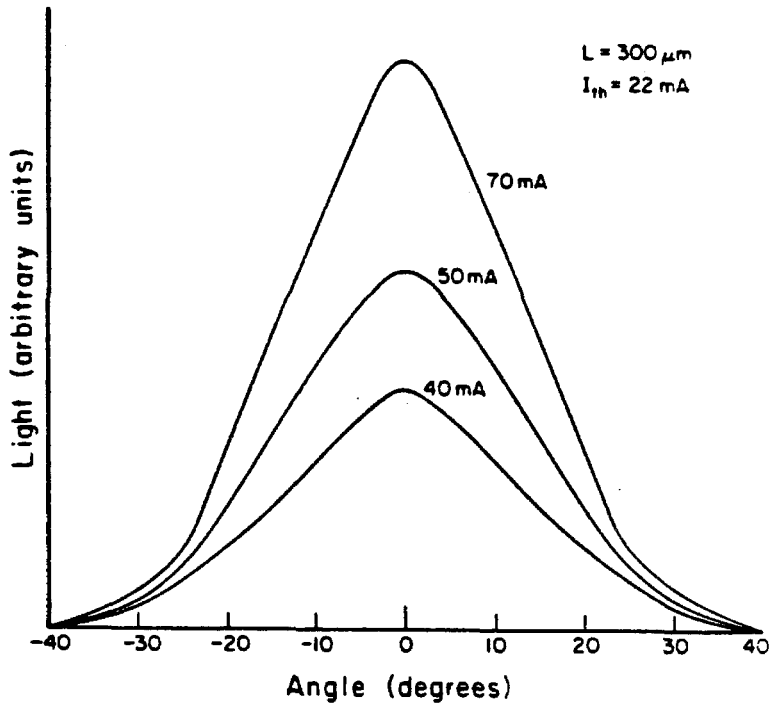
Figure 4.2- 6. Typical far field pattern of a laser operating at the fundamental spatial mode

longitudinal mode laser is shown in Figure 4.2−8. The device maintained this single mode behavior up to current levels of more than $4 \times I_{th}$. At the higher current region there is a small shift ($\approx +20\text{Å}$) in the oscillation wavelength, which is due to thermal effects.
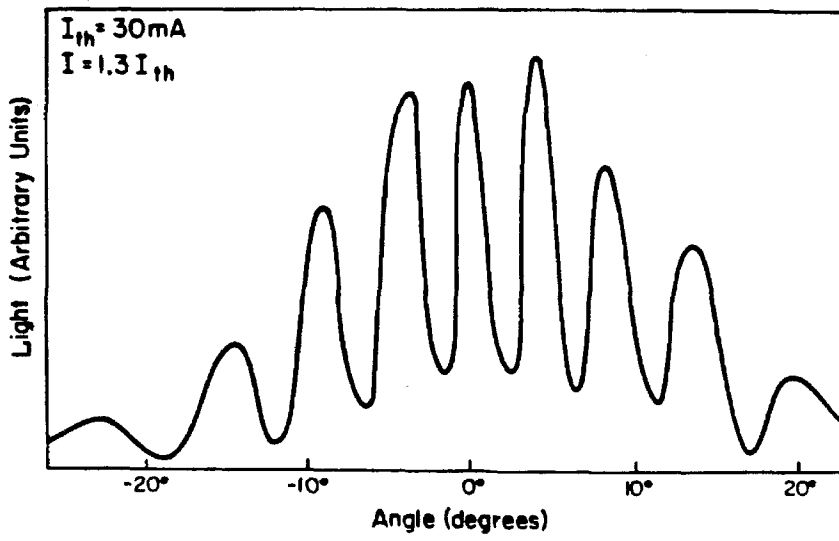
Figure 4.2- 7. Far field patterns of a laser operating in a 9- th order mode.

Figure 4.2-8. Spectrum of a single longitudinal mode laser. (The horizontal scale depicts wavelengths in Å)

4.3 Buried Heterostructure AlGaAs Lasers on Semi- Insulating Substrates

4.3.1 Principles of Operation

There are two basic prerequisites for lasers to be effectively used as a component of an optoelectronic integrated circuit. First, the laser should possess good properties, such as low threshold current and single spatial mode operation, and second, it has to be grown on a substrate that is suitable for integ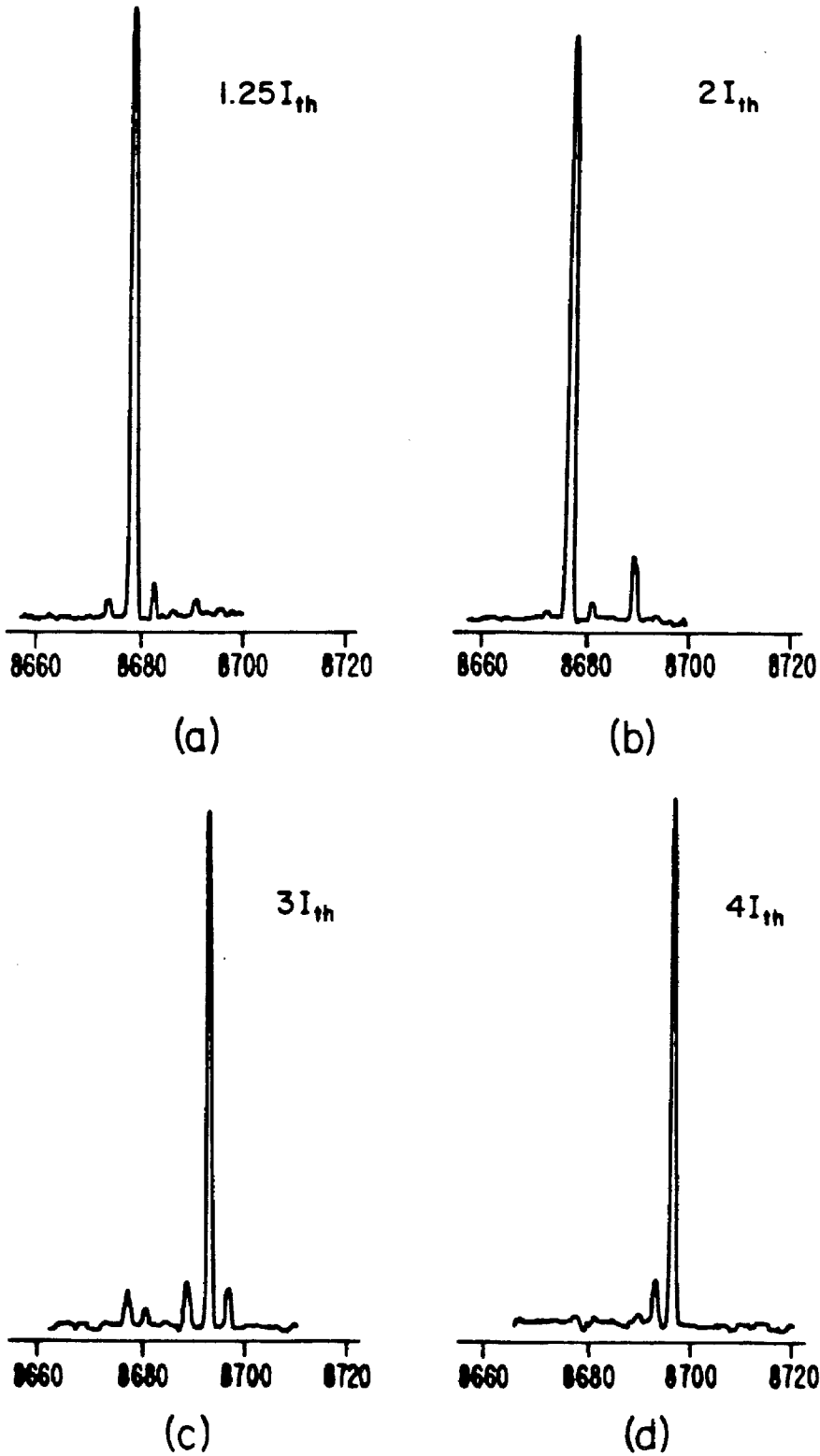ration with other electronic devices. For devices made of the ternary AlGaAs system, Semi–Insulating (SI) GaAs crystals are the most suitable substrates for these purposes.

Operation of several types of injection lasers grown on SI GaAs sub−strates have recently been demonstrated. Among these are the Crowding Effect Laser [12], the T−Laser [13], the Transverse Junction Stripe (TJS) laser [14], and the Beryllium Stripe Laser [QQaq]. Integration of these lasers with several electronic components has also been achieved [13], [15]−[17].

One type of laser that is an attractive candidate for this type of applications is the Buried−Heterostructure (BH) laser [3]. In a manner similar to the Embedded Stripe Laser described in the preceding section of this chapter, the BH laser also has an active region which is com−pletely embedded in AlGaAs material with a wider bandgap and a smaller index of refraction, thus providing a two−dimensional waveguiding and carriers confinement. The attractive features of this laser include low threshold current, stable spatial mode operation, flat frequency response and linear light−current characteristics.

However, so far this type of laser has been fabricated on conductive substrates only. The BH laser described in this section is fabricated on a SI $GaAs$ substrate [18]. The cross-section of the device is shown in Figure 4.3-1. Several things are worth noting about this structure. The n^+-GaAs layer serves not only as the cathode of the laser, but also as a buffer layer between the substrate and the double- heterostructure. The introduction of a buffer layer reduces the anmount of defects in the active region of the laser due to defects in the substrate, thus increasing the lifetime of the device [19]. Growing the active region with a small aluminum contents ($x \approx 0.05$) was also found to increase the device lifetime [1].

The main advantage of fabricating the laser on a semi-insulating substrate is that other parts (of the substrate) can be utilized for the fabrication of electronic devices such as photodetectors or field-effect-transistors, which are necessary for opoelectronic circuits like transmitters and repeaters. The realization of the Buried Optical Guide laser [8] can be similarly achieved, thus leading to devices that emit higher optical powers without a considerable increase in the threshold current. The operation of a $GaInAsP$ BH laser on a SI InP substrate has also been demonstrated recently [20].

4.3.2 Fabrication Procedure

Some of the processing steps are common to the fabrication of the BH laser on a SI substrate and the Translaser. Missing details on these steps can be found in the subsection describing the fabrication pro-
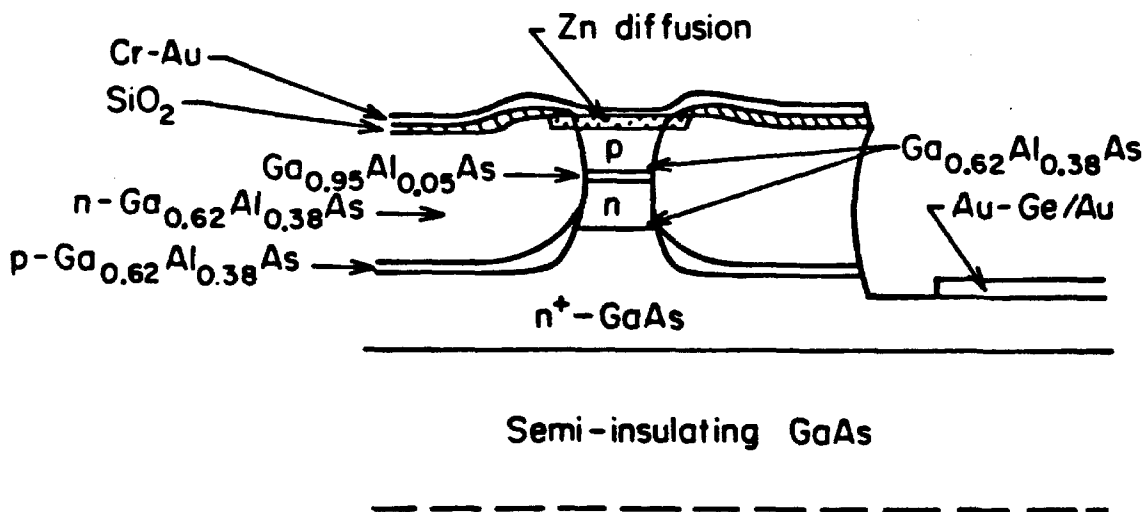
Figure 4.3- 1. Schematic cross- section of a BH laser grown on a SI substrate

cedure of the Translaser. (Section 2.2–4).

As is the case with the regular BH laser, the device described here is also fabricated by a two–step liquid phase epitaxy. The substrate used is a (100)–oriented Cr–doped Semi–Insulating (SI) $GaAs$ substrate. The resistivity of the substrate material is more than $1 \times 10^7 \Omega$ –cm. This high value of resistivity is due to a reduction of the carrier lifetime by the Cr dopant.

The details of the structure grown in the first step are given in Table 4.3–1. A schematic cross–section of the structure after the first growth is shown in Figure 4.3–2a. In some of the devices an additional layer was

TABLE 4.3- 1. Parameters of the first growth step of a BH laser on a SI substrate

Layer	Type	Thickness [μm]	Al contents (x)	Doping Dopant	Doping Conc[cm^{-3}]
buffer layer	n^+	4.0	0.0	Te	2×10^{18}
lower cladding	n	1- 1.5	0.38	Sn	1×10^{17}
active region	n (undoped)	0.2- 0.25	0.25		$\approx 5 \times 10^{16}$
upper cladding	p	1- 1.5	0.38	Ge	5×10^{17}

grown between the buffer and the lower cladding layers. This layer is Sn-doped ($N_D \approx 5 \times 10^{17} cm^{-3}$), and its thickness is $\leq 0.5 \mu m$. Its function is to prevent the growth defects that result when an $AlGaAs$ layer is grown directly on a highly Te doped layer. After the growth, a mesa is etched down to the n^+-GaAs layer, with the mesa direction parallel to the $< 1\overline{1}0 >$ direction. The etchant used is 1:8:8 ($H_2SO_4 : H_2O_2 : H_2O$) solution, and the resulting cross-section of the mesa has the inverted trapezoidal shape. The stripe at the active region is about $2 \mu m$. (See Figure 4.3-2b).

Then the second step of the growth is performed. The parameters of the layers grown in the second step are given in Table 4.3-2. The cross-section of the laser after this growth step is shown in Figure 4.3-
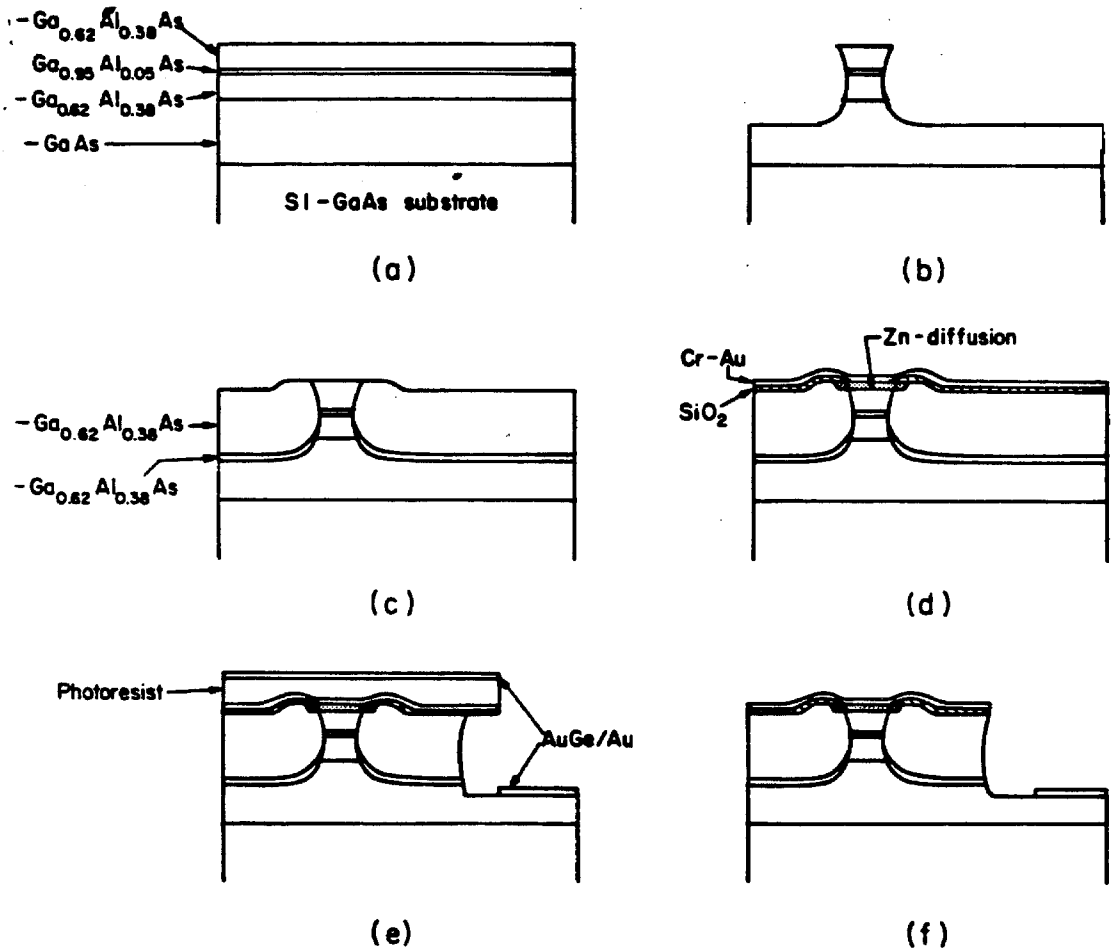
Figure 4.3- 2. Steps in fabrication of BH laser on a SI substrate. a) After the first growth step. b) After the etching of the laser mesa. c) After the second growth step. d) After applying the p contact. e) After etching the second mesa, before the lift- off. f) The final device.

2c. The order of the layers forms an inverted n–p junction in parallel with the p–n junction in the laser mesa, thus reducing the current leaking.

TABLE 4.3- 2. Parameters of the second growth step of a BH laser on a SI substrate

Layer	Type	Thickness $[\mu m]$	Al contents (x)	Doping	
				Dopant	Conc$[cm^{-3}]$
lower burying layer	p	≈ 0.3	0.38	Ge	1×10^{17}
upper burying layer	n	≈ 2.5	0.38	Sn	1×10^{17}

After the growth the wafer is covered with a SiO_2 film. Using conventional photolithographic techniques, stripes are opened in the SiO_2 film above the laser mesa, and a shallow Zn diffusion is performed in order to obtain a better contact to the laser anode. This is followed by an evaporation of $Cr-Au$ to form the p contact. A cross-section of the device at this stage is shown in Figure 4.3-2d.

In order to apply the cathode contact, a second mesa is formed at a distance of about $50\mu m$ from the laser mesa by etching down to the n^+- $GaAs$ layer (using the same etchant as before). Using a lift-off technique, the n contact is formed by an evaporation of $Cr-Au$ and Au, followed by alloying. Figures 2.4-2e and 2.4-2f depicts the structure of the device before and after this final lift-off process, respectively. Since both the p and the n contacts are on the upper side of the device, the

lasers are mounted with the junction up on a copper heat−sink.

4.3.3 Experimental Results

The threshold current is approximately 8 $mA/\mu m$ stripe width for devices with $300\mu m$ cavity length. These results are in agreement with the results reported on BH lasers on conductive substrates [8]. The typical series resistance of the devices was 15Ω, compared to 10Ω for vertical BH lasers (i.e., BH lasers on conductive substrates). However, due to the low operating currents ($\approx 20-30$ mA), this gives rise only to a small increase ($\approx 10\%$) in heat dissipation.

The light versus current characteristics are linear up to average power levels of $10mW$, with differential quantum efficiencies of 55%. A stable fundamental transverse mode is found in the lasers with stripe width of $2\mu m$. This value is somewhat better than that predicted by theory [8], and might be due to the asymmetry in the current injection. The far field patterns of two devices are shown in Figure 4.3−3. Figures 4.3−3a and 4.3−3b show typical patterns of devices operating in the fundamental and the first order modes, respectively. No significant asymmetry was observed in the light intensity patterns.
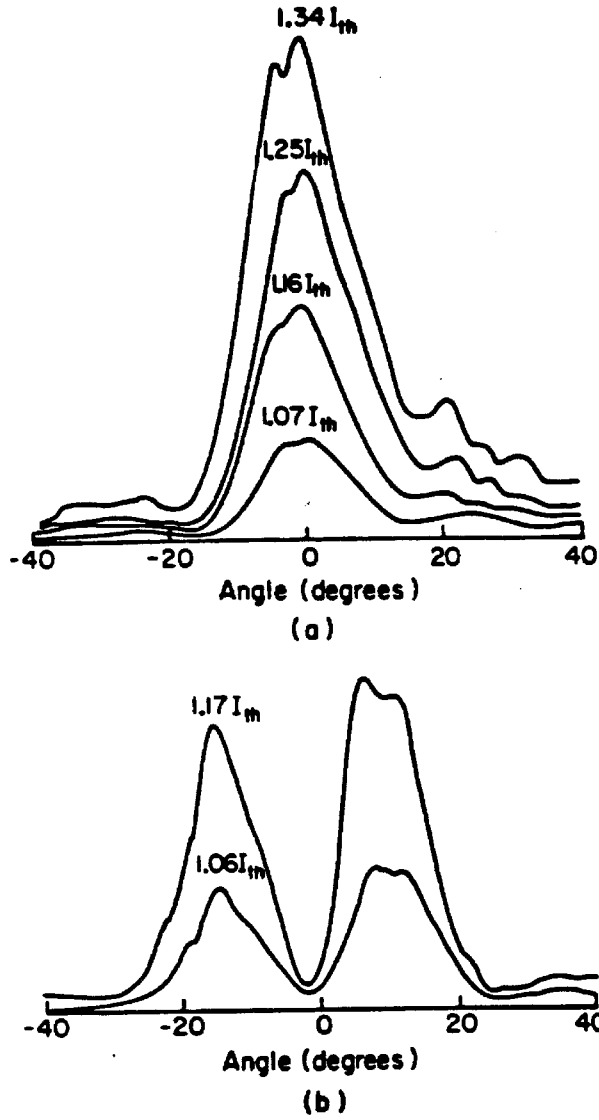
Figure 4.3-3. Typical far-field patterns of the buried-heterostructure laser (vertical scale - arbitrary units) on a SI *GaAs* substrate. a) 2 μm stripe width. b) 3 μm stripe width

References for Chapter 4

[1] M. Ettenberg and H. Kressel, "The Reliability of $(AlGa)As$ CW Laser Diodes", IEEE J. Quant. Electron., **QE-16**, pp 186–196 (1980)

[2] J. Katz, S. Margalit, D. Wilt, and A. Yariv, "Single Growth Embedded Epitaxy $AlGaAs$ Injection Lasers with Extremely Low Threshold Currents", Appl. Phys. Lett., **37**, pp 987–989 (1980)

[3] T. Tsukada, "$GaAs - Ga_{1-x}Al_xAs$ Buried–Heterostructure Injection Lasers", J. Appl. Phys., **45**, pp 4899–4906 (1974)

[4] I. Samid, C. P. Lee, A. Gover, and A. Yariv, "Embedded Heterostructure Epitaxy: A Technique for Two–Dimensional Thin Film Definition" Appl. Phys. Lett., **27**, pp 405–407 (1975)

[5] C. P. Lee, I. Samid, A. Gover, and A. Yariv, "Low Threshold Room Temperature Embedded Heterostructure Lasers", Appl. Phys. Lett., **29**, pp 365–367 (1976)

[6] C. P. Lee, *New Optoelectronic Devices Using GaAs–GaAlAs Epitaxy*, Ph.D Thesis, California Institute of Technology, Pasadena, 1978

[7] D. W. Bellavance and J. C. Campbell, "Room Temperature Mesa Lasers Grown by Selective Liquid Phase Epitaxy", Appl. Phys. Lett., **29**, pp 162–164 (1976)

[8] K. Saito and R. Ito, "Buried Heterostructure $AlGaAs$ Lasers", IEEE J. Quant. Electron., **QE-16**, pp 205–215 (1980)

[9] W. Streifer, R. D. Burnham, and D. R. Scifres, "Analysis of Diode Lasers with Lateral Spatial Variations in Thickness", Appl. Phys.

Lett., **37**, pp 121–123 (1980)

[10] H. Kressel and J. K. Butler, *Semiconductor Lasers and Heterojunction Leds*, Academic Press, New York, 1977, pp 275–280

[11] H. C. Casey, Jr. and M. B. Panish, *Heterostructure Lasers*, Academic Press, New York, 1978, Part A, pp 180–181

[12] C. P. Lee, S. Margalit, and A. Yariv, "Double Heterostructure *GaAs-GaAlAs* Injection Lasers on Semi–Insulating Substrates Using Carrier Crowding", Appl. Phys. Lett., **30**, pp 281–282 (1978)

[13] I. Ury, S. Margalit, M Yust, and A. Yariv, "Monolithic Integration of an Injection Laser and a Metal Semiconductor Field Effect Transistor", Appl. Phys. Lett., **34**, pp 430–432 (1979)

[14] C. P. Lee, S. Margalit, I. Ury, and A. Yariv, "*GaAs-GaAlAs* Injection Lasers on Semi–Insulating Substrates Using Laterally Diffused Junctions", Appl. Phys. Lett., **32**, pp 410–412 (1978)

[15] D. Wilt, N. Bar–Chaim, S. Margalit, I. Ury, M. Yust, and A. Yariv, "Low Threshold *Be* Implanted (*GaAl*)*As* Laser on Semi– Insulating Substrate", IEEE J. Quant. Electron., **QE-16**, pp 390–391 (1980)

[16] C. P. Lee, S. Margalit, I. Ury, and A. Yariv, "Integration of an Injection Laser with a Gunn Oscillator on a Semi–Insulating *GaAs* Substrate", Appl. Phys. Lett., **32**, pp 806–807 (1978)

[17] M. Yust, N. Bar–Chaim, S. H. Izadpanah, S. Margalit, I. Ury, D. Wilt, A. Yariv, "A Monolithically Integrated Optical Repeater", Appl. Phys. Lett., **35**, pp 795–797 (1979)

[18] N. Bar–Chaim, J. Katz, I. Ury, and A. Yariv, "Buried–Heterostructure *AlGaAs* Lasers on Semi–Insulating Substrates", Electron. Lett., **17**, pp 108–109 (1981)

[19] K. Shima, N. Takagi, K. Segi, H. Imai, K. Hory, and M. Takusagawa, "Improvement of Photoluminiscence Property of *(GaAl)As* Double– Heterostructure Laser Wafer with Buffer Layer", Appl. Phys. Lett., **36**, pp 395–397 (1980)

[20] T. Matsuoka, K. Takahei, Y. Noguchi, and H. Nagai, "1.5μm Region *InP/GaInAsP* Buried Heterostructure Lasers on Semi–Insulating Substrates", Electron. Lett., **17**, pp 12–14 (1981)

5. THE INTRINSIC ELECTRICAL EQUIVALENT CIRCUIT OF A LASER DIODE

5.1 Introduction

In this chapter an electrical model of the laser diode is developed [1]. This model provides better understanding of the electrical behavior of the laser diode. The common method of characterizing the temporal response of the laser diode is by its light versus current frequency transfer function. However, many applications, and in particular those which involve high- frequency modulation or combined operation with other electronic components and circuits (i.e., devices such as the laser- MESFET combination [2], the repeater [3] or the Translaser [4]), require an accurate representation of the electrical impedance characteristics of the laser. It should be always kept in mind that besides the fact that it emits light, the laser diode is also an electronic device, and the current flowing through it and the voltage developed across its terminals must be calculated as a part of the design of the whole circuit.

The DC current-voltage characteristics and the elements of the laser equivalent circuit (i.e., its impedance function) are derived from the rate-equations [5], which describe the interplay between the optical intensity (or, equivalently, the photon density) and the charge carriers. These equations are augmented by the voltage-carrier-density relation of the injection junction.

5.2 The Rate Equations and the Carrier- Density Voltage Relation

The rate equations used in this section are taken from Kressel and Butler [5]. Because of quasi-neutrality, a rate-equation for only one type of charge carriers, e.g., electrons, will be needed. The electron density N_e obeys the following equation:

$$\frac{dN_e}{dt} = \frac{I}{qad} - A\,(N_e - N_{om})N_{ph} - \frac{N_e}{\tau_S} \qquad (5.2-1)$$

and a similar equation holds for the photon density N_{ph}:

$$\frac{dN_{ph}}{dt} = A\,(N_e - N_{om})N_{ph} - \frac{N_{ph}}{\tau_{ph}} + \beta\frac{N_e}{\tau_S} \qquad (5.2-2)$$

where I is the current flowing through the diode, a is the diode area, d is the thickness of the active region, q is the electronic charge, A is a proportionality constant, N_{om} is the minimum electron-density required to obtain positive gain, τ_S is the spontaneous lifetime of the charge carriers, τ_{ph} is the photons lifetime and β is the fraction of the spontaneous emission that is coupled into the lasing mode. β is usually a number of the order of $1\times10^{-4\pm1}$. The dependence of beta on the device parameters can be found in various references [6], [7].

The first term on the right-hand side of Equation (5.2-1) accounts for carriers injected into the active region. The second and the third terms account for charge carriers lost in stimulated and spontaneous recombination, respectively. Similarly, in Equation (5.2-2) the first term

on the right−hand side represents photons generated by stimulated recombination of carriers, the second − photons lost (i.e., by absorption or mirror loss), and the third − photons added to the lasing mode from the spontaneous emission.

The assumptions implied in formulating Equations (5.2−1) and (5.2−2) are that the laser oscillates in a single mode, the inversion (gain) is homogeneous and the gain is linear in the difference between N_e and N_{om}. Although the above set of equations is a simplified representation of the behavior of the laser diode, they yield results which contain most of the basic important phenomena relevant to the operation of the device.

The junction voltage V is introduced into the equations through its relation to the carrier density N_e. Since the effective density of states in the conduction band (N_C) of $GaAs$ is smaller than the carriers density at threshold $(N_{e,th})$, Boltzmann's statistics are not accurate for this band. For the valence band Boltzmann's statistics are still a resonable approximation even at the threshold, since N_V is considerably larger than N_{th}. $(N_C = 4.3 \times 10^{17} cm^{-3}$, $N_V = 8.9 \times 10^{18} cm^{-3}$, and $N_{e,th} \approx 1-2 \times 10^{18} cm^{-3})$. Using the inverted expansion of the Fermi−Dirac integral developed by Joyce and Dixon [8], keeping only the first correction term, and assuming an undoped active region (or more realistically, high level injection conditions), the following relation is obtained between the carriers density and the junction voltage:

$$V = \frac{2KT}{q}\left(\ln\frac{N_e}{n_i} + \frac{1}{4\sqrt{2}}\frac{N_e}{N_C}\right) \qquad (5.2\text{-}3)$$

where n_i is the intrinsic carrier density in *GaAs*. The error in Equation (5.2-3) is about 2% at throshold for $\frac{N_{e,th}}{N_C} \approx 3$. This is accurate enough for all practical calculations based on the independent— particle parabolic—band approximation. Higher order terms of the expansion can be included if a better accuracy is needed.

5.3 Current- Voltage Characteristics

·The DC current–voltage (I–V) characteristic is found from the steady- state solution of the rate–equations. Seting $\frac{d}{dt} = 0$ in Equations (5.2-1) and (5.2-2), eliminating the photon density from the resulting equations and using Equation (5.2-3), the following I–V relation is obtained:

$$V = V_{om} + \frac{2KT}{q}\left[\ln\frac{b - \sqrt{b^2 - c}}{2(1 - \beta)} + \frac{1}{4\sqrt{2}}\frac{N_{om}}{N_C}\frac{b - \sqrt{b^2 - c}}{2(1 - \beta)} \right] \qquad (5.3-1)$$

where all the parameters in Equation (5.3-1) are defined as follows:

$$V_{om} = \frac{2KT}{q}\ln(\frac{N_{om}}{n_t}) \qquad (5.3-2)$$

$$b = 1 + [A\,\tau_{ph}N_{om}]^{-1} + i^0 - \beta \qquad (5.3-3)$$

$$c = 4i^0(1 + [A\,\tau_{ph}N_{om}]^{-1})(1- \beta) \qquad (5.3-4)$$

$$i^o = \frac{\tau_S}{N_{om}qad}I \qquad (5.3-5)$$

At current levels below threshold, and assuming Boltzmann's statistics, Equation (5.3-1) reduces to the usual diode equation, i.e.

$$V = \frac{2KT}{q}\ln(\frac{\tau_S I}{n_i qad})$$

(5.3−6)

and at current levels above threshold the voltage is effectively clamped to a value of

$$V = V_{om} + \frac{2KT}{q}\left(\ln\zeta + \frac{N_{om}}{8\sqrt{2}(1-\beta)N_C}\zeta\right)$$

(5.3−7)

(where $\zeta = 1 + [A\,\tau_{ph}N_{om}]^{-1} - \beta$), a fact that represents the laser gain clamping associated with the lasing threshold . In the next section it will be shown that the voltage clamping does not exist at high frequencies.

5.4 The Impedance Function of the Laser Diode

The laser model will be developed in three steps. Each step will introduce a new physical phenomenon that pertains to the operation of the laser. In the first step we assume $\beta = 0$ in Equation (5.2-2), i.e., the laser is modeled as a classical oscillator above threshold, and as a regular diode below threshold. We will solve for the impedance function above threshold, since below threshold $N_{ph} \equiv 0$ when $\beta = 0$. Next, a small–signal analysis is performed on Equations (5.2-1) to (5.2-3). The parameters in the equations are expanded in the following fashion:

$$N_e \approx N_e^0 + N_e^1 e^{i\omega t} \tag{5.4-1a}$$

$$N_{ph} \approx N_{ph}^0 + N_{ph}^1 e^{i\omega t} \tag{5.4-1b}$$

$$V \approx V^0 + V^1 e^{i\omega t} \tag{5.4-1c}$$

where N_e^0, N_{ph}^0, V^0, and N_e^1, N_{ph}^1, V^1 are the quiescent and the small signal values, respectively, of N_e, N_{ph} and V. By using Equation (5.4-1) in Equations (5.2-1) to (5.2-3), the differential equations become algebraic equations since $\frac{d}{dt}$ is replaced by $i\omega$. It is also assumed that $N_e^1 << N_e^0$, $N_{ph}^1 << N_{ph}^0$, and $V^1 << V^0$. The above analysis results in the following impedance functon:

$$Z(\omega) \triangleq \frac{V(\omega)}{I(\omega)} = \frac{i\dfrac{\omega}{C}}{-\omega^2 + i\dfrac{\omega}{RC} + \dfrac{1}{LC}}$$

$$(5.4-2)$$

$V(\omega)$ and $I(\omega)$ are the complex amplitudes of the small−signal junction voltage and current, respectively, and

$$R = R_d \frac{I_{th}}{I^0} \qquad (5.4-3a)$$

$$L = R_d \tau_{ph} \frac{1}{\dfrac{I^0}{I_{th}} - 1} \qquad (5.4-3b)$$

$$C = \frac{\tau_S}{R_d} \qquad (5.4-3c)$$

where

$$R_d = \frac{2KT}{q} \left(1 + \frac{1}{4\sqrt{2}} \frac{N_e^0}{N_C}\right) \frac{1}{I_d} \qquad (5.4-4)$$

is the expression of the differential resistance of the diode, I^0 is the bias current of the laser diode, and I_d is a normalized current given by

$$I_d = \frac{N_e^0}{\tau_S} aqd \qquad (5.4-5)$$

$I_d = I^0$ for $I^0 < I_{th}$, and $I_d = I_{th}$ for $I^0 > I_{th}$. In *AlGaAs* lasers, typical values of R are about or less than 1Ω, of $L-$ about $1pH$, and of $C -$ a few

nF. The impedance given in Equation (5.4-2) is that of a parallel RLC circuit (Figure 5.4-1a). For currents below threshold the model reduces to the usual diode model, i.e. a parallel RC circuit, with $R = \dfrac{2\,KT}{qI^0}$ and $C = \dfrac{\tau_S}{R}$. It should be noted that for currents greater than the threshold current, $N_e^0 = N_{e,th}$.
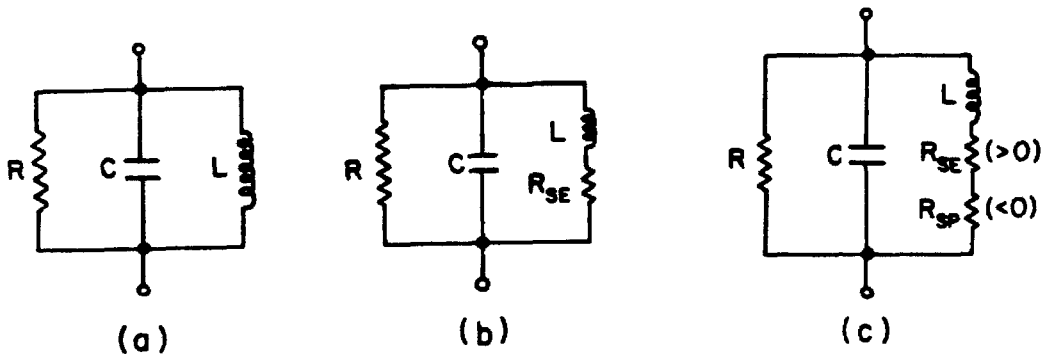

Figure 5.4- 1. Models of the laser diode. a) basic model - no spontaneous emission. b) including spontaneous emission. c) including spontaneous emission and saturable absorption.

The problems with this basic model (which is similar to the one developed recently by Morishita et al [9]) is that it does not take into account the physical phenomena of spontaneous emission into the laser

mode and of saturable absorption (or, equivalently, non−linear gain), and consequently fails to predict the occurrence of self−pulsations and its disturbing effect on the modulation frequency response, and the interplay between the spontaneous emission and the self−pulsations.

In the second step the interaction of the spontaneous emission with the laser mode is taken into account. Again a small signal analysis is performed on Equations (5.2−1) to (5.2−3), but now without the assumption that $\beta = 0$.

This analysis results in the following impedance function:

$$Z(\omega) = \frac{i\frac{\omega}{C} + \frac{R_{se}}{LC}}{-\omega^2 + i\omega(\frac{1}{RC} + \frac{R_{se}}{L}) + \frac{1}{LC}(1 + \frac{R_{se}}{R})} \qquad (5.4-6)$$

The impedance function of Equation (5.4−6) is that of a parallel RLC circuit with a resistor R_{se} in series with the inductance (Figure 5.4−1b). The values of the components are:

$$R = \frac{R_d}{n_{ph}^0 + 1} \qquad (5.4-7a)$$

$$L = \frac{R_d \tau_{ph}}{(n_{ph}^0 + \beta)(n_e^0 - n_{om})} \approx \frac{R_d \tau_{ph}}{n_{ph}^0} \qquad (5.4-7b)$$

$$C = \frac{\tau_s}{R_d} \qquad (5.4-7c)$$

$$R_{so} = \beta R_d \frac{n_e^0}{n_{ph}^0 (n_{ph} + \beta)(n_e^0 - n_{om})} \approx \beta R_d \frac{n_e^0}{(n_{ph}^0)^2} \qquad (5.4-7d)$$

where n_{ph}^0, n_e^0 and n_{om} are the normalized steady-state values of N_{ph}^0, N_e^0 and N_{om}, respectively. ($n_{ph}^0 = A \tau_S N_{ph}^0$, $n_e^0 = A \tau_{ph} N_e^0$, and $n_{om} = A \tau_{ph} N_{om}$). In order to see how this model reduces to the basic one, it should be noted that when $\beta = 0$, $n_{ph}^0 = \frac{I^0}{I_{th}} - 1$ if $I^0 > I_{th}$, and $n_{ph}^0 = 0$ if $I^0 < I_{th}$.

In the third step of developing the electrical model of the laser diode, phenomena that cause self-pulsations are also included. These phenomena can be accommodated in the model by including a saturable absorption term in the rate equation for the photons [10].

$$\frac{dN_{ph}}{dt} = A (N_e - N_{om}) n_{ph} + \beta \frac{N_e}{\tau_S} - \frac{n_{ph}}{\tau_{ph}} \left[1 + \frac{\delta}{1 + \frac{N_{ph}}{N_S}} \right] \qquad (5.4-8)$$

where δ is a parameter denoting the strength of the non-linearity ($\delta \approx 0.02$ [10]) and N_S is the saturation density of the photons ($N_S \approx 1 \times 10^{13} - 1 \times 10^{14} cm^{-3}$ [10], [11]). Basically, δ and N_S are phenomenological parameters, whose values are chosen so that the calculations will conform to experimental results. Due to various degradation mechanisms of the laser diode, both δ and N_S can change as the laser ages.

Performing small-signal analysis on Equations (5.2-1), (5.2-3) and

(5.4−8), we find that the effect of saturable absorption is to introduce in the equivalent circuit a negative resistance R_{sp} which is in series with the inductance (Figure 5.4−1c). The value of this resistance is:

$$R_{sp} = -R_d \frac{\delta}{n_S} \frac{n_{ph}^0}{(1 + n_{ph}^0/n_S)^2 (n_{ph}^0 + \beta)(n_e^0 - n_{om})} \qquad (5.4-9)$$

$$\approx - R_d \frac{\delta}{n_S} \frac{1}{\left(1 + \frac{n_{ph}^0}{n_S}\right)^2}$$

where n_S is the normalized photon saturation density $(n_S = A \tau_S N_S)$, and it is connected in series with the resistor describing the spontaneous emission. It has been recently found by Anthony et al [12] that self− pulsations are accompanied by negative resistance of the laser. Also, in an earlier work by D'Asaro et al [13], it was found that oscillations in the light output from the laser occur simultaneously with oscillations in the current.

It is interesting to note that phenomena that are optical in nature (self−pulsations, spontaneous emission) are responsible for elements in the "optical" branch in the equivalent circuit (i.e., in series with the inductance). Also the effect of the spontaneous emission, modeled as a positive resistance R_{se}, is to reduce the causes of self−pulsations, which are modeled by a negative resistance R_{sp}.

Figure 5.4−2 depicts the magnitude of a typical impedance function $|Z(\omega)|$ and the magnitude of the normalized light response function

$$\left| \frac{L(\omega)}{L(0)} \right| \triangleq \left| \frac{n_{ph}^1(\omega)I(0)}{n_{ph}^1(0)I(\omega)} \right|$$

where L denotes the light output from the laser. Both functions have a resonance peak at a frequency ω_{res} which is basically determined by the optical properties of the laser material and the laser itself:

$$\omega_{res} \approx \left[A \frac{N_{ph}^0}{\tau_{ph}} \right]^{\frac{1}{2}} \tag{5.4-10}$$

Far from ω_{res}, the impedance of the laser diode is very small in magnitude (i.e., almost perfect gain clamping), and the light response is flat and equal to its DC value. The magnitude of the resonance peak of the light transfer function (as compared to the low-frequency value) is

$$\left| \frac{L(\omega_{res})}{L(0)} \right| = \frac{\omega_{res}}{\dfrac{1}{\tau_{eff}} + AN_{ph}^0} \tag{5.4-11}$$
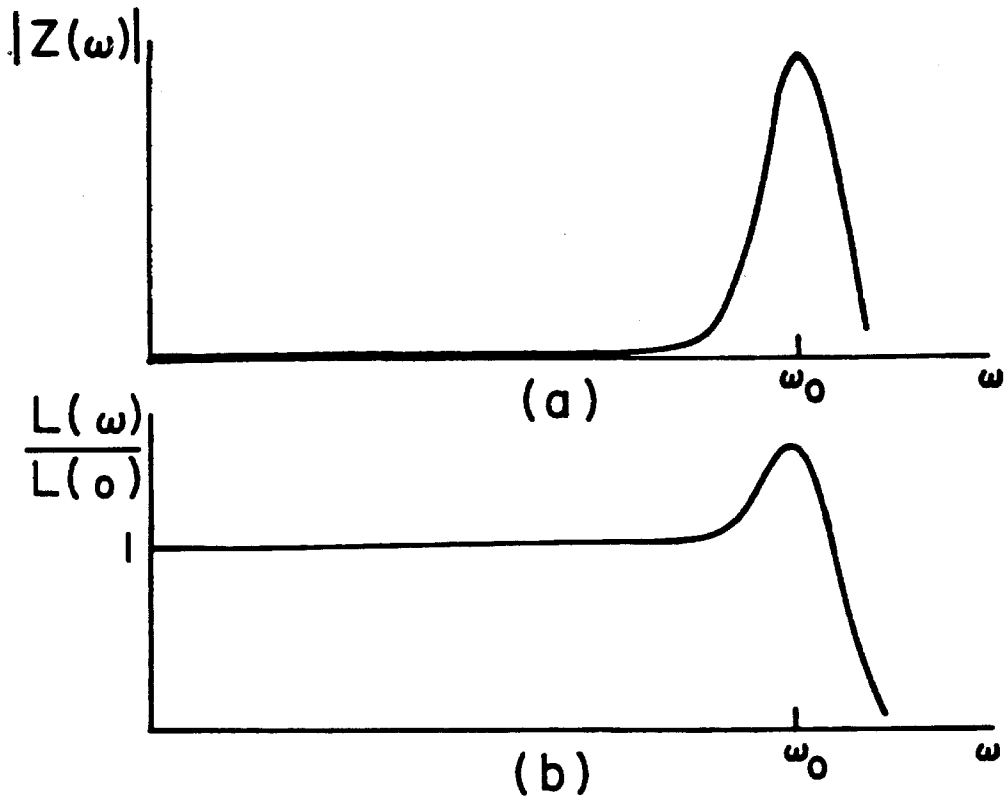
Figure 5.4- 2. a) Magnitude of the impedance function of a laser diode. b) Light versus current transfer function of a laser diode.

5.5 Numerical Calculations

Figure 5.5-1 shows some calculated results of the DC (or low-frequency) resistance (i.e., the real part of the impedance function at $\omega \to 0$) of the laser diode at the vicinity of the threshold, as a function of current, for several values of β and N_S.

These graphs indicate large values of negative resistance near the threshold for small values of β and N_S, and are in a good agreement with the experimental results reported recently by Anthoni et al [12]. In this case there is also a superlinear behavior in the light versus current curve of the laser in a narrow region near the threshold. For larger values of β and N_S, the absolute value of the DC resistance near threshold is small, and its sign depends on the particular values of the parameters. In general, lasers with large β ($\approx 1 \times 10^{-3}$), do not have negative resistance and thus are less likely to exhibit self-pulsations. Lasers with large values of N_S tend to have negative resistance with a small absolute value, and thus are less influenced by external electronic circuits. Since the values of the components in the model depend on the operating point, the resistance can be negative for some values of the bias current and positive for others. It should be noted that if the DC resistance of the laser diode is negative at a certain bias point, then the real part of its impedance will be negative at all frequencies at that bias point. Values taken for the calculations are $\delta = 0.02$, $A = 1.5 \times 10^{-6} cm^3 - sec^{-1}$, $N_{om} = 5 \times 10^{17} cm^{-3}$, $d = 0.3 \ \mu m$, $a = 300 \times 5 \mu m^2$, $\tau_{ph} = 1 \ ps$, and $\tau_S = 3 \ ns$.
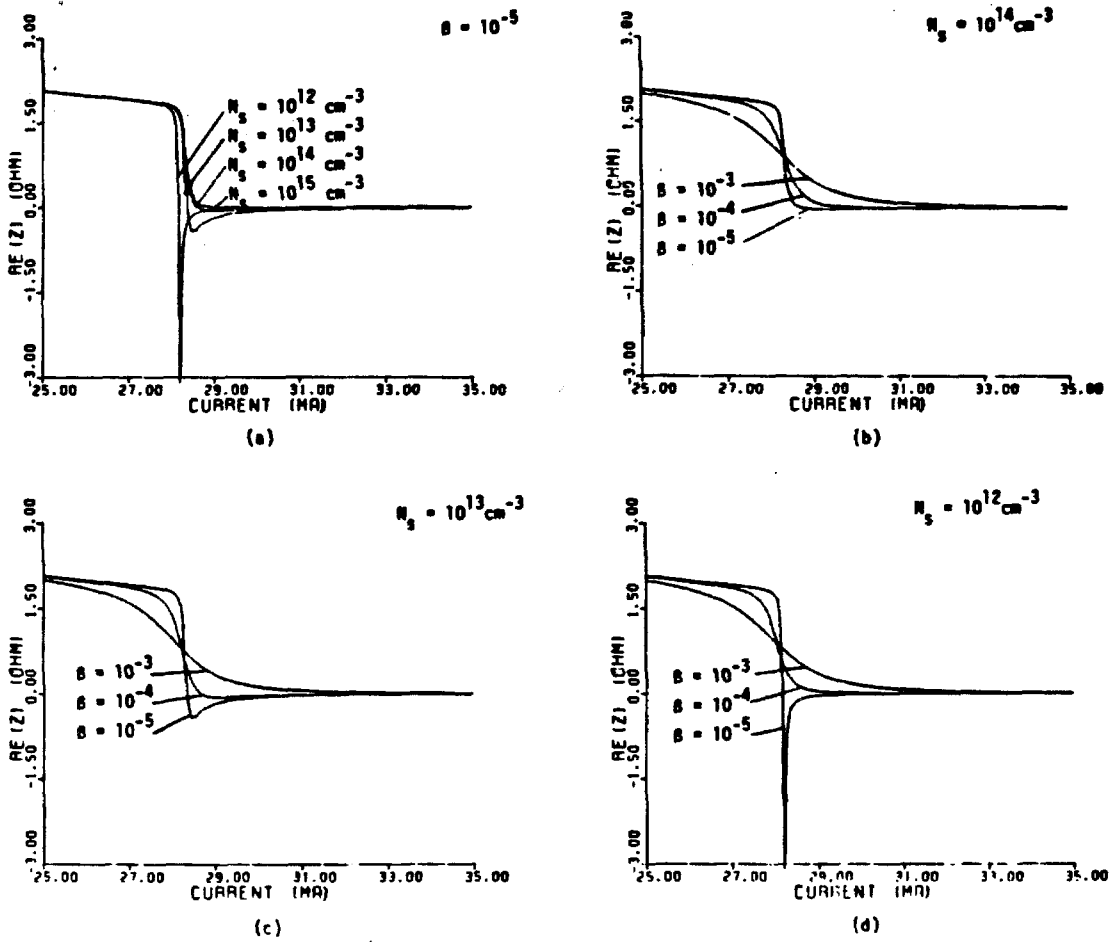
Figure 5.5-1. DC resistance of a laser diode. a)$\beta = 1 \times 10^{-5}$. b)$N_S = 1 \times 10^{14} cm^{-3}$. c)$N_S = 1 \times 10^{13} cm^{-3}$. d)$N_S = 1 \times 10^{12} cm^{-3}$.

It is very important to note that parasitic electronic components, which are not intrinsic to the laser operation but are nevertheless always present, tend to reduce the effects of electrical components connected in parallel with it. Among these components are the parasitic

capacitance of the diode, and mainly the parasitic series resistance. In order to exercise a significant control by connecting external components in parallel with the laser diode, the condition $\frac{2KT}{qI_{th}} >> R_c$ (R_c is the contact resistance of the diode) must be fulfilled. This condition is difficult to realize presently, but there is no reason why in future low threshold improved lasers this condition can not be met.

5.6 Modification of the Impedance Function via the Operation of the Laser as a Part of a Transistor

The resonance peak in the light versus current transfer function is undesirable, since it effects adversely the temporal response of the laser, for example by causing relaxation oscillations [5]. As can be seen from Equation (5.4−11), this resonance peak can be reduced by reducing the effective carriers lifetime, τ_{eff}. Several methods to achieve this goal have been proposed. The main idea behind all the schemes is to connect some kind of impedance in parallel with the laser. For frequencies far from resonance, this impedance has a little effect since the intrinsic impedance of the laser is small. Only near the resonance, when the laser impedance increases, the externally connected impedance may manifest itself by drawing current from the laser, thus reducing the resonance peak. It is clear that because of the low values of all the impedances involved, this external current drawing mechanism must be connected in parallel with the laser in an AC fashion. In some types of lasers this mechanism is built into their structure [14].

Various methods for reducing the resonance peak in the laser response have been suggested, and some of these have also been implemented [15]−[17]. In the following we analyze an alternative method of damping relaxation oscillations. The analysis will use charge control calculations which are sufficient to discuss the basic ideas. This method utilizes a proposed new type of device, where the laser itself operates as a part of a heterostructure transistor, with the active region as a part of the transistor emitter, as shown in Figure 5.6−1a. The basic device
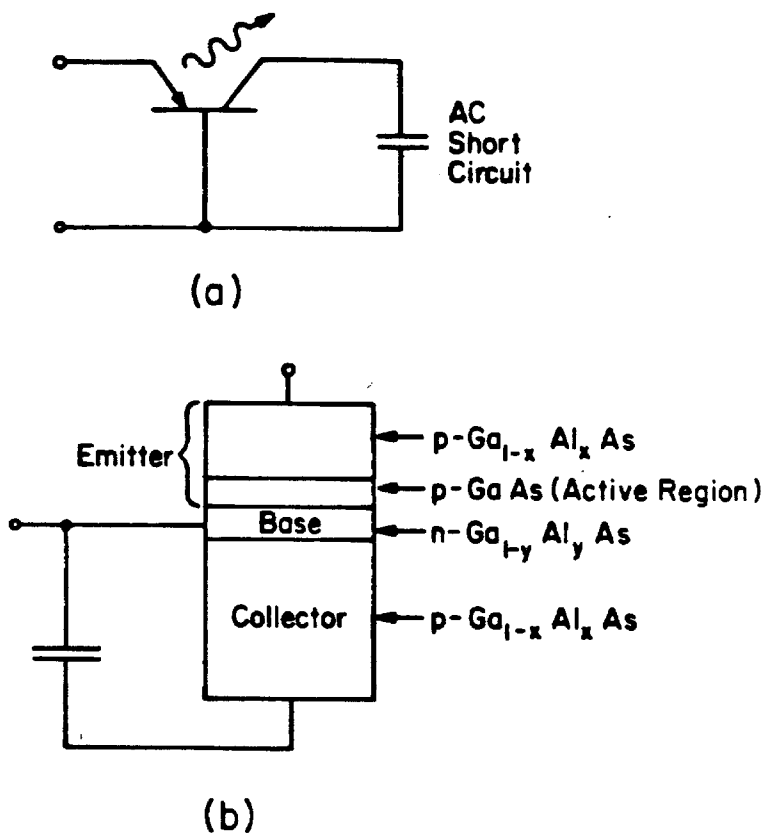
structure is shown in Figure 5.6−1b.

Figure 5.6- 1. a)Proposed device for reducing the laser resonance peak. b)Schematic structure of the device.

In this Translaser the function of the transistor is not to amplify input signals, but to control the carrier lifetime in the laser. The laser has two different carier lifetimes: one for DC and low frequencies, and one for frequncies near the resonance. At DC the collector terminal is floating, and thus both the emitter and the collector junctions are forward biased. The excess hole concentration in the active region (width

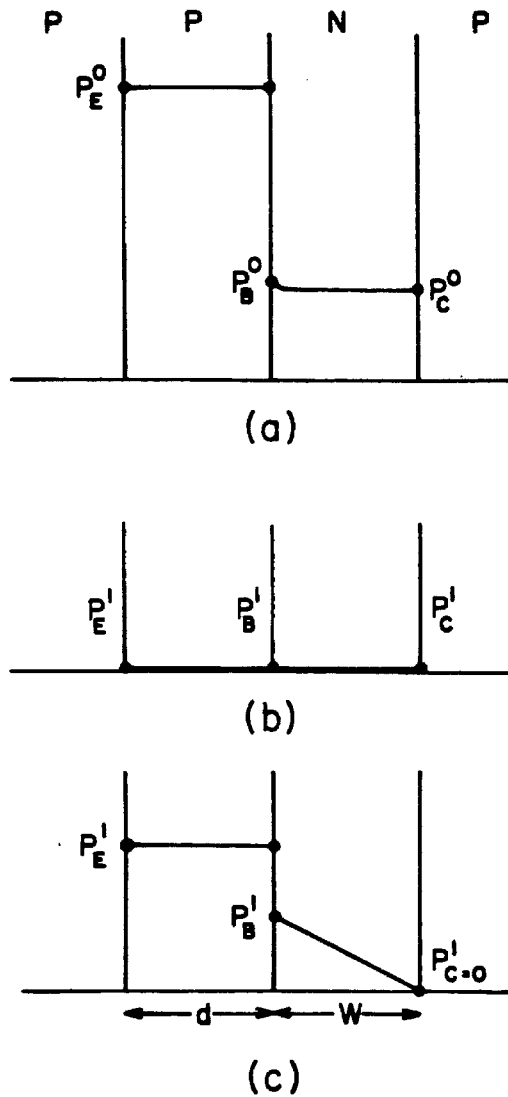*d*), and the base (width *W*) is shown in Figure 5.6−2a.

Figure 5.6- 2. Excess carrier concentration profile in the active region and in the base of the transistor. a)DC. b)low frequencies. c)frequencies near resonance.

As a first approximation, the active region excess carrier concentration

N_E^0 ($=P_E^0$ by quasineutrality) is constant, and the concentration across the base is also approximately constant (variations are of the order of only $\frac{KT}{q}$). We assume that $P_C^0 \approx P_E^0 = \delta P_B^0$, where δ is a factor determined by the Boltzmann statistics from the bandgap and doping differences between the active region and the base. ($\delta = e^{-\frac{\Delta E_g}{KT}} \frac{P_E^0}{P_B^0}$ for low level injection, and $\delta = e^{-\frac{\Delta E_g}{2KT}}$ for high level injection). As far as the laser operation is considered, the amount of current wasted in the DC operation is lost only by recombination in the base:

$$J_{leakage}^{DC} = q\frac{\delta P_E^0}{\tau_S}W \tag{5.6-1}$$

By analyzing the rate equation for the carriers we see that the effective DC lifetime is reduced by a factor of only $(1 + \delta\frac{W}{d})$, which is a small change if $\delta << 1$ and $W \lesssim d$. At low frequencies τ_{eff} is equal to τ_S since the carrier concentration at the active region is clamped and thus the AC component of the carriers concentration is virtually zero (Figure 5.6-2b). Only when we approach the resonance frequency, an appreciable AC component of the carrier concentration can be maintained in the active region. At the emitter-base junction $P_B^1 = \delta P_E^1$, but $P_C^1 = 0$ because of the imposed boundary conditions (Figure 5.6-2c). This causes a much larger leakage from the active region:

$$J_{leakage}^{RES} = \frac{qD_B \delta P_E^1}{W}$$

(5.6-2)

If we now take into account the finite resistances in the base (r_b) and collector (r_c) regions, we find that the carriers lifetime is reduced from τ_S to

$$\tau_{eff}^{RES} = \frac{\tau_S}{1 + \dfrac{\tau_S D_B \delta}{Wd} \dfrac{1}{1 + \dfrac{r_b + r_c}{r_0}}}$$

(5.6-3)

where

$$\frac{1}{r_0} \triangleq A_E \frac{q D_B \delta P_E^0}{W} \frac{q}{2KT}$$

(5.6-4)

where A_E is the area of the transistor emitter.

From Equations (5.6-3) and (5.6-4) we see that the necessary – and the difficult to achieve – prerequisite for a significant lifetime reduction is $r_b << (r_c + r_0) \lesssim R_d$. Realization of this requirement calls for the fabrication of layers with resistances of the order of at least $1 \times 10^{-6} \ \Omega \ cm^2$. For a typical set of values ($\delta = 0.1$, $P_E^0 = 2 \times 10^{18} cm^{-3}$, $\tau_S = 3nS$, $r_0 \times A_E \approx 5 \times 10^{-7} \Omega \ cm^2$, $W = 0.1 \mu m$ and $d = 0.2 \mu m$), the effective carriers lifetime is reduced to $0.07nS$ for $r_b + r_c = 0$, and to $0.55nS$ for $(r_b + r_c) \times A_E = 5 \times 10^{-6} \ \Omega \ cm^2$. We thus conclude that significant reduction of the carriers lifetime is achievable within the limits of the available technology.

References for Chapter 5

[1] J. Katz, S. Margalit, C. Harder, D. Wilt, and A. Yariv, "The Intrinsic Electrical Equivalent Circuit of a Laser Diode", IEEE J. Quant. Electron., **QE-17**, pp 4–7 (1981)

[2] I. Ury, S. Margalit, M Yust, and A. Yariv, "Monolithic Integration of an Injection Laser and a Metal Semiconductor Field Effect Transistor", Appl. Phys. Lett., **34**, pp 430–432 (1979)

[3] M. Yust, N. Bar–Chaim, S. H. Izadpanah, S. Margalit, I. Ury, D. Wilt, A. Yariv, "A Monolithically Integrated Optical Repeater", Appl. Phys. Lett., **35**, pp 795–797 (1979)

[4] J. Katz, N.Bar–Chaim, P. C. Chen, S. Margalit, I. Ury, D. Wilt, M. Yust, and A. Yariv "A Monolithic Integration of *GaAs/GaAlAs* Bipolar Transistor and Heterostructure Laser", Appl. Phys. Lett., **37**, pp 211–213 (1980)

[5] H. Kressel and J. K. Butler, *Semiconductor Lasers and Heterojunction Leds*, Academic Press, New York, 1977, Ch. 17

[6] Y. Suematsu and K. Furuya, "Theoretical Spontaneous Emission Factor of Injection Lasers", Trans. IECE Japan., **E60**, pp 467–472 (1977)

[7] K. Petermann, "Calculated Spontaneous Emission Factor for Double–Heterostructure Injection Lasers with Gain–Induced Waveguiding", IEEE J. Quant. Electron., **QE-15**, pp 566–570 (1979)

[8] W. B. Joyce and R. W. Dixon, "Analytic Approximations for the Fermi

Energy of an Ideal Fermi Gas", Appl. Phys. Lett., **31**, pp 354–356 (1977)

[9] M. Morishita, T. Ohmi, and J. Nishizawa, "Impedance Characteristics of Double–Heterostructure Laser Diodes", Solid State Electron., **22**, pp 951–962 (1979)

[10] K. Y. Lau, L. Figuroa, and A. Yariv, "Generation and Quenching of Intensity Self–Pulsations in Semiconductor Lasers Coupled to External Cavities", *Eleventh Intl. Quant. Electron. Conf.*, Boston, Mass., June 22–26, 1980 (Paper W.4)

[11] R.L. Hartman, R. A. Logan, L. A. Koszi, and W. T. Tsang, "Pulsations and Absorbing Defects in *(Al,Ga)As* Injection Lasers", J. Appl. Phys., **50**, pp 4616–4637 (1979)

[12] P. J. Anthony, T. L. Paoli, and R. L. Hartman, "Observations of Negative Resistance Associated with Superlinear F—ission Characteristics of *(Al,Ga)As* Double–Heterostructure Lasers", IEEE J. Quant. Electron., *QE–16*, pp 735–739 (1980)

[13] L. A. D'Asaro, J. M. Cherlow, and T. L. Paoli, "Continuous Microwave Oscillations in *GaAs* Lasers", IEEE J. Quant. Electron., **QE-4**, pp 164–167 (1969)

[14] N. Chinone, K. Aiki, M. Nakamura, and R. Ito, "Effects of Lateral Mode and Carrier Density Profile on Dynamic Behaviors of Semiconductor Lasers", IEEE J. Quant. Electron., **QE-14**, pp 625–631 (1978)

[15] R. Lang and K. Kobayashi, "Suppression of the Relaxation Oscilla-

tion in the Modulated Light Output of Semiconductor Lasers", IEEE J. Quant. Electron., **QE-12**, pp 194–199 (1976)

[16] Y. Suematsu and T. –H. Hong, "Suppression of Relaxation Oscillation in Light Output of Injection Lasers by Electrical Resonance Circuit", IEEE J. Quant. Electron., **QE-13**, pp 756–762 (1977)

[17] T. –H. Hong and Y. Suematsu, "Suppression of Resonance–Like Phenomena in the Light Output of Directly Modulated Injection Lasers by π–Type Suppressor Circuit", Trans. IECE Japan., **E61**, pp 121–124 (1978)